学位論文

Infrared spectroscopy of cool evolved stars with the ISO SWS

（ISO SWS による進化の進んだ低温度星の赤外スペクトルの研究）

平成10年12月博士（理学）申請

東京大学大学院理学系研究科
天文学専攻
青木和光

Infrared spectroscopy of cool evolved stars with the ISO SWS

Wako Aoki
School of Science, The University of Tokyo

December 1998

Contents

Chapter 1

Introduction

1.1 Evolution of intermediate- and low-mass stars

From the point of view on stellar evolution, stars are roughly classified into three categories according to their initial masses; massive ($M >$8-9$M_\odot$) stars, intermediate-mass (2-2.3$M_\odot$ $< M <$8-9$M_\odot$) stars and low-mass ($M <$2-2.3$M_\odot$) stars, where the criterion of the masses depends on the metallicity. While massive stars evolve to supergiants and eventually to type II supernovae, intermediate- and low-mass stars lose their envelopes by the stellar wind and evolve to white dwarfs. In this thesis, attention is concentrated on the late evolutionary stages of intermediate- and low-mass stars.

After the main sequence phase, stars begin hydrogen-shell burning and evolve to red giant branch stars. Low-mass stars are distinguished from intermediate-mass stars by the characteristics of the helium core and the helium ignition; low-mass stars develop the electron degenerate helium-core and violent helium-burning (helium flash) occurs when the core mass reaches about 0.45$M_\odot$ as a result of hydrogen-shell burning, while intermediate-mass stars begin the helium-core burning when the temperature and density reach suitable values during the core contraction. For this reason, the duration of red giant branch is much longer in low-mass stars than in intermediate-mass stars. However, it is not easy to distinguish observationally low-mass stars from intermediate-mass stars for individual objects, especially for field stars, because stars in both categories occupy similar temperature ranges. Therefore we do not distinguish the intermediate-mass stars from low-mass stars in this work.

After the helium-core burning phase, intermediate- and low-mass stars evolve to Asymptotic Giant Branch (AGB) stars which consist of the carbon-oxygen core, the thin helium-shell and the hydrogen-rich envelope (Iben & Renzini 1983). For the most part of this phase, the hydrogen shell burning is the main source of energy. However, as a result of the increase of the mass of the helium-shell below the hydrogen-burning shell, helium-burning intermittently occurs (so-called helium-shell flash or thermal pulse) and the carbon-oxygen core grows. During this phase, material processed in the helium-shell can be brought into the outer convective envelope and exposed to the surface (so-called third dredge-up).

On the other hand, the envelope mass gradually decreases due to the mass loss during the red giant phase[1]. The stellar mass loss significantly influences the evolution of red giants. In fact, the AGB phase terminates when the hydrogen-rich envelope is finally lost through the stellar mass loss. After the AGB phase, stars evolve to post-AGB stars, to planetary nebulae and eventually to white dwarfs.

Though there are many works on red giants from various points of view, we emphasize the two important changes in the red giant phase, especially in the AGB phase. The one is the change of the chemical composition in the stellar surface,

[1]The term 'red giant' is sometimes used to mean 'stars on the red giant branch'. However, in this thesis, we use this term to mean the stars in the post-main-sequence phase, i.e. red giant branch stars, clump stars and AGB stars.

and the other is the stellar mass loss which causes the growth of the circumstellar envelope.

During the main-sequence phase, the chemical composition in the stellar surface is believed to reflect the initial abundance of the star, except for some light elements (e.g. lithium). When stars evolve to red giants, the products of hydrogen-burning (CNO-cycle) during the previous phase are dredged up to the stellar surface (the first dredge-up), and abundances of carbon, nitrogen, oxygen and their isotopes considerably change (e.g. Lambert & Ries 1981). Since carbon abundance generally decreases by the CNO-cycle, a star keeps the carbon-to-oxygen abundance ratio (C/O ratio) to be smaller than unity, if the initial C/O ratio of the star is smaller than unity (e.g. C/O=0.48 in the solar photosphere).

In the AGB phase, the chemical composition in the stellar surfaces sometimes drastically changes due to the thermal pulse and the subsequent third dredge-up. Especially, it is important that the ^{12}C abundance in the surface of a star can increase through these processes. This is one of the explanations for the carbon star formation (e.g. Iben 1975, Lambert et al. 1986), though there are various types of carbon stars which cannot be explained by this scenario (e.g. Dominy 1984).

The effect of carbon excess on the atmosphere and the circumstellar envelope is significant in cool stars. Since the dissociation energy of CO is quite high, oxygen is almost completely locked up in CO in carbon-rich environment, while carbon is locked up in CO in oxygen-rich environment. For this reason, the molecule and dust formations in carbon-rich stars are quite different from those in oxygen-rich stars. This difference drastically affects not only the molecular and/or dust features observed, but also the structure of the atmosphere and the circumstellar envelope.

The high resolution spectroscopy with Fourier Transform Spectrometers (FTS's) have provided quite valuable results on abundances of red giants including AGB stars (e.g. Smith & Lambert 1990, Tsuji 1991, Aoki & Tsuji 1997, Lambert et al. 1986). However, the abundance analysis of AGB stars has been quite limited due to the difficulties in the analysis of the spectra with severe blending of molecular lines and in the modeling of the complicated atmospheres.

The changes of the chemical composition other than the carbon abundance in the AGB phase, e.g. the enhancement of lithium (e.g. Plez et al. 1993) and the *s*-process elements (e.g. Smith & Lambert 1985, Lambert et al. 1995), are also important to understand the evolution of AGB stars, but these are out of the scope of the present work.

Though the mass loss occurs even in stars on the main sequence, the rate is not high (e.g. about $10^{-14}M_\odot$yr^{-1} in the sun) enough to affect the following stellar evolution. However, the influences of mass loss in red giants are significant on their evolution. The mass loss rate of the red giant branch stars is not high (10^{-10}-$10^{-9}M_\odot$yr^{-1}), but the effect can be large because of the long duration of the red giant branch phase (10^8-10^9yr, depending on the stellar mass). Since the mass loss rate in the AGB phase is generally high (10^{-8}-$10^{-4}M_\odot$yr^{-1}), the mass loss

affects the structure of the hydrogen-rich envelope and of the atmosphere, and finally determines the termination of the AGB phase.

The mechanism of the stellar mass loss has not yet been clarified well. Although red giants have much larger radius (several tens or hundreds times solar radii) than stars on the main sequence, matters cannot easily escape from stars; for example, the escape velocity of a star with $100\,R_\odot$ and $1\,M_\odot$ is about $60\mathrm{kms}^{-1}$. Hence some mechanisms to produce the outflow are required. The acceleration of the outflow by the radiation pressure on dust grains and the momentum transfer to gases are considered in the modeling of the circumstellar envelopes (e.g. Goldreich & Scoville 1976). However, there remains a problem how matters escape from the photosphere to the dust forming region which should exist away from several or several tens stellar radii (e.g. Danchi et al. 1994). Several mechanisms such as pulsation driven winds (e.g. Bowen 1988), radiation pressure on spectral lines (e.g. Jørgensen & Johnson 1992), sound wave driven winds (e.g. Pijpers & Hearn 1989) have been proposed to explain this fact. In addition to the model for outflows with constant mass loss rate, the scenario called episodic mass loss has also been proposed. Detached shells were found by recent far-infrared and radio observations (Izumiura et al. 1996, Olofsson et al. 1998), and the relation between the intermittent mass loss and the thermal pulse was suggested.

Thus the changes of the chemical composition and the mass loss are the remarkable phenomena of the evolved intermediate- and low-mass stars. The understanding of these characteristics is also indispensable in the study of the evolution of our Galaxy, because the elements and dust grains produced in intermediate- and low-mass stars are released to interstellar medium through the stellar mass loss.

1.2 Atmosphere and circumstellar envelope of cool evolved stars

Many observational and theoretical researches have been done on the chemical composition and the structure of atmospheres and circumstellar envelopes of red giants. In this section, we briefly review these studies for three components; photosphere, cool circumstellar envelope and 'outer atmosphere' by which we mean the region between the photosphere and the circumstellar envelope.

1.2.1 Photosphere

The photosphere is the surface of a star whose radius is about 10^{13} cm (a few hundred solar radii) in the case of red giants. While the extension of the photosphere can usually be neglected in dwarfs, that is as large as the stellar radius in highly evolved stars for which the spherically extended model photospheres have been constructed (e.g. Watanabe & Kodaira 1978, Scholz & Tsuji 1984). The typical temperature of photospheres of red giants is 3000-4000K, but the temperature of the surface layer is as low as 1000-1500K in the photospheres of very cool stars.

The most spectral features in the optical and the near infrared wavelength regions are originating in photospheres. The molecular features such as TiO and C_2 in low resolution spectra are used to classify cool stars into spectral types. Since the spectral type is basically defined by the features originating in photospheres, these classification cannot necessarily be applied to very cool stars in which the radiation in the outer atmosphere may be dominant.

The photospheric structures of red giants have been investigated by many observations and theoretical studies, and model photospheres have been developed (e.g. Tsuji 1978, Jørgensen et al. 1992). However, some difficulties remain in understanding and modeling of photospheres of cool giants. The largest one is the complexity in the evaluation of molecular line opacities. Since molecules dominate in photospheres of cool giants, the influence of molecular line opacities on the temperature structure of the photosphere is significant, and a careful approximation of the opacities is required in the calculation of model photospheres (e.g. Tsuji 1994). Further, since molecular abundances are strongly dependent on the temperature structure of photospheres, the photospheric structure, molecular abundances and molecular opacities should consistently be solved in model calculations. For the same reason, the chemical composition, especially the C/O ratio, also influences the structure of photospheres through the molecule formation.

Studies based on high resolution spectra of red giants revealed a variety of chemical compositions in red giants, especially in AGB stars (Smith & Lambert 1990, Tsuji 1991, Lambert et al. 1986). However, there are large uncertainties in the abundance analyses of cool stars, not only due to the strong blending of molecular absorption lines, but also due to the uncertainties of model photospheres and stellar parameters.

The modeling of photospheres is usually done on the assumption of hydrostatic equilibrium. However, most evolved stars, especially Mira variables, show pulsations. The velocity variation in spectral lines originating in photospheres was actually observed for long period variables (e.g. Barnbaum 1992). For these stars, the effect of dynamics on the photospheric structure has been examined in model calculation (e.g. Bowen 1988, Höfner & Dorfi 1997).

1.2.2 Circumstellar envelope

The existence of a circumstellar envelope was found by Deutsch (1956) for a luminous M giant, α Her. We call here the region expanding with an almost constant velocity (10-20 kms^{-1}) a circumstellar envelope. The inner boundary of a circumstellar envelope is the dust forming region (about 10^{14}cm or several stellar radii away from the central star) where the outflow would be accelerated by radiation pressure on dust grains and by the friction between grains and gas materials. The outer limit of the envelope may be determined by the photo-dissociation of molecules by the interstellar ultraviolet radiation (10^{17}-10^{18}cm away from the star). The cool circumstellar envelopes are well traced by molecular emission (e.g. CO) in the radio range. By the CO observations, the mass loss rates and expansion velocities of envelopes have been derived (e.g. Olofsson et al. 1993). The cool circumstellar envelopes are also detected by the far infrared observations. Some recent radio and far infrared imaging observations revealed that several carbon stars have detached shells (Olofsson et al. 1996, Izumiura et al. 1996). Especially, the observation of CO emission by the interferometer showed that the detached shell of a carbon star, TT Cyg, is geometrically very thin (Olofsson et al. 1998). These results suggest the episodic mass loss which may relate to the thermal pulse in the AGB phase.

Because of the limited spatial resolution of CO emission observations, we can only obtain the information of the cool and extended envelope which is at least 10^{15}-10^{16}cm away from the central star. To investigate the inner envelope, the K I 769.9 nm and/or Na D lines scattering has been observed, and the mass loss rate and the expansion velocity were estimated (e.g. Mauron & Caux 1992, Gustafsson et al. 1997).

The modeling of circumstellar envelopes has been done including the acceleration of the outflow, heating and cooling processes and some chemical reactions (e.g. Goldreich & Scoville 1976). The photo-chemistry in cool envelopes was reviewed by Glassgold (1996).

1.2.3 Outer atmosphere

We define here the region between a photosphere and a circumstellar envelope as an outer atmosphere, though this region may also be called an inner envelope, a transition zone etc. Then the outer limit of this region would be the dust forming region where the mass loss outflow is accelerated. Danchi et al. (1994) investigated

the spatial distribution of warm dust around red giants and supergiants by the infrared spatial interferometry, and evaluated the size of the warm dust-shell to be 3-5 stellar radii or larger (They discuss the existence of two classes in the size). Therefore the outer atmosphere extends to about 10^{14}-10^{15}cm from the central star.

According to this definition, the chromosphere is included in this region. The chromospheres in cool giants were found and have been studied using the atomic lines such as Ca II H and K lines. Ultraviolet (UV) observations by *International Ultraviolet Explorer (IUE)* and *Hubble Space Telescope (HST)* also much contributed to the study of chromospheres in cool giants (e.g. Eriksson et al. 1986, Johnson et al. 1995). However, the origin of chromospheres of red giants is still unclear. Since the rotation of giants is generally quite slow, the heating due to magnetic field which may explain chromospheres and coronae in main-sequence stars is unlikely applicable to evolved stars. Several other heating mechanisms such as acoustic waves, acoustic shocks are proposed (e.g. Ulmschneider 1991), but no theory on the chromosphere has been established yet.

For clarifying the origin of the stellar mass loss, the first step should be to understand the physical structure and chemical processes in the outer atmospheres where the mass loss outflow originates. Extensive studies have been done for modeling of the chemical processes in this region including dust formation (e.g. Sedlmayr 1994) and chromospheric UV radiation (e.g. Beck et al. 1992) as well as the dynamics (e.g. Fleischer et al. 1992). However, the outer atmosphere is poorly understood due to its complexity. One observational difficulty is that this region cannot be spatially resolved, except for the infrared interferometric observation for several nearby objects. Then spectroscopic studies are quite important to investigate the structure as well as chemistry in outer atmospheres. Since this region would have the temperature about several hundred or a thousand Kelvin, infrared observations are desired. We briefly summarize the studies of cool giants based on infrared spectroscopy in the next section.

1.3 Infrared spectroscopy of cool evolved stars

Extensive efforts to obtain the infrared spectra have been made for red giants, because of their importance in the study of the late stages of stellar evolution. The low resolution spectra obtained by ground-based observations revealed several features such as the 3μm band in carbon stars (e.g. Noguchi et al. 1977), but the wavelength regions covered were quite limited. The Kuiper Airborne Observatory explored the wavelength regions which cannot be accessed from the ground (e.g. Goebel et al. 1980), but the wavelength regions studied so far, as well as the number of objects, have been more or less limited. The Low Resolution Spectra (LRS) of the InfraRed Astronomical Satellite (IRAS) covered the wavelength region from 8 to 23 μm and contributed so much to the study of the cool giants with a thick circumstellar envelope. The low resolution spectra of late-type stars from 1.4 to 12 μm were also obtained with the spectrometers on board the Infrared Telescope in Space (IRTS, Murakami et al. 1996).

The high resolution spectra obtained by FTS's have provided important information on the chemical composition of red giants (e.g. Smith & Lambert 1990) and on the structure of the circumstellar envelope as well as of the photosphere (e.g. Keady et al. 1988). The outer atmosphere was also investigated based on the FTS spectra by Tsuji (1988) who revealed the existence of warm and quasi-static layers close to the stars.

Though important results have been obtained by the infrared spectroscopy so far, the wavelength region and/or spectral resolution are limited. Then a variety of atomic, molecular and solid-state spectral features in the infrared region, which are expected to originate in the outer atmospheres as well as in the photospheres of red giants, remain to be investigated. The entire spectra from 2.5 to 45 μm have become available by the Short Wavelength Spectrometer (SWS, de Graauw et al. 1996) on board the Infrared Space Observatory[2] (ISO, Kessler et al. 1996) launched in November 1995. The resolving power of the SWS normal grating mode is from 1000 to 2000 which is high enough to detect molecular band features (e.g. the band heads of the CO fundamental bands), atomic line emission and dust features.

Several new results on the photospheres and the outer atmospheres of red giants have already been obtained using the ISO SWS. The existence of H_2O in the outer atmospheres of red giants was revealed by Neufeld et al. (1996) and Tsuji et al. (1997a), in addition to H_2O in the cool and extended stellar outflow. CO_2 in the outer atmospheres was also found as emission features (Justtanont et al. 1998, Ryde et al. 1999) and as absorption features (Tsuji et al. 1997a). The unexpected SO_2 features were detected in several oxygen-rich AGB stars (Yamamura et al. 1999). The time variation of dust features in oxygen-rich Mira variables was reported by Onaka et al. (1998).

[2]Based on observations with ISO, an ESA project with instruments funded by ESA Member States (especially the PI countries: France, Germany, the Netherlands and the United Kingdom) with the participation of ISAS and NASA.

1.4 Goal of the research and outline of this thesis

In the situation discussed above, we planed the observations of cool evolved stars with the ISO SWS to investigate the region from the photosphere to the outer atmosphere. Rich vibration-rotation spectra of molecules in the infrared region are expected to be quite useful in the understanding of the photospheres and the outer atmospheres of cool evolved stars. Atomic forbidden lines would also be useful to investigate the outer atmospheres. Dust features are also expected in these stars, but we gave a priority to atomic and molecular features in the selection of objects and wavelength regions in our observing program with the ISO SWS.

We selected stars without heavy infrared excess as our sample. Since the photospheric contribution is dominant in the infrared region for the stars without heavy infrared excess, we examine our model photospheres for these stars by the use of infrared spectra at first, and discuss the contribution of the absorption or emission in the outer atmosphere in the second step. To investigate the effect of the basic stellar properties such as the temperature and the chemical composition on infrared spectra, we selected objects based on spectral types. Our sample consists of K and M giants, oxygen-rich and carbon-rich Mira variables, carbon stars including N-type, SC-type, J-type and CH stars (The classification of carbon stars will be reviewed in Chapter 5).

The results of the analysis of some molecular features in oxygen-rich giants have already been reported by Tsuji et al. (1997a, b). In Tsuji et al. (1997a), the H_2O absorption was detected even in an early M giant, β Peg, in which the existence of H_2O is not predicted by the model photosphere. The excess absorption of H_2O and CO_2, which cannot be explained by the predicted spectra based on the model photospheres, was also found in late M giants and a Mira variable. We concluded that these excess absorption is not photospheric origin, but originates in warm molecule forming envelopes of these stars. Such warm and dense molecular envelopes will be a site of various chemical reactions, dust formation and acceleration of mass loss outflows.

In this thesis, we report the molecular features detected in carbon stars, and discuss the molecules in the photospheres and the outer atmospheres of carbon stars. As in the optical wavelength region, molecular spectra in the infrared region of carbon stars should be quite different from those of oxygen-rich giants, except for CO bands; in carbon stars, carbon-bearing molecules such as CS, CH, HCN, C_2H_2 are expected to be detected. Unfortunately, spectral line lists of these molecules are less established than those of molecules observed in oxygen-rich stars (e.g. H_2O, CO_2). Therefore, we need to survey the basic molecular data and to produce molecular line lists. Model photospheres of carbon stars are also required to analyze the infrared spectra and to discuss not only the molecular features originating in the photospheres but also possible absorption and/or emission in the outer atmospheres.

Further, we report the detection of fine-structure line emission of metals, which may be a direct evidence of the outer atmosphere, in both oxygen-rich and carbon-rich giants, and discuss the relation of the outer atmospheres with the chemical composition and with the evolutionary phase.

We describe our observations with the ISO SWS in Chapter 2. The method of data reduction is also briefly summarized in the chapter. In Chapter 3, basic molecular data are compiled and molecular line lists are produced. For the analysis of infrared spectra of carbon stars, model photospheres are used. For the model calculation, the revised version of the computational code developed by Tsuji (e.g. 1999) was used. We discuss the approximation of molecular line opacities in the model calculation in Chapter 4, where the dependence of the model photosphere on the effective temperature and on the carbon abundance is also discussed.

After the above preparation, we analyze and discuss the molecular spectra of N-type and SC-type carbon stars in Chapter 5. In the wavelength region between 2.5 and 15 μm, we identified many band features of molecules such as HCN, CS, SiS, most of which were clearly detected for the first time in carbon stars. We discuss the dependence of these molecular features on the C/O ratio. The molecular emission in the outer atmospheres is also discussed. The main result of this chapter has already been published (Aoki et al. 1998b).

In Chapter 6, we report the detection of fine-structure line emission of iron, silicon and sulfur in oxygen-rich AGB stars as well as in carbon stars. The mass and temperature of the line emitting region are derived from the line fluxes measured and excitation levels of detected lines. Based on these results, the location of the line emitting region, the chromospheric activity, chemistry in the outer atmosphere and the relation to the stellar evolution are discussed. The preliminary result described in this chapter has already been published (Aoki et al. 1998a).

References

Aoki W., Tsuji T., A&A 328, 175

Aoki W., Tsuji T., Ohnaka K., 1998a, A&A 333, L19

Aoki W., Tsuji T., Ohnaka K., 1998b, A&A 340, 222

Barnbaum C., 1992, AJ 104, 1585

Beck H. K. B., Gail H. -P., Henkel R., Sedlmayr E., 1992, A&A 265, 626

Bowen G. H., 1988, ApJ 329, 299

Danchi W. C., Bester M., Degiacomi C. G., Greenhill L. J., Townes C. H., 1994, AJ 107, 1469

de Graauw Th., Haser L. N., Beintema D. A. et al., 1996, A&A 315, L49

Deutsch A. J., 1956, ApJ 123, 210

Dominy J. F., 1984, ApJS, 55, 27

Eriksson K., Gustafsson B., Johnson H.R. et al., 1986, A&A 161, 305

Fleischer A. J., Gauger A., Sedlmayr E., 1992, A&A 266, 321

Glassgold A. E., ARAA 34, 241

Goebel J. H., Bregman J. D., Goorvitch D. et al., 1980, ApJ 235, 104

Goldreich P., Scoville N., 1976, ApJ 205, 144

Gustafsson B., Eriksson K., Kiselman D., Olander N., Olofsson H., 1997, A&A 318, 535

Höfner S., Dorfi E. A., 1997, A&A 319, 648

Iben I. Jr., 1975, ApJ 196, 525

Iben I. Jr., Renzini A., 1983, ARAA 21, 271

Izumiura H., Hashimoto O., Kawara K., Yamamura I., Waters L. B. F. M., 1996,A&A 315, L221

Jørgensen, U. G., Johnson H. R., 1992, A&A 265, 168

Jørgensen, U. G., Johnson H. R., Nordlund A., 1992, A&A 261, 263

Johnson H. R., Ensman L. M., Alexander D. R., 1995, ApJ 443, 281

Justtanont K., Feuchtgruber H., de Jong T. et al, 1998, A&A 330, L17

Keady J. J., Hall D. N. B., Ridgway S. T., 1988, ApJ 326, 832

Kessler M. F. Steinz J. A., Anderegg M. E. et al., 1996, A&A 315, L27

Lambert D. L., Gustafsson B., Eriksson., Hinkle K.H., 1986, ApJS, 62,373

Lambert D. L., Ries L. M., 1981, ApJ 248, 228

Lambert D. L., Smith V. V., Busso M., Gallino R., Straniero O., 1995, ApJ 450, 302

Mauron N., Caux E., 1992, A&A 265, 711

Murakami H., Freund, M. M., Ganga K. et al., 1996, PASJ 48, L41

Neufeld D. A., Chen W., Melnick G. J. et al., 1996, A&A 315, L237

Noguchi K., Maihara T., Okuda H., Sato S., Mukai T., 1977, PASJ 29, 511

Olofsson H., Eriksson K., Gustafsson B., Carlström U., 1993, ApJS 87, 267

Olofsson H., Bergman P., Eriksson K., Gustafsson B., 1996, A&A 311, 587

Olofsson H., Bergman P., Lucas R., et al. , 1998, A&A 330, L1
Onaka T., Yamamura I., de Jong T., et al. 1998, Ap&SS 255, 331
Plez B., Smith V. V., Lambert D. L., 1993, ApJ 418, 812
Pijpers F. P., Hearn A. G., 1989, A&A 209, 198
Ryde N., Eriksson K., Gustafsson B., 1999, A&A 341, 579
Scholz M., Tsuji T., 1984, A&A 130, 11
Sedlmayr E., 1994, LNP 428, *Molecules in the Stellar Environment*, ed. U. G. Jørgensen, 163
Smith V.V., Lambert D.L., 1985, ApJ 294, 326
Smith V.V., Lambert D.L., 1990, ApJS 72, 387
Tsuji T., 1978, A&A 62, 29
Tsuji T., 1988, A&A 197, 185
Tsuji T., 1991, A&A 245,203
Tsuji T., 1994, LNP 428, *Molecules in the Stellar Environment*, ed. U. G. Jørgensen, 79
Tsuji T., 1999, in proceedings of IAU Symp. 177, *The carbon star phenomenon*, ed. R. F. Wing, in press
Tsuji T., Ohnaka K., Aoki W., Yamamura I., 1997a, A&A 320, L1
Tsuji T., Ohnaka K., Aoki W., 1997b, ASP Conf. ser. 124 *Diffuse Infrared Radiation and the IRTS*, eds. H. Okuda, T Matsumoto and T. Roellig, 91
Ulmschneider P., 1991, *Mechanisms of Chromospheric and Coronal Heating*, eds. P. Ulmschneider, E. R. Priest, R. Rosner, 328
Watanabe T., Kodaira K., 1978, PASJ 30, 21
Yamamura I., de Jong T., Onaka T., Cami J., Waters L.B.F.M., 1999, A&A 341, L9

Chapter 2

Observation with the ISO SWS

2.1 Introduction

As discussed in Chapter 1, infrared observations are indispensable for the study of cool objects which radiate their most energy in the infrared range. However, the most of this wavelength region remains to be investigated due to the absorption in Earth's atmosphere and to thermal emission from the telescope and instruments. For this reason, cooled space telescopes have been desired. The first infrared satellite, IRAS, was launched in 1983, which surveyed almost all sky and obtained low resolution spectra (LRS) for bright objects. Contrary to IRAS, ISO was destined to do detailed studies of selected objects and regions, and realized the observation for wider wavelength range, with better spatial and/or spectral resolution and with greater sensitivity. ISO was launched on November 17, 1995, and completed the mission on May 16, 1998.

The spectroscopy for the whole infrared region became available by the Short Wavelength Spectrometer (SWS) covering 2-45 μm and the Long Wavelength Spectrometer (LWS) (45-200 μm) on board ISO. For the study of the atomic and molecular features in cool evolved stars, we planed the observation with the SWS. The instrument, observing mode and data reduction technique of the SWS were reviewed by de Grauuw et al. (1996).

The SWS covers the wavelength range from 2.38 to 45 μm by two gratings (SW and LW) and by four detector arrays. The spectral resolution of normal grating mode is from 1000 to 2000 depending on the wavelength. The observing modes we used are the normal grating mode (SWS06) and the rapid scan mode (SWS01, speed 1) with a resolution of 1/8 of the full spectral resolving power (i.e. about 200). The exception is the observation of α Cet for which we used the SWS01 (speed 4) with the full resolving power.

The spectrum consists of 12 different spectral bands called 'AOT bands' which are determined by the combination of the grating, the grating order and the detector array. As a result, discontinuities in an observed spectrum are sometimes present which can in principle be eliminated if a correction for spectral responsivity of the instrument is applied. This point will be discussed in Section 2.3.

Each detector is an one-dimensional array with 12 detector elements. The quality of the obtained data can be estimated by the dispersion of signals among these detector elements.

In Section 2.2, the sample of our program and observing modes are described. The method of the data reduction, calibration, and the quality of the data are discussed in Section 2.3.

2.2 Observations

In the guaranteed time observing program (REDSTAR1) and the open time program (PROP_001) using the SWS, we observed cool evolved stars with various spectral types. As described in Section 1.4, we intended to study the region from the photosphere to the outer atmosphere of cool giants using atomic lines and molecular features. To investigate the effect of basic stellar properties such as the temperature and chemical composition on infrared spectra, we selected objects with various spectral types. Our sample covers K-M giants, oxygen-rich and carbon-rich Mira variables, and carbon stars including N-type, SC-type, J-type and CH stars.

We give the objects analyzed in this work among them in Table 2.1. They are bright and typical stars for each spectral type. The spectra of N-type and SC-type carbon stars are analyzed in Chapter 5 to investigate the molecular features which may originate in the photospheres and in the outer atmospheres. For the five M giants and the five carbon stars observed by the higher resolution modes (i.e. SWS06 or SWS01-4), the fine-structure emission lines of metals near 25 μm and 35 μm are studied in Chapter 6. The spectral resolution and the aperture size are given in Table 2.2 for each spectral region.

Table 2.1: Summary of observations

star	spectral type[1]	AOT	wavelength range	TDT[2]	obs. date
α Cet	M1.5III	SWS01-4	2.38-45 μm	6750	29 Jan 1998
ρ Per	M4II	SWS06	2.45-5.5,14.5-16.5, 22-27 μm	3221	5 Mar 1998
α Her	M5Ib-II	SWS06	2.45-5.5,14.5-16.5, 22-27 μm	3221	6 Feb 1998
30g Her	M6III	SWS06	2.45-45 μm	8100	23 Aug 1996
SW Vir	M7-8III	SWS06	2.45-45 μm	8100	20 Jul 1996
TX Psc	N-type (C7,2)	SWS06	2.45-45 μm	8100	26 Nov 1996
V460 Cyg	N-type (C6,3)	SWS01-1	2.38-45 μm	1352	11 Jan 1997
TT Cyg	N-type (C5,4)	SWS01-1	2.38-45 μm	1352	30 May 1997
		SWS06	13-15 μm	1080	30 May 1997
W Ori	N-type (C5,4)	SWS06	23.5-26.5 μm	758	22 Mar 1998
WZ Cas	SC-type (C9,2JLi)	SWS06	2.45-45 μm	8964	22 Jul 1996
W Cas	SC-type (C7,1e)	SWS01-1	2.38-45 μm	1352	12 Jan 1997
RZ Peg	SC-type (C9,1e)	SWS01-1	2.38-45 μm	1352	10 Jun 1996
		SWS06	13-15 μm	1080	10 Jun 1996
T Lyr	J-type (C6,5J)	SWS06	2.45-45 μm	8964	12 Nov 1996
V CrB	Mira, CH? (C6,2e)	SWS06	2.45-45 μm	8964	29 Jul 1996

[1] From Keenan & Boeshaar (1980) and Yamashita (1972) for carbon stars
[2] Target dedicated time (sec)

Table 2.2: Resolution and aperture size

wavelength region (μm)	resolution	aperture area (")
2.38-8	1000-2000	14 × 20
13-15	1400-1600	14 × 27
24-26	1000-1200	14 × 27
34-36	1000-1200	20 × 33

2.3 Data reduction

The data reduction methods were reviewed by de Graauw et al. (1996). The flux calibration, the Relative Spectral Response Function (RSRF) and the beam profile were given by Schaeidt et al. (1996). The wavelength calibration, the spectral resolution and the instrumental profile were described by Valentijn et al. (1996).

The data obtained with ISO are distributed as three formats which are processed by the standard product generation pipeline; Edited Raw Data (ERD), Standard Processed Data (SPD) and Auto-Analysis Results (AAR). In the case of the SWS, the raw data consist of 24 digital readouts per second. By removing the instrumental effect shorter than 1 second, the data are converted to SPD in which the slopes (μV/sec) against time and wavelengths (μm) assigned are given. In the processes from SPD to AAR, the instrumental effects longer than 1 second are removed. Namely, the dark currents are subtracted, the spectral responsivities of individual AOT bands are corrected, the detector responses are converted from μV/sec to Jy and data formats are converted to flux density against wavelength. By these processes, the relation between wavelength (μm) and flux density (Jy) is derived for each detector element.

The flux calibration is done by evaluating the sensitivity of 12 AOT bands using the standard stars, and by determining the RSRF for each AOT band. The flux level of each AOT band is calibrated for so-called 'key wavelength' where RSRF of the AOT band is at its maximum and the spectra of standard stars are expected to be relatively featureless. For each AOT band, the RSRF was measured to black-body sources prior to the launch of ISO. For some AOT bands, the RSRF's were modified based on the re-measurement to standard stars.

We carried out the most data reduction from ERD or SPD using the SWS Interactive Analysis software (SWS IA). One reason is that the qualities of AAR's were not guaranteed in the early stage of the data distribution, and another is that the further optional processes can be introduced in the reduction from SPD to AAR. We did the data reduction from ERD for the wavelength region at around 25 μm of some bright objects. This is because a small error in the wavelength calibration was reported and that could cause rather large error in flux calibration by the RSRF in this wavelength region. This problem can be avoided by the reduction from ERD by using the new calibration data provided.

The spectra of the AOT bands of 12-16 μm region are severely affected by fringes due to the regular interference patterns, which depend on the exact pointing of the satellite at the time of the observation. To reduce this effect, we applied the defringing algorithm in the SWS IA package 'resp_inter' which tries to cancel the fringes by the small shift of the RSRF for wavelength. Such a procedure is, however, somewhat questionable because the real features occurring at frequencies close to the fringe pattern may be taken away and we need special care in the discussion on the spectra processed by the defringing procedure.

The post AAR analysis is also available with the SWS IA. We combined the spectra obtained by different 12 detectors and by 2 scans called up-scan and down-scan (This process is called 'flat-fielding'). After discarding the data points affected by transients, we re-sampled data points and obtained the spectra with the instrumental resolution.

One spectrum from 2.38 to 45 μm consists of 12 AOT bands (see Section 2.1). There are some discrepancies in fluxes between different AOT bands due to the uncertainty in flux calibration. These were corrected by scaling with respect to the band 1B (2.6-3.0 μm) in the present work. The slopes of the spectrum in the individual AOT bands were not changed after the reduction by the SWS IA. The flux discrepancies are at most 10%. This correction is not important for the present work on the individual atomic and molecular features, though a more careful flux calibration is necessary for the study on the spectral energy distribution.

We can estimate the quality of the data using the standard deviations of signals in one resolution element, but should be careful with fringes and some spurious features. To distinguish the real features like the forbidden line emission from spurious features, we need to confirm the detection in two scans and also in 12 different detector elements. The main uncertainties in the observed spectra between 12 and 16 μm come from the instrumental fringing.

The spectra obtained by these processes are shown in Figures 5.1, 5.2 and 6.1. We show these spectra as F_ν(Jy) against λ (μm) as the usual manner of the presentation for the ISO SWS data.

References

de Graauw Th., Haser L. N., Beintema D. A. et al., 1996, A&A 315, L49
Keenan P. C., Boeshaar P. C., 1980, ApJS 43, 379
Schaeidt S. G., Morris P. W., Salama A. et al., 1996, A&A 315, L55
Valentijn E. A., Feuchtgruber H., Kester D. J. M. et al., 1996, A&A 315, L60
Yamashita Y., 1972, Ann. Tokyo Astr. Obs. 2nd Ser. 13, 169

Chapter 3

Molecular data

3.1 Introduction

In the infrared region, there are rich vibration-rotation transitions of molecules. Some electronic transitions also exist in the near infrared region (e.g. the CN red system). The absorption by diatomic molecules is important in the photosphere of the stars cooler than about 4000K. In addition, polyatomic molecules become abundant in the photospheres of cooler stars, and their absorption features dominate in the infrared region.

For the analysis of molecular features in the infrared spectra of carbon stars, we produced the line lists of various molecules. In the following sections, the basic data used to produce the line lists for the vibration-rotation transitions of diatomic molecules (CO, CS, SiS and CH), electronic transitions of diatomic molecules (the C_2 Ballik-Ramsay system and the CN red system) and the vibration-rotation transitions of polyatomic molecules (HCN and C_2H_2) are described in this order. The molecular bands expected in the spectra of carbon stars are summarized in Figure 3.1.

For calculating the synthetic spectra, we need the line position, which is usually represented by wavenumber (cm^{-1}) or wavelength (μm) in the infrared region, the lower excitation potential (χ cm^{-1}) and the line strength (gf-value) for each line.

By the use of the gf-value and the lower excitation potential, the line intensity which depends on temperature (T) is represented by

$$S(J,v,T) = \frac{\pi e^2}{m_e c^2} n(T) \frac{gf \cdot e^{-\frac{hc\chi}{kT}}}{Q(T)}, \qquad (3.1)$$

where $n(T)$ is the number of the molecule, $Q(T)$ is the partition function and the others have their usual meanings. The wavenumber and the lower excitation potential are derived from the energy levels of molecules and the selection rules of the transition. The line strengths are decomposed to band (rotationless) oscillator strengths and rotational strengths, but usually corrected for the interaction between rotation and vibration. An extensive description of molecular structures and molecular spectra can be found in Herzberg (1950 and 1945) for diatomic and polyatomic molecules, respectively.

To produce the line lists of molecules, we surveyed the experimental data and the corresponding formula in literatures. We extrapolated the calculation for higher rotational energy levels (i.e. higher J) when the laboratory data are not enough to apply to the calculation of the stellar spectra. We will show the synthetic spectra of the above molecules in Figures 5.3-5.9 (Chapter 5).

It should be noted that the higher order terms in the formula of the energy levels are sometimes neglected, and the uncertainty of the wavenumber in our line lists is about 0.1 cm^{-1}. This uncertainty is small enough to analyze our SWS spectra, but more accurate calculation may be necessary for analyzing higher resolution spectra.

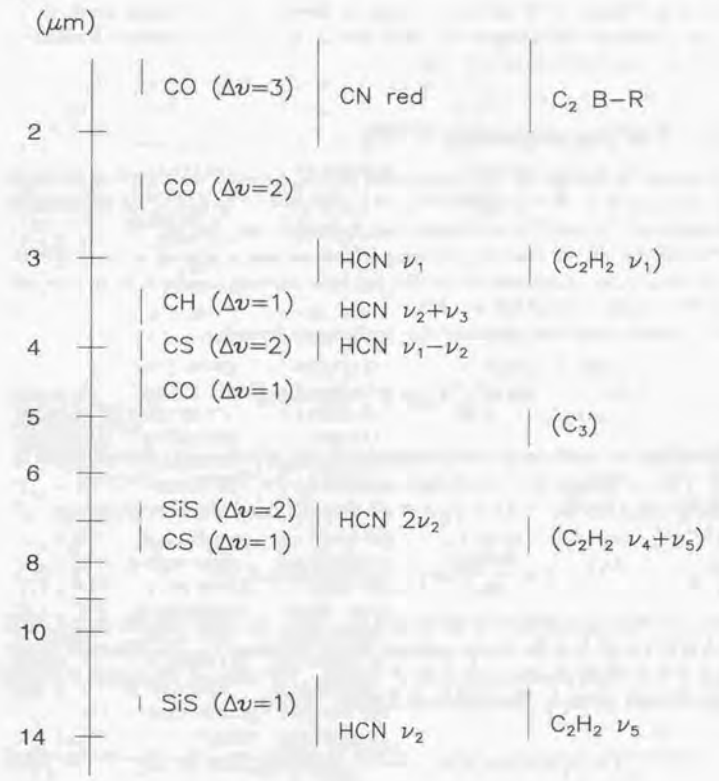

Figure 3.1: The molecular bands expected in the spectra of carbon stars

3.2 Vibration-rotation transition of diatomic molecules

In the spectra of carbon stars, the vibration-rotation bands of CO, CS and CH are expected, and their band heads were clearly detected in our SWS spectra as discussed in Chapter 5. In addition to these molecules, the absorption bands of SiS were also detected (see Chapter 5). We describe the vibration-rotation transitions of these four molecules in this section.

3.2.1 Carbon monoxide (CO)

We prepared the line list of the fundamental bands (4.3 μm$\sim$) and the first overtone bands (2.3 μm$\sim$) of $^{12}C^{16}O$ and $^{13}C^{16}O$. We neglected $C^{17}O$ and $C^{18}O$ because the abundances of ^{17}O and ^{18}O are usually much smaller than that of ^{16}O.

The line list of CO vibration-rotation transition was produced in Tsuji (1986). But we review the calculation of the line list here, because similar calculations will be applied to the cases of CS and SiS.

The energy levels are calculated by the Dunham formula;

$$E = \sum_{i,j} Y_{i,j}(v+\frac{1}{2})^i[J(J+1)]^j. \tag{3.2}$$

The Dunham coefficients were determined by the experiments (Guelachvili et al. 1983). The coefficients are summarized in Table 3.1 for $^{12}C^{16}O$ and $^{13}C^{16}O$.

The f-value for the $(v, J) \rightarrow (v+n, J')$ transition of CO can be given by

$$f = \frac{8\pi^2 mc}{3he^2}\omega S_J < v, J|M|v+n, J' >^2, \tag{3.3}$$

where ω is the wavenumber of the transition, S_J is the Hönl-London factor, and $< v, J|M|v+n, J' >$ is the dipole moment matrix element. The Hönl-London factor (S_J) is $J+1$ for R branch and J for P branch. We adopted the dipole moment matrix element given by Chackerian & Tipping (1983);

$$< v, J|M|v+n, J' >^2 = \frac{M(n)^2(v+n)!}{v!n!} H_n(v)F_n(v,m), \tag{3.4}$$

where $M(n)$ is the rotationless matrix element, $H_n(v)$ represents the effect of the vibrational anharmonicity, and $F_n(v,m)$ is the Herman-Wallis factor which describes the influence of the vibration-rotation interaction ($m = J+1$ for R branch $m = -J$ for P branch). Tsuji (1986) adopted the least square fitting coefficients to $H_n(v)$ and $F_n(v,m)$ given by Chackerian & Tipping (1983) and those provided by Drs. Tipping and Chackerian for higher excitation lines.

Table 3.1: Dunhum coefficients for CO, CS and SiS

Constant	$^{12}C^{16}O$	$^{13}C^{16}O$	$^{12}C^{32}S$	$^{13}C^{32}S$	$^{28}Si^{32}S$
$Y_{1,0}$	2169.813079	2121.439427	1285.15525	1248.58230	749.645653
$Y_{2,0}$	−13.28790597	−12.70207525	−6.502789	−6.13727	−2.586222
$Y_{3,0} \times 10^2$	1.041444730	0.973387618	0.3923	0.34554	0.10408
$Y_{4,0} \times 10^5$	6.921598529	6.324758585	−1.05		−0.73
$Y_{5,0} \times 10^7$	1.657890319	1.481162575			
$Y_{6,0} \times 10^9$	2.466226718	2.154216361			
$Y_{7,0} \times 10^{10}$	−8.630071431	−7.370214014			
$Y_{8,0} \times 10^{11}$	1.261536024	1.138528123			
$Y_{9,0} \times 10^{14}$	−8.363842545	−6.827949978			
$Y_{0,1}$	1.931280862	1.846151538	0.82004244	0.77403917	0.303527884
$Y_{1,1} \times 10^2$	−1.750410155	−1.635943496	−0.591743	−0.542951	−0.1473159
$Y_{2,1} \times 10^7$	5.422101371	5.150977893	−12.42	−3.83	−0.311
$Y_{3,1} \times 10^8$	1.311844382	1.172004433			−0.908
$Y_{4,1} \times 10^9$	1.401093705	1.223836787			
$Y_{5,1} \times 10^{12}$	−5.329907475	−4.978830838			
$Y_{6,1} \times 10^{12}$	−1.434127145	−1.197464788			
$Y_{0,2} \times 10^6$	−6.120747566	−5.592963902	−1.33508	−1.19597	−0.199030
$Y_{1,2} \times 10^9$	0.9449843095	0.8442508999	−1.617	−1.1226	−0.1864
$Y_{2,2} \times 10^{10}$	−1.450768382	−1.267226959			−0.0292
$Y_{3,2} \times 10^{12}$	−2.027592559	−2.500209167			
$Y_{4,2} \times 10^{13}$	1.660533203	1.386508893			
$Y_{5,2} \times 10^{15}$	−4.714582132	−3.848820777			
$Y_{0,3} \times 10^{12}$	5.555886989	4.852556927	0.153		−0.00131
$Y_{1,3} \times 10^{13}$	−0.1512463732	−1.291667338			−0.00620
$Y_{2,3} \times 10^{15}$	− 1.471295100	1.228499217			

3.2.2 Carbon monosulfide (CS)

We produced the line list of the fundamental bands (7.2 μm~) and the first overtone bands (3.8 μm~) of $^{12}C^{32}S$ and $^{13}C^{32}S$. The line list was provided by Chandra et al. (1995), where the Dunham coefficients determined by Winkel et al. (1984) for $^{12}C^{32}S$ and by Todd & Olson (1979) for $^{13}C^{32}S$ were used. The Dunham coefficients are given in Table 3.1. for $^{12}C^{32}S$ and $^{13}C^{32}S$.

Chandra et al. (1995) applied the dipole moment function of $^{12}C^{32}S$ given by Botschwina & Sebald (1985) to both $^{12}C^{32}S$ and $^{13}C^{32}S$.

3.2.3 Silicon monosulfide (SiS)

We produced the line list of the first overtone bands (6.6 μm~) of $^{28}Si^{32}S$. The Dunham coefficients determined by Frum et al. (1990) were adopted (see Table 3.1). The dipole matrix element was given by Piñeiro et al. (1987) as -0.63×10^{-2} (Debye). The Hönl-London factor (S_J) is the same as that of CO.

3.2.4 CH radical

We calculated the line list of the fundamental bands of CH (3.3 μm~). The ground state of CH is $X^2\Pi$, i.e. the quantum number, Λ, which is corresponding to the case that the component of the electronic orbital angular momentum along the internuclear axis is 1, and the quantum number of the spin (S) is 1/2. This means the electronic term splits into two levels (doublet). In the case of the CH $X^2\Pi$, the electronic motion (spin and orbital) is coupled strongly to the line joining the nuclei (Hund's case (a)), the energy levels are represented by F_1 and F_2 for which rotational energy levels are defined. Further, the interaction between the rotation and the electronic orbital angular momentum causes the splitting into two components (Λ-type doubling) which are designated e and f. The term-diagram for the transition is presented in Figure 3.2.

The energy levels of the $^2\Pi$ state are calculated using the matrix element of the Hamiltonians presented by Amiot et al. (1981). We give the matrix element in Table 3.2. The molecular constants were determined by Zachwieja (1995) which are given in Table 3.3.

We adopted the dipole matrix elements derived by Lie et al. (1973). The f-values derived for the transitions with $\Delta v = 1$ are as follows;

$v' - v''$	$f \times 10^5$
1-0	2.78
2-1	5.88
3-2	9.15
4-3	12.1

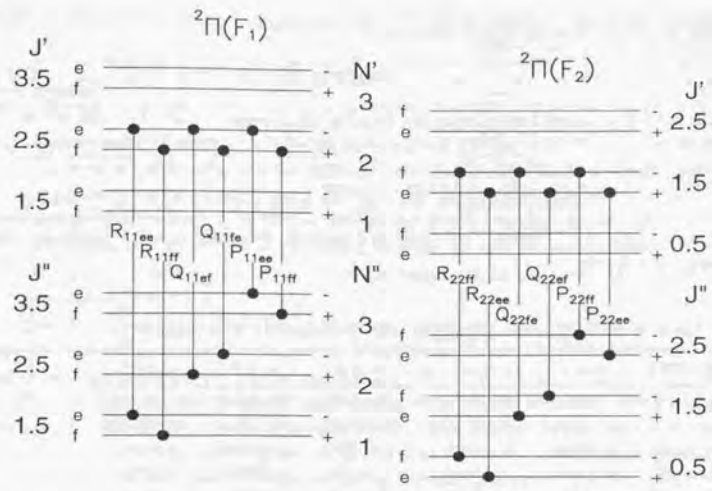

Figure 3.2: The term diagram of the CH $X^2\Pi$-$X^2\Pi$ transition

We applied the Hönl-London factors derived by Bennett (1970) to the calculation of the line intensities.

Table 3.2: Hamiltonian matrix elements for the CH $X^2\Pi$ state

$<^2\Pi_{3/2}\|^2\Pi_{3/2}>$	$T_v + 0.5A_v + B_v z - D_v z(z+1) + H_v z(z+1)(z+2) - L_v z(z+1)^2(z+4)$ $\mp 0.5 q_{D_v} z(J+0.5) \mp q_{H_v} z(J+0.5)^3 - 0.5\gamma_D z$
$<^2\Pi_{1/2}\|^2\Pi_{1/2}>$	$T_v - 0.5A_v + B_v(z+2) - D_v(z+1)(z+4) + H_v(z+1)(z^2+8z+8) - L_v(z+1)^2(z^2+12z+16)$ $\mp 0.5 p_{D_v}(J+0.5) \mp 0.5 p_D(J+0.5)(z+2) \mp q_v(J+0.5)$ $\mp 0.5 q_{D_v}(J+0.5)(3z+4) \mp 2q_{H_v}(z+2)(J+0.5)^3 - \gamma_v - 0.5\gamma_D(3z+4)$
$<^2\Pi_{3/2}\|^2\Pi_{1/2}>$	$-B_v\sqrt{z} + 2D_v\sqrt{z}(z+1) - H_v\sqrt{z}(z+1)(3z+4) + 4L_v\sqrt{z}(z+1)^2(z+2)$ $\pm 0.25 p_D\sqrt{z}(J+0.5) \pm 0.5 q_v\sqrt{z}(J+0.5)$ $\pm 0.5 q_{D_v}\sqrt{z}(z+2)(J+0.5) \pm 0.5 q_{H_v}\sqrt{z}(z+1)(J+0.5)^3 + 0.5\gamma_v\sqrt{z} + 0.5\gamma_D\sqrt{z}(z+2)$

$z = (J - \frac{1}{2})(J + \frac{1}{2})$. When two signs are quoted, the lower is for f levels and the upper for e levels.

Table 3.3: Molecular constants (in cm^{-1}) of the CH $X^2\Pi$ state

Constant	$v = 0$	$v = 1$	$v = 2$	$v = 3$	$v = 4$
T_v	0.0	2732.97771	5339.90308	7822.2187	10180.9981
B_v	14.192406	13.6618556	13.135933	12.613589	12.093160
$D_v \times 10^3$	1.46183	1.438687	1.417275	1.398003	1.38081
$H_v \times 10^7$	1.1668	1.13034	1.09272	1.04708	0.9707
$L_v \times 10^{11}$	1.459	1.4189	1.4312	1.4812	1.438
A_v	28.146724	28.3387	28.5287	28.6899	28.8854
$\gamma_v \times 10^2$	−2.565	−2.3910	−2.2297	−2.0906	−1.919
$\gamma_{D_v} \times 10^6$	8.56	8.285	8.23	8.46	7.55
$p_v \times 10^2$	3.351	3.162	3.038	2.898	2.767
$p_{D_v} \times 10^6$	−9.29	−7.92	−7.02	−6.04	−5.12
$q_v \times 10^2$	3.86724	3.72765	3.58977	3.45190	3.3103
$q_{D_v} \times 10^5$	−1.5127	−1.4744	−1.4357	−1.3974	−1.335
$q_{H_v} \times 10^9$	2.852	2.740	2.630	2.561	2.14

3.3 Electronic transition of diatomic molecules

3.3.1 C_2 Ballik-Ramsay system

There are three electronic transitions of C_2 in the optical and near infrared regions; the Swan system ($d^3\Pi_g$-$a^3\Pi_u$), the Phillips system ($A^1\Pi_u$-$X^1\Sigma_g^+$) and the Ballik-Ramsay system ($b^3\Sigma_g^-$-$a^3\Pi_u$). We discuss here the Ballik-Ramsay system among them because that is rather strong in the near infrared region where cool stars have the peak of radiation. The line list of the Ballik-Ramsay system in the near infrared region was produced in this work to examine the approximation of molecular opacities in the calculation of model photospheres in the calculation of model photospheres (Chapter 4).

The term-diagram for the Ballik-Ramsay system is shown in Figure 3.3. The lower state ($a^3\Pi_u$) is represented by the Hund's case (a) as the CH $X^2\Pi$ state, but has three spin components (triplet) denoted by $F_1(J'' = N'' + 1)$, $F_2(J'' = N'')$ and $F_3(J'' = N'' - 1)$. The Λ-doubling occurs in each J'' component. However, the levels with positive parity are missing because C_2 is a homonuclear molecule with zero nuclear spin. The missing levels due to this effect are shown by dotted lines in Figure 3.3. The upper $b^3\Sigma_g^-$ is, on the other hand, represented by the Hund's case (b), i.e. the coupling of spin to the internuclear axis is weak and three spin components exist for a given N' as F_1 ($J' = N' + 1$), F_3 ($J' = N' - 1$) and F_2 ($J' = N'$). As in the $a^3\Pi_u$ state, only those levels with positive total parity (odd rotational quantum number N') are present.

For calculating the energy levels, the Hamiltonian matrix elements presented by Islami & Amiot (1986) are used (see Table 3.4 and 3.5). We adopted the molecular constants determined by Amiot et al. (1979) for $v = 0$, 1, 2 and 3 and those by Davis et al. (1988) for $v = 4$. They are given in Table 3.6 and 3.7, respectively. The five vibrational transitions with $\Delta v = 3$, 2, 1, 0 and -1 were calculated. We neglected the lines of satellite branches because they are much weaker than those of main branches.

The line strengths were calculated using the dipole moments determined by Cooper & Nicholls (1975).

3.3.2 CN red system

The absorption of the CN in the near infrared region is important not only in analyzing the observed spectra themselves but also in calculating model atmospheres. We produced the line list of the CN red system ($A^2\Pi$-$X^2\Sigma^+$) for $\Delta v = -2, -1, 0, 1, 2$ to examine the approximation of molecular opacities in the calculation of model photospheres (Chapter 4).

The term-diagram for the CN red system is shown in Figure 3.4. The lower state ($X^3\Sigma^+$) is represented by the Hund's case (b) as C_2 $b^3\Sigma_g^-$ state. The upper state $A^2\Pi$ is represented by Hund's case (a) as the CH $X^2\Pi$ state. The energy levels are

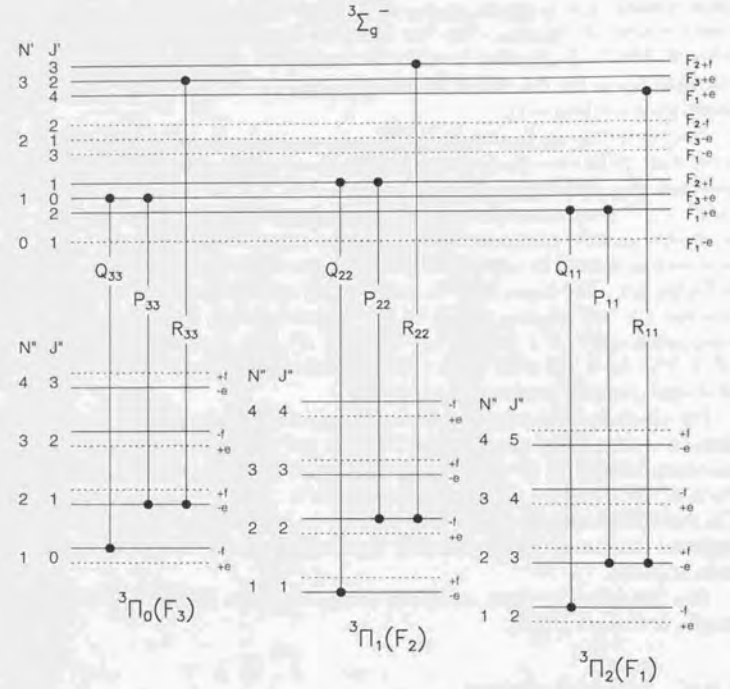

Figure 3.3: The term diagram of the C_2 $b^3\Sigma_g^-$-$a^3\Pi_u$ transition (the main branches). The dotted lines correspond to missing levels

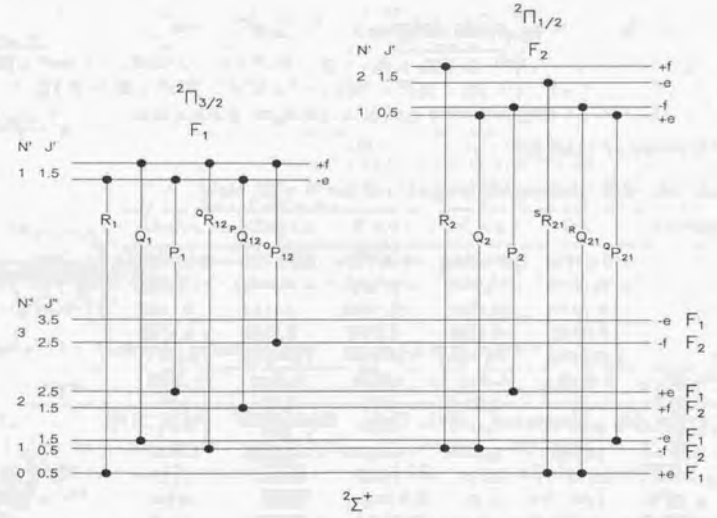

Figure 3.4: The term diagram of the CN $A^2\Pi$-$X^2\Sigma^+$ transition

Table 3.4: Hamiltonians matrix elements for the C_2 $a^3\Pi_u$ state

$<^3\Pi_0\|^3\Pi_0>$	$= T - A + \epsilon \pm o + B(x+1) - A_D(x+1) - D[(x+1)^2+2x] + H(x+1)(x^2+8x+1) + \frac{1}{4}qx + \frac{1}{2}(1\mp1)(q+p)$
$<^3\Pi_1\|^3\Pi_1>$	$= T - 2\epsilon + B(x+1) - D(x^2+6x-3) + H(x^3+15x^2-5x+5) + \frac{1}{4}q(1\mp1)x + \frac{1}{2}(q+p)$
$<^3\Pi_2\|^3\Pi_2>$	$= T + A + \epsilon + B(x-3) + A_D(x-3) - D(x^2-4x+5) + H(x^3-3x^2+5x-7) + \frac{1}{4}q(x-2)$
$<^3\Pi_1\|^3\Pi_0>$	$= -\sqrt{2x}[B - \frac{1}{2}A_D - 2D(x+1) + H(3x^2+10x-1) - \frac{1}{2}\gamma + \frac{1}{4}q \mp \frac{1}{2}q + \frac{1}{8}p \mp \frac{1}{4}p]$
$<^3\Pi_2\|^3\Pi_1>$	$= -\sqrt{2(x-2)}[B + \frac{1}{2}A_D - 2D(x-1) + H(3x^2-2x+3) - \frac{1}{2}\gamma + \frac{1}{4}q + \frac{1}{8}p]$
$<^3\Pi_0\|^3\Pi_2>$	$= \sqrt{x(x-2)}[-2D + 2H(3x-1) \mp \frac{1}{4}q]$

$x = J(J+1), p = p_0 + p_J J(J+1), q = q_0 + q_J J(J+1), \epsilon = \epsilon_0 + \epsilon_J J(J+1)$ and $\gamma = \gamma_0 + \gamma_J J(J+1)$. When a sign is given, the upper one refers to e sublevels and the lower one to f sublevels.

Table 3.5: Hamiltonians matrix elements for the C_2 $b^3\Sigma_g^-$ state

$<^3\Sigma_0^-\|^3\Sigma_0^->$	$= \frac{1}{2}(1\pm1)[T - 2\epsilon - 2\gamma + B(x+2) - D(x^2+8x+4) + H(x^3+18x^2+28x+8)]$
$<^3\Sigma_1^-\|^3\Sigma_1^->$	$= T + \epsilon - \gamma + Bx - D[x^2+2x(1\pm1)] + H[x^3+2(3x^2+2x)(1\pm1)]$
$<^3\Sigma_0^-\|^3\Sigma_1^->$	$= \frac{1}{2}(1\pm1)\sqrt{x}[2B - \gamma - 4D(x+1) + H(6x^2+20x+8)]$

See footnote of Table 3.4

Table 3.6: Molecular constants (cm^{-1}) of the C_2 $a^3\Pi_u$ state

Constant	$v=0$	$v=1$	$v=2$	$v=3$	$v=4$
T	1536.0731	3154.0853	4748.7704	6320.1221	7868.1507
A	−15.2629	−15.2434	−15.2304	−15.1978	−15.1986
ϵ	−0.1049	−0.1096	−0.1083	−0.1115	−0.1036
o	−0.6743	−0.6702	−0.6582	−0.6556	−0.6537
B	1.624254	1.607668	1.591035	1.574365	1.557611
$D \times 10^6$	6.4405	6.4511	6.4636	6.4846	6.5001
$H \times 10^{12}$	2.59	2.03	1.25	0.00	0.00
$p_0 \times 10^3$	4.55	5.17	5.20	7.28	8.61
$q_0 \times 10^3$	−1.0559	−1.1659	−1.3023	−1.5185	1.8640
$A_D \times 10^4$	3.779	3.618	3.486	3.558	4.170
$\epsilon_J \times 10^6$	1.85	4.13	3.01	5.09	6.15
$p_J \times 10^8$	−6.5	−9.9	−17.8	−31.1	−31.7
$q_J \times 10^8$	3.99	5.09	6.51	10.10	17.71
$o_J \times 10^6$	2.19	2.47	0.0	0.0	0.0

Table 3.7: Molecular constants (cm^{-1}) of the C_2 $b^3\Sigma_g^-$ state

Constant	$v=0$	$v=1$	$v=2$	$v=3$	$v=4$
T	7168.18	8616.3078	10042.2742	11446.1374	12827.9830
B	1.490484	1.474168	1.457833	1.441496	1.425161
$D \times 10^6$	6.1990	6.2072	6.2151	6.2249	6.2432
ϵ	0.1014	0.1064	0.1064	0.1023	0.1032
$\gamma \times 10^3$	−1.498	−1.668	−1.771	−1.765	−1.659

Table 3.8: Molecular constants (cm^{-1}) of the CN $X^2\Sigma^+$ state

Constant	$v=0$	$v=1$	$v=2$	$v=3$	$v=4$
T_0	0.0	2042.42261	4058.55176	6048.34766	8011.7734
B	1.8910827	1.8736591	1.8561802	1.8386440	1.8210468
$D \times 10^5$	0.64072	0.64162	0.64263	0.64367	0.64445
$H \times 10^{11}$	0.636	0.608	0.585	0.547	0.380
$\gamma_0 \times 10^2$	0.7417	0.7367	0.7272	0.7190	0.7212
$\gamma_J \times 10^7$	−0.70	−0.96	−0.97	−0.96	−3.0
$\gamma_{JJ} \times 10^{11}$	0.16	0.45	0.45	0.0	7.8

Table 3.9: Hamiltonians matrix elements for the CN $^2\Pi$ state

$<^2\Pi_{1/2}\|^2\Pi_{1/2}>$	$= T_0 + \frac{1}{4}A_0 - \frac{1}{2}\gamma - \frac{1}{2}A + (B - A_J)(x+1) - D[(x+1)^2+x] + H[(x+1)^3+x(3x+1)]$ $-\frac{1}{2}A_{JJ}[3(x+1)^2+x] + \frac{1}{2}p(1\mp\sqrt{x+1}) + \frac{1}{2}q(x+2\mp2\sqrt{x+1}) + o$
$<^2\Pi_{3/2}\|^2\Pi_{3/2}>$	$= T_0 + \frac{1}{4}A_0 - \frac{1}{2}\gamma + \frac{1}{2}A + (B + A_J)(x-1) - D[(x-1)^2+x] + H[(x-1)^3+x(3x-1)]$ $+\frac{1}{2}A_{JJ}[3(x-1)^2+x] + \frac{1}{2}qx$
$<^2\Pi_{1/2}\|^2\Pi_{3/2}>$	$= -B\sqrt{x} + 2Dx\sqrt{x} + \frac{1}{2}\gamma\sqrt{x} - H\sqrt{x}(3x^2+x+1)$ $+A_{JJ}\sqrt{x} - \frac{1}{4}p\sqrt{x} + \frac{1}{2}q\sqrt{x}(-1\pm\sqrt{x+1})$

$x = (J - \frac{1}{2})(J + \frac{3}{2}), p = p_0 + p_J J(J+1) + p_{JJ}[J(J+1)]^2, q = q_0 + q_J J(J+1) + q_{JJ}[J(J+1)]^2$

Table 3.10: Molecular constants (cm^{-1}) of the CN $A^2\Pi$ state

Constant	$v=0$	$v=1$	$v=2$	$v=3$	$v=4$
T_0	9117.39268	10905.10365	12667.24425	14403.8029	16114.7716
A	−52.65010	−52.57602	−52.50026	−52.4289	−52.3705
$A_J \times 10^4$	0.177	0.176	0.180	0.250	0.473
$A_{JJ} \times 10^9$	−0.74	−0.49	0.0	0.0	0.0
B	1.7073145	1.6900415	1.6727238	1.6553535	1.637902
$D \times 10^5$	0.61497	0.61613	0.61746	0.61877	0.6166
$H \times 10^{11}$	0.406	0.375	0.354	0.372	−0.51
$p_0 \times 10^2$	0.8409	0.8400	0.8347	0.858	0.759
$p_J \times 10^6$	−0.2708	−0.2916	−0.315	−0.386	0.0
$q_0 \times 10^3$	−0.38961	−0.39772	−0.4084	−0.4160	−0.4112
$q_J \times 10^7$	0.1082	0.1146	0.1382	0.135	0.0
$q_J \times 10^{13}$	−0.97	−0.95	−0.38	0.0	0.0

calculated using the molecular constants and the formula derived by Cerny et al. (1978). The ground state $X^2\Sigma^+$ is described by the terms

$$F_1(N) = BN(N+1) - D[N(N+1)]^2 + H[N(N+1)]^3 + \frac{1}{2}\gamma N \quad (3.5)$$

$$F_2(N) = BN(N+1) - D[N(N+1)]^2 + H[N(N+1)]^3 - \frac{1}{2}\gamma(N+1), \quad (3.6)$$

where $N = J - \frac{1}{2}$ and $N = J + \frac{1}{2}$ for $F_1(N)$ and $F_2(N)$, respectively. γ represents the spin doubling of the $^2\Sigma^+$ and given by the expansion

$$\gamma = \gamma_0 + \gamma_J N(N+1) + \gamma_{JJ}[N(N+1)]^2. \quad (3.7)$$

Molecular constants are given in Table 3.8.

In the calculation of the state $A^2\Pi$, the matrix elements and the molecular constants given by Cerny et al. (1978) are used (see Table 3.9 and 3.10, respectively).

We calculated not only the main branches ($P_1, Q_1, ...$) but also the satellite branches ($^OP_{12}, ^PQ_{12}, ...$). We used the Einstein coefficients for the CN red system derived by Bauschlicher et al. (1988) for the band strengths.

3.4 Vibration-rotation transition of polyatomic molecules

3.4.1 Hydrogen cyanide (HCN)

HCN is an asymmetric linear molecule and has three normal vibrations as shown in Figure 3.5. We define ν_1 and ν_3 as the CH-stretching vibration and the CN-stretching vibration, respectively, as defined by Maki et al. (1996). There are combination bands in addition to normal vibration bands.

The bending mode (ν_2) of HCN is the doubly degenerate vibration. In this case, the quantum number l is defined as $l = v_2, v_2 - 2, ..., 1$ or 0 which denotes the vibrational angular momentum about the symmetry axis. Thus the vibrational energy levels are defined by v_1, v_2, v_3 and l. The energy states are denoted as $\Sigma, \Pi, \Delta, ...$ corresponding to $l = 0, 1, 2, ...$.

Further, if the molecule is rotationally excited, the energy levels with $l \geq 1$ split into two sublevels by the interaction with rotation (l-type doubling). As a result, there are v_2+1 energy levels for v_2 state.

Transitions are allowed for $\Delta l = 0$ or ± 1. Transitions with $\Delta l = 0$ are called the parallel-bands ($\parallel$ bands) and have no or very weak Q branch (e.g. the ν_1 bands at 3 μm, the $2\nu_2$ bands at 7 μm). Transitions with $\Delta l = \pm 1$ are called the perpendicular bands ($\perp$ bands) and have strong Q branches (e.g. the $\nu_2 + \nu_3$ bands at 3.6 μm, the ν_2 bands at 14 μm).

The formula to calculate the energy levels of HCN are given in Maki et al. (1996) and Maki & Lide (1967). The energy levels are presented as the sum of the rotational and vibrational energy;

$$E^0 = G_V + B_V J(J+1) - D_V[J(J+1) - l^2]^2 + H_V[J(J+1) - l^2]^3 \quad (3.8)$$

where G_V is the vibrational energy. The vibrational term, G_V, is represented by the expansion

$$\begin{aligned} G_V &= \sum \omega_i (v_i + d_i/2) + \sum\sum x_{ij}(v_i + d_i/2)(v_j + d_j/2) + g_{22} l^2 \\ &\quad + \sum\sum\sum y_{ijk}(v_i + d_i/2)(v_j + d_j/2)(v_k + d_k/2) \\ &\quad + \sum y_{ll}(v_i + d_i/2) l^2. \end{aligned} \quad (3.9)$$

In this and following equations, the sums are over all values of the subscript 1 to 3 with the exception that $k \geq j \geq i$. The vibrational degeneracy is given by $d_1 = d_3 = 1$ and $d_2 = 2$ for HCN. We neglected the terms with higher order of v which are given in Maki et al. (1996). B_V, D_V and H_V are presented as follows;

$$B_V = B_e - \sum \alpha_i (v_i + d_i/2) + \sum\sum \gamma_{ij}(v_i + d_i/2)(v_j + d_j/2) + \gamma_{ll} l^2$$

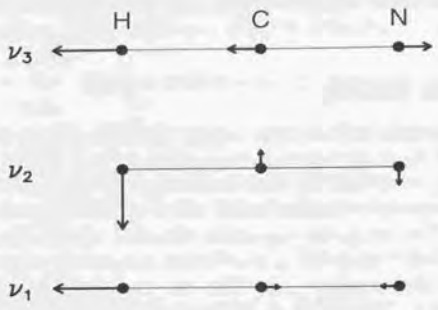

Figure 3.5: Form of the normal vibrations of HCN

$$+ \sum\sum\sum \gamma_{ijk}(v_i + d_i/2)(v_j + d_j/2)(v_k + d_k/2)$$
$$+ \gamma_{ill}(v_i + d_i/2)l^2, \tag{3.10}$$

$$D_V = D_e + \sum \beta_i(v_i + d_i/2) + \sum\sum \beta_{ij}(v_i + d_i/2)(v_j + d_j/2) + \beta_{ll}l^2, \tag{3.11}$$

and

$$H_V = H_e + \sum \epsilon_i(v_i + d_i/2) + \epsilon_{ll}l^2. \tag{3.12}$$

The molecular constants determined by Maki et al. (1996) are given in Tables 3.11 and 3.12.

The energy levels for v_2=0 state is given by E^0 itself. However, for v_2=1 states, it is necessary to add to E^0 the term

$$\pm\frac{1}{2}[q_V - q_{VJ}J(J+1)]J(J+1), \tag{3.13}$$

where q_{VJ},q_{VJJ} are given by the expansions

$$q_V = q_e + \sum \pi_i(v_i + d_i/2) + \sum\sum \pi_{ij}(v_i + d_i/2)(v_j + d_j/2) + \pi_{ll}l^2, \tag{3.14}$$

$$q_{VJ} = q_{eJ} + \sum \mu_i(v_i + d_i/2) + \sum\sum \mu_{ij}(v_i + d_i/2)(v_j + d_j/2) + \mu_{ll}l^2. \tag{3.15}$$

The molecular constants are presented in Table 3.13

For v_2 =2, 3 and 4, the energy levels are calculated by solving the secular determinants given by Maki & Lide (1967) which are presented as follows;

$$\begin{vmatrix} E^0_\Delta - \epsilon & W_{20} & W_{22} \\ W_{20} & E^0_\Sigma - \epsilon & W_{20} \\ W_{22} & W_{20} & E^0_\Delta - \epsilon \end{vmatrix} = 0 \quad \text{for} \quad v_2 = 2,$$

$$\begin{vmatrix} E^0_\Phi - \epsilon & W_{31} & W_{3,-1} & 0 \\ W_{31} & E^0_\Pi - \epsilon & W_{11} & W_{3,-1} \\ W_{3,-1} & W_{11} & E^0_\Pi - \epsilon & W_{31} \\ 0 & W_{3,-1} & W_{31} & E^0_\Phi - \epsilon \end{vmatrix} = 0 \quad \text{for} \quad v_2 = 3,$$

$$\begin{vmatrix} E^0_\Gamma - \epsilon & W_{42} & \sqrt{2}W_{40} \\ W_{42} & E^0_\Delta + W_{2,-2} - \epsilon & \sqrt{2}W_{02} \\ \sqrt{2}W_{40} & \sqrt{2}W_{02} & E^0_\Sigma - \epsilon \end{vmatrix} = 0 \quad \text{and}$$

$$\begin{vmatrix} E^0_\Delta - W_{2,-2} - \epsilon & W_{42} \\ W_{42} & E^0_\Gamma - \epsilon \end{vmatrix} = 0 \quad \text{for} \quad v_2 = 4.$$

The matrix elements (W's) are given in Table 3.14.

For the calculation of line intensities of HCN, we used the transition dipoles, the vibrational and rotational intensity factors, and the Herman-Wallis factors (correction for the interaction between rotation and vibration) derived by Maki et al. (1995).

We calculated the transitions 100-000 (ν_1), 011-000 ($\nu_2 + \nu_3$), 100-010 ($\nu_1 - \nu_2$), 010-000 (ν_2), 020-000 ($2\nu_2$) and their hot bands. While the calculations were done for $v_2 \leq 4$ for perpendicular bands, the parallel bands of HCN (ν_1 and $2\nu_2$) for the higher v_2 were also calculated by regarding the l-type splitting as a degeneracy, because the accuracy of line positions is not so important for these bands which do not have strong Q branches.

Table 3.11: Molecular constants for the vibrational energy levels of HCN

parameter	(in cm^{-1})	parameter	(in cm^{-1})
ω_1	3443.08076	y_{111}	0.447836
ω_2	726.96074	y_{222}	0.021381
ω_3	2127.41201	y_{333}	−0.039269
x_{11}	−53.203496	y_{112}	−0.113845
x_{22}	−2.599847	y_{122}	−0.077350
x_{33}	−10.091733	y_{113}	−0.464875
x_{12}	−18.939592	y_{133}	0.157604
x_{13}	−13.910718	y_{123}	0.097544
x_{23}	−3.209492	y_{233}	−0.120962
g_{22}	5.314057	y_{223}	0.092102
		y_{11l}	−0.035176
		y_{22l}	0.004273
		y_{33l}	−0.121280

Table 3.12: Rotational constants for HCN

parameter	(in $cm^{-1} \times 10^{-3}$)	parameter	(in cm^{-1})	parameter	(in cm^{-1})
B_e	1484.780811	$D_e \times 10^6$	2.85297	$H_e \times 10^{12}$	2.458
α_1	10.43529	$\beta_1 \times 10^8$	−3.4091	$\epsilon_1 \times 10^{12}$	0.284
α_2	−3.57440	$\beta_2 \times 10^8$	6.7957	$\epsilon_2 \times 10^{12}$	0.857
α_3	10.00284	$\beta_3 \times 10^8$	0.5296	$\epsilon_3 \times 10^{12}$	−0.083
γ_{11}	−0.145020	$\beta_{11} \times 10^9$	0.494	$\epsilon_{ll} \times 10^{12}$	−0.146
γ_{22}	0.043053	$\beta_{22} \times 10^9$	0.740		
γ_{33}	−0.029179	$\beta_{33} \times 10^9$	0.078		
γ_{12}	0.195899	$\beta_{12} \times 10^9$	5.577		
γ_{13}	0.196127	$\beta_{13} \times 10^9$	4.575		
γ_{23}	−0.120675	$\beta_{23} \times 10^9$	−1.700		
γ_{ll}	−0.190750	$\beta_{ll} \times 10^9$	−4.643		
γ_{111}	−0.0015528				
γ_{222}	0.0011645				
γ_{333}	0.0				
γ_{112}	0.0				
γ_{122}	0.0034568				
γ_{113}	0.0027397				
γ_{133}	0.0				
γ_{123}	0.0133458				
γ_{233}	0.0				
γ_{223}	−0.0032349				
γ_{11l}	−0.0021490				
γ_{22l}	−0.0058495				
γ_{33l}	0.0034167				

Table 3.13: The vibrational expansion coefficients for the l-type resonance constants for HCN

parameter	(in cm^{-1})	parameter	(in cm^{-1})
$q_e \times 10^3$	7.229679	$q_{eJ} \times 10^8$	7.556
$\pi_1 \times 10^3$	0.0885	$\mu_1 \times 10^8$	0.649
$\pi_2 \times 10^3$	0.10116	$\mu_2 \times 10^8$	0.528
$\pi_3 \times 10^3$	−0.0183	$\mu_3 \times 10^8$	−0.185
$\pi_{11} \times 10^4$	−0.1626	$\mu_{11} \times 10^8$	−0.094
$\pi_{22} \times 10^4$	0.01764	$\mu_{22} \times 10^8$	0.0023
$\pi_{33} \times 10^4$	−0.0068	$\mu_{33} \times 10^8$	0.0560
$\pi_{12} \times 10^4$	0.11840	$\mu_{12} \times 10^8$	0.026
$\pi_{13} \times 10^4$	0.7903	$\mu_{13} \times 10^8$	0.465
$\pi_{23} \times 10^4$	−0.1378	$\mu_{23} \times 10^8$	−0.108
$\pi_{ll} \times 10^4$	−0.0090	$\mu_{ll} \times 10^8$	−0.072

Table 3.14: Matrix elements used in the seqular determinants

$W_{22} =< 2,2|H|2,-2 >= \rho[J^2(J+1)^2 - 2J(J+1)]/2$

$W_{20} =< 2,2|H|2,0 >= q[J^2(J+1)^2 - 2J(J+1)]^{1/2}/\sqrt{2}$

$W_{31} =< 3,3|H|3,1 >= \sqrt{3}q[J^2(J+1)^2 - 8J(J+1) + 12]^{1/2}/2$

$W_{3,-1} =< 3,3|H|3,-1 >= \sqrt{3}\rho J(J+1)[J^2(J+1)^2 - 8J(J+1) + 12]^{1/2}/2$

$W_{11} =< 3,1|H|3,-1 >= qJ(J+1)$

$W_{42} =< 4,4|H|4,2 >= q[J^2(J+1)^2 - 18J(J+1) + 72]^{1/2}$

$W_{2,-2} =< 4,2|H|4,-2 >= 3\rho J(J+1)[J(J+1) - 2]/2$

$W_{02} =< 4,2|H|4,0 >= \sqrt{6}q[J^2(J+1)^2 - 2J(J+1)]^{1/2}/2$

$W_{40} =< 4,4|H|4,0 >= \sqrt{6}\rho[J^2(J+1)^2 - 18J(J+1) + 72]^{1/2}[J^2(J+1)^2 - 2J(J+1)]^{1/2}/2$

$q = q_V - q_{VJ}J(J+1)$ and $\rho = -1.085\,cm^{-1}$

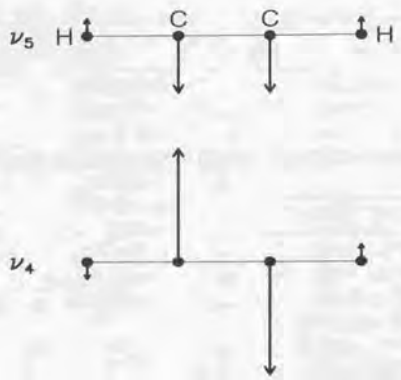

Figure 3.6: Form of the normal bending vibrations of C_2H_2

3.4.2 Acetylene (C_2H_2)

C_2H_2 is a symmetric linear molecule and has five normal vibrations. In Figure 3.6, we show the two bending vibrations (ν_4 and ν_5). In this work, we only discuss the bending mode of ν_5 near 13.7 μm. Then we briefly describe the calculation of the line list of this band.

C_2H_2 has degenerate bending modes of vibration as HCN. However, C_2H_2 is characterized by two degenerate vibrations and the quantum number for the total vibrational angular momentum $k(=l_4+l_5)$ should be considered. A full Hamiltonian representing bending energy levels up to four quanta in $V_4 + V_5 \leq 4$ was presented by Herman et al. (1991). We calculate the energy levels by their Hamiltonian using the molecular constants determined by Kabbadj et al. (1991).

For the calculation of line intensities of C_2H_2, we used the transition dipoles, the vibrational and rotational intensity factors, Herman-Wallis factors, and Hönl-London factors derived by Weber et al. (1994). However, the factors derived by Weber et al. are not enough to calculate the line intensities for high excitation bands. Therefore our calculation was limited to the transitions within $V_4 + V_5 \leq 3$.

References

Amiot C., Chauville J., Maillard J. -P., 1979, J. Mol. Spectrosc. 75, 19
Amiot C., Maillard J. -P., Chauville J., 1981, J. Mol. Spectrosc. 87, 196
Bauschlicher C. W. Jr., Langhoff S. R., Taylor P.R., 1988, ApJ 332, 531
Bennett R. J. M., 1970, MNRAS 147, 35
Botschwina P., Sebald P., 1985, J. Mol. Spectrosc. 110, 1
Cerny D., Bacis R., Guelachvili G., Roux F., 1978, J. Mol. Spectrosc. 73, 154
Chackerian C., Tipping R. H., 1983, J. Mol. Spectrosc. 99, 431
Chandra S., Kegel W.H., Le Roy R.J., Hertenstein T., 1995, A&AS 114, 175
Cooper D. M., Nicholls R. W., 1975, J. Quant. Spectrosc. Rad. Transf. 15, 139
Davis S. P., Abrams M. C., Sandalphon, Brault J. W., Rao M. L. P., 1988, J. Opt. Soc. Am. B., 5, 1838
Frum C.I., Engleman R., Bernath P.F., 1990, J. Chem. Phys. 93, 5457
Guelachvili G., de Villeneuve D., Farrenq R., Urban W., Verges J., 1983, J. Mol. Spectrosc., 98, 64
Herman M., Huet T. R., Kabbadj Y., Auwera J. V., 1991, Molecular Physics 72, 75
Herzberg G., 1945, *Molecular Spectra and Molecular Structure. II., Infrared and Raman Spectra of Polyatomic Molecules*, Van Nostrand Reinhold Company, New York.
Herzberg G., 1950, *Molecular Spectra and Molecular Structure. I., Spectra of Diatomic Molecules*, Van Nostrand Reinhold Company, New York.
Islami K., Amiot C., 1986, J. Mol. Spectrosc. 118, 132
Kabbadj Y., Herman M., Di Lonardo G., Fusina L., Johns J. W. C., 1991, J. Mol. Spectrosc. 150, 535
Lie G. C., Hinze J., Liu B., 1973, J. Chem. Phys. 59, 1887
Maki A. G., Lide D. R., 1967, J. Chem. Phys. 47, 3206
Maki A., Quapp W., Klee S., 1995, J. Mol. Spectrosc. 171, 420
Maki A., Quapp W., Klee S., Mellau G. -C., Albert S., 1996, J. Mol. Spectrosc. 180, 323
Piñeiro A. L., Tipping R. H., Chackerian C., 1987, J. Mol. Spectrosc 125, 184
Tsuji T., 1986, A&A 156, 8
Todd T. R., Olson W. B., 1979, J. Mol. Spectrosc. 74, 190
Weber M., Blass W. E., Halsey G. W., Hillman J. J., 1994, J. Mol. Spectrosc. 165,107
Winkel R. J., Davis S. P., Pecyner R. Brault J. W., 1984, Can. J. Phys. 62, 1414
Zachwieja M., 1995, J. Mol. Spectrosc. 170, 285

Chapter 4

Model photospheres of carbon stars

4.1 Introduction

In the present study, we used model photospheres to analyze the molecular features of carbon stars (Chapter 5). Since absorption features are quite complicated in cool stars, synthetic spectra based on model photospheres are useful even for identification of molecular features. We will also discuss the dependence of molecular features on spectral types using model photospheres.

We calculated model photospheres of carbon stars based on the plane-parallel geometry and hydrostatic equilibrium. For detailed and quantitative analyses of the spectra, the sphericity effect should be taken into account. However, the effect in carbon stars are probably much smaller than in oxygen-rich giants (see Section 5.4). Hence we neglect the sphericity effect in the model calculation in this work. The effect of dynamics in atmospheres by stellar pulsation has been studied (e.g. Höfner & Dorfi 1997) and this possibility will be discussed in Section 5.4.

Since the spectrum and photospheric structure of red giants are dominated by the molecular processes, the careful evaluation of the molecular line opacities is indispensable in the calculation of model photospheres. We can of course evaluate molecular line opacities directly using the line lists, and will actually demonstrate the synthetic spectra based on line-by-line calculation for several molecular bands in Chapter 5. However, the number of molecular lines is so large that the line-by-line calculation is unrealistic to produce model photospheres for which we need to iterate the evaluation of molecular line opacities until the self-consistent temperature structure is obtained on the assumption of radiative equilibrium. Therefore some approximation for molecular opacities is necessary for model calculations. The approximate method usually used in modeling of stellar photospheres is the opacity distribution function method (ODF) or opacity sampling method (OS), both of which are based on huge line data of molecules (e.g. Gustafsson et al. 1975, Peytremann 1974). However, in our calculation of model photospheres of carbon stars, the evaluation of molecular line opacities was done by the band model method which was reviewed by Tsuji (1994). One advantage of the band model method against ODF and OS is its flexibility, because this method does not require a huge table of opacity prior to model calculation which is necessary for OS and ODF, but requires only a few spectroscopic constants of molecular bands. Therefore we can produce model photospheres for various chemical composition. This flexibility is important for studying carbon stars, because the C/O ratio of carbon stars are diverse and the photospheric structures severely depend on the C/O ratio.

Since the approximation by the band model method may be rather rough (see Section 4.2), it is necessary to examine how well this method represents the molecular line opacities. For this purpose we compared the spectra calculated by the band model method and the synthetic spectra based on the direct line-by-line calculation using the molecular line lists produced in Chapter 3.

The band model method for carbon bearing molecules is briefly reviewed in Section 4.2. In Section 4.3, we compare the synthetic spectra by the band model method with those based on the line-by-line calculation. The model photospheres calculated are discussed in Section 4.4.

4.2 Application of band model method to carbon bearing molecules

In this section we briefly describe the band model method and the application to absorption bands of CO, C_2, CN and HCN. The concept and formulation of band model method were reviewed by Tsuji (1994). Then we briefly summarize the formulae, and describe rather details on the determination of parameters in the band model method.

In the calculation of model photospheres, the molecular opacities are required for each spectral mesh and for each layer of the photosphere. Namely we need to evaluate the molecular opacities as a function of wavenumber ω and temperature T.

Contrary to atomic lines, the line intensity and line density of molecules can be estimated by simple formulae for each band of a molecule if the spectral mesh and temperature are specified. As a simple example, we here consider one vibrational transition of one species.

The line position (wavenumber ω) of the band can be represented by

$$\omega = \omega_{v'v''} + (B'_v + B''_v)m + (B'_v - B''_v)m^2, \tag{4.1}$$

where $m = -J$ for the P branch and $m = J + 1$ for the R branch, and by

$$\omega = \omega_{v'v''} + (B'_v - B''_v)m(m+1), \tag{4.2}$$

where $m = J$ for the Q branch. These equations can be solved for m.

The integrated line intensity for a single line is represented by

$$S_{v'v''}(m) = \frac{\pi e^2}{m_e c^2} f_{v'v''} \frac{\omega}{\omega_{v'v''}} |m| F(m) \exp[-\frac{hc}{kT}\{G''_v + B'_v|m(m-1)|\}] \times [1 - \exp(-\frac{hc\omega}{kT})]/Q_r(T)Q_v(T), \tag{4.3}$$

where $f_{v'v''}$ is the vibrational f-value, $F(m)$ is the Herman-Wallis factor, G''_v is the term value of the lower vibrational level, $Q_r(T)$ and $Q_v(T)$ are the rotational and vibrational partition functions, respectively, and other notations have their usual meanings. Since m is determined by eqs. (4.1) or (4.2) when ω is given, $S_{v'v''}$ can be written as a function of ω and T.

The line separation in the (v', v'') band is evaluated by

$$d_{v'v''}(m) = \frac{d\omega}{dm} = (B'_v + B''_v) + 2(B'_v - B''_v)m, \tag{4.4}$$

and can also be written as a function of ω.

Thus the line intensity and the line separation are derived for the spectral mesh represented by ω and the layer of the photosphere with T.

By these $S_{v'v''}(\omega)$ and $d_{v'v''}(\omega)$, we define the straight mean absorption coefficient $(\bar{k})$ as

$$\bar{k} = (\frac{S}{\bar{d}}) = \sum_{v'v''}[\frac{S_{v'v''}(\omega)}{d_{v'v''}(\omega)}], \tag{4.5}$$

where the summation should be extended to all the bands that are contributing at the wavenumber (ω). Then, we define the effective mean line separation $(\bar{d}(\omega))$ by

$$\frac{1}{\bar{d}} = (\frac{S^{1/2}}{d})^2/(\frac{S}{\bar{d}}), \tag{4.6}$$

where $\frac{S^{1/2}}{d}$ is defined as

$$\frac{S^{1/2}}{d} = \sum_{v'v''}[\frac{S_{v'v''}(\omega)^{1/2}}{d_{v'v''}(\omega)}]. \tag{4.7}$$

If the line separation $\bar{d}$ is comparable to or smaller than the Doppler widths of absorption lines, which are usually about several kms^{-1} in photospheres of giants, the line absorption coefficient can be regarded as a quasi-continuous absorption and given by the straight mean absorption coefficient $(\bar{k})$ itself. This is usually called just overlapping line approximation (JOLA). This may be applicable to the line absorption coefficients of some polyatomic molecules like HCN and C_2H_2. However, the mean line separations are larger than the Doppler widths for most bands of diatomic molecules. Then the absorption coefficients should be overestimated if the JOLA is applied in the model calculation. In this case, band models such as the Voigt-Analogue Elsasser band model could be applied with the use of the mean absorption coefficient and the mean line separation (Tsuji 1971). Hence, the evaluation of the mean line separation is very important in the approximation of molecular opacities.

Similar formulation can be applied to electronic bands of diatomic molecules like C_2 and CN. The straight mean absorption coefficient is written by the band oscillator strength $f_{v'v''}$, the electronic partition function $Q_e(T)$, the statistical weight (g_e), the term value (T_e) of the lower electronic state, and other factors in eq. (4.3). This was presented by Tsuji (1994) where the distinction between the P, Q and R branches was neglected. The mean line separation is given by eq. (4.4), but that must be divided by the number of branches (e.g. three if there are the P, Q and R branches). Further, the line separation may be even smaller due to the splitting by the spin-orbital interaction and due to the Λ-type doubling. Namely the line separation given by eq. (4.4) should be divided by $n_{P,Q,R}(2S+1)(2-\delta_{\Lambda,0})$, where n_{PQR} is the number of branches, $2S+1$ is the splitting by the spin-orbital interaction, and $2-\delta_{\Lambda,0}$ is 2 if there is the Λ-doubling.

In the case of the CN red system ($A^2\Pi$-$X^2\Sigma^+$), the dividing factor is 6, because there are the P, Q and R branches and $2S+1$=2. We neglected the satellite branches in the approximation of molecular line opacities, because their lines are much weaker than those of main branches. Similarly, the dividing factor for the CN violet system ($B^2\Sigma$-$X^2\Sigma^+$) is 4.

In the case of the C_2 Swan band ($d^3\Pi_g$-$a^3\Pi_u$), the dividing factor is 6, because there are the P and R branches (the Q branch is very weak) and $2S+1$=3. The factor 9 and 3 are derived for the C_2 the Ballik-Ramsay system ($b^3\Sigma_g$-$a^3\Pi_u$) and the Phillips system ($b^1\Pi_u$-$a^1\Sigma_g^+$), respectively. However we must consider the missing levels for the C_2 Ballik-Ramsay and the Phillips systems (see Chapter 3) since C_2 is the homonuclear molecule with zero nuclear spin. Therefore the factors should be divided by 2 for these two systems.

The evaluation of the line separation of the electronic bands is rather complicated as shown above, in spite of the fact that the molecular absorption coefficients are strongly dependent on these values, especially in the case of diatomic molecules. Therefore we examine how well the band model method can represent the molecular line absorption coefficients in the next section.

4.3 Comparison with synthetic spectra based on line-by-line calculation

For examining to what extent the band model method can represent the molecular line absorption coefficients, we compared the emergent flux based on the band model method with the synthetic spectra directly calculated using the line lists. For this purpose, we calculated model photospheres based on the band model method described above. Based on these model photospheres, the synthetic spectra are calculated using the line list of molecules produced in the previous chapter.

We carried out this comparison for CO vibration-rotation bands, the CN red system, the C_2 Ballik-Ramsay system and the HCN ν_1 bands, which are very important opacity sources in the photospheres of cool carbon stars. It should be noted that the line lists of these molecules are not necessarily complete, especially for lines with high excitation potential, while the band model method considers relatively higher excitation bands. This should be taken into consideration in the following discussion.

CN red system

The synthetic spectrum based on the line-by-line calculation for the CN red system is shown in Figure 4.1a for $T_{\rm eff}$=3000K and C/O=1.1. The transitions with $\Delta v = -2, -1, 0, 1$ and 2 are included. The emergent fluxes based on our band model method and on the JOLA are shown by the solid and dotted lines, respectively, in Figure 4.1b. It is evident that the emergent flux based on the JOLA shows large deviation from the synthetic spectrum based on the line-by-line calculation, but the agreement is fairly improved by our band model method. We also show the logarithmic difference between the synthetic spectrum and the emergent flux based on our band model method in Figure 4.1c. We can see that the absorption bands of the synthetic spectra are well reproduced by the band model method. The absorption in the emergent flux based on the band model method is rather stronger at 1.3, 1.7 and 2.3 μm than the synthetic spectrum, but this is due to the incompleteness of the line list of CN used in the calculation of the synthetic spectrum. We note that the satellite branches are not considered in these calculations. Though the lines of satellite branches are weaker by about two orders of magnitude than those of main branches, these branches should be included for more accurate approximation. In order to examine the effect of the effective temperature and of the carbon abundance, we also show the comparison for $T_{\rm eff}$ = 3400K and C/O=1.1 (Figure 4.2), for $T_{\rm eff}$ = 3000K and C/O=1.01 (Figure 4.3), and for $T_{\rm eff}$ = 3000K and C/O=2.0 (Figure 4.4). We confirmed that the absorption bands of the synthetic spectra are also well reproduced by the band model method in these cases.

C_2 Ballik-Ramsay system

The synthetic spectrum calculated using the line list of the C_2 Ballik-Ramsay system is shown for $T_{\rm eff}$=3000K and C/O=1.1 in Figure 4.5a. The transitions with $\Delta v = -1, 0, 1, 2$ and 3 are included. The emergent fluxes based on our band model

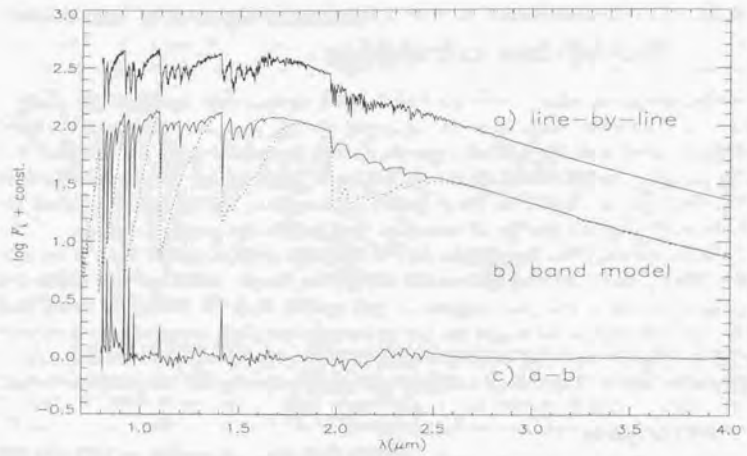

Figure 4.1: **a.** The synthetic spectrum of the CN red system for $T_{\rm eff}$=3000K and C/O=1.1. **b.** The emergent fluxes based on our band model method (solid line) and on the JOLA (dotted line). **c.** The logarithmic difference between the synthetic spectrum and the emergent flux based on our band model method

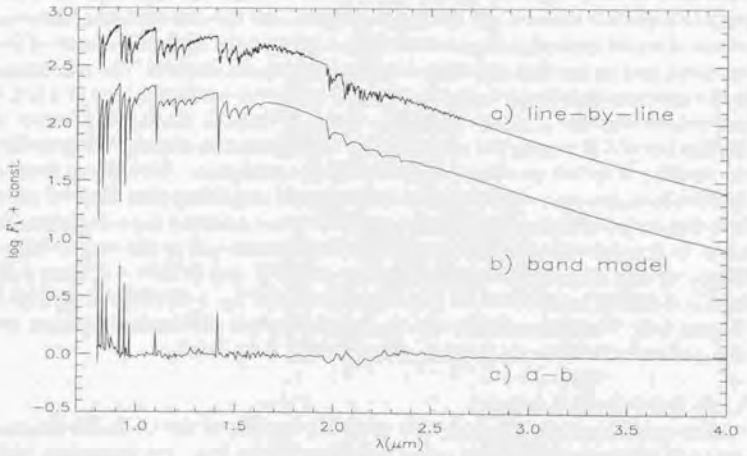

Figure 4.2: The same as Figure 4.1, but for $T_{\rm eff}$=3400K

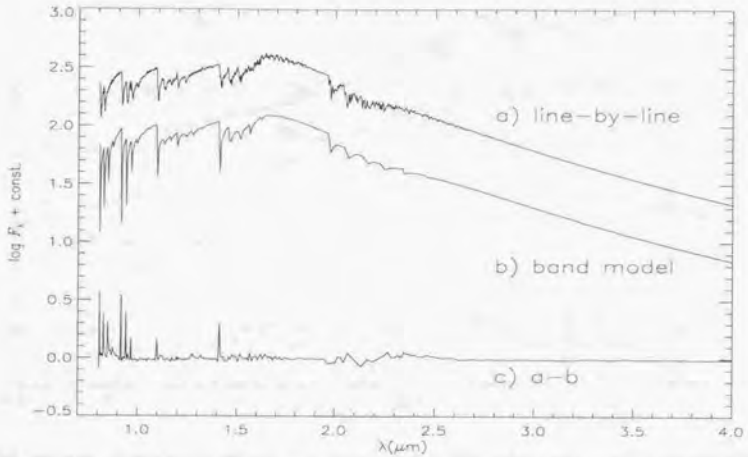

Figure 4.3: The same as Figure 4.1, but for C/O=1.01

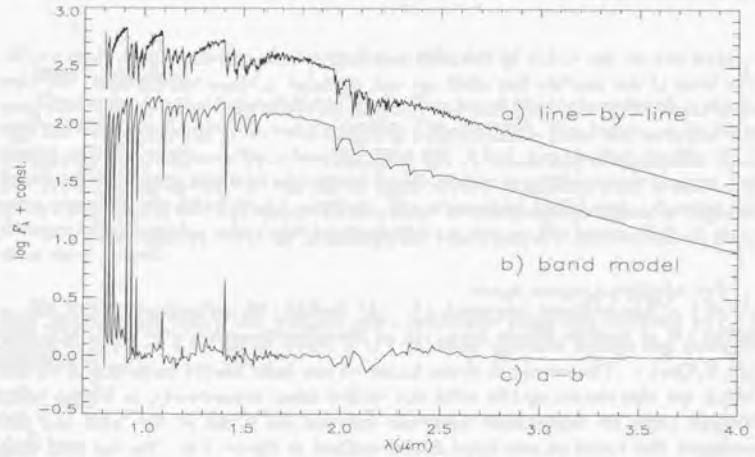

Figure 4.4: The same as Figure 4.1, but for C/O=2

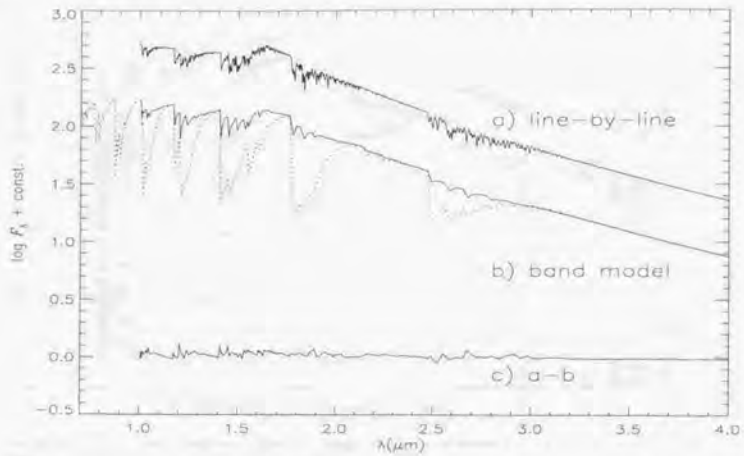

Figure 4.5: **a.** The synthetic spectrum of the C_2 Ballik-Ramsay system for $T_{\rm eff}$=3000K and C/O=1.1. **b.** The emergent fluxes based on our band model method (solid line) and on the JOLA (dotted line). **c.** The logarithmic difference between the synthetic spectrum and the emergent flux based on our band model method

method and on the JOLA by the solid and dotted lines, respectively, in Figure 4.5b. The lines of the satellite branches are not included in these calculations. We also show the logarithmic difference between the synthetic spectrum and the emergent flux based on our band model method in Figure 4.5c. As in the case of CN red system, the emergent flux based on the JOLA shows much stronger band absorption than that in the synthetic spectrum based on the line-by-line calculation, while the strength of the band absorption of the synthetic spectra are well reproduced by our band model method. We confirmed the agreement for other parameters.

CO vibration-rotation bands

The synthetic spectrum calculated using the line list of the fundamental, first overtone and second overtone bands of CO is shown in Figure 4.6a for $T_{\rm eff}$=3000K and C/O=1.1. The emergent fluxes based on our band model method and on the JOLA are also shown by the solid and dotted lines, respectively, in Figure 4.6b. We also show the logarithmic difference between the synthetic spectrum and the emergent flux based on our band model method in Figure 4.6c. We can find that the absorption bands of the synthetic spectrum are reasonably reproduced by our band model method. We confirmed the agreement for other parameters as the case of the CN red system.

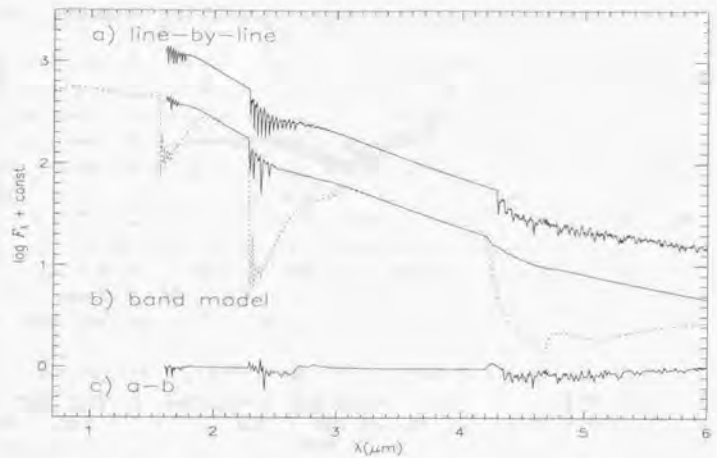

Figure 4.6: **a.** The synthetic spectrum of the CO vibration-rotation bands for $T_{\rm eff}$=3000K and C/O=1.1. **b.** The emergent fluxes based on our band model method (solid line) and on the JOLA (dotted line). **c.** The logarithmic difference between the synthetic spectrum and the emergent flux based on our band model method

HCN ν_1 bands

The synthetic spectrum calculated by the line list of the HCN ν_1 bands is shown in Figure 4.7 for $T_{\rm eff}$=3000K and C/O=1.1. The emergent flux based on the band model method is also shown. We note that the JOLA was applied for the HCN bands. We can see that the absorption bands of the synthetic spectrum are well reproduced by the band model method. The absorption at 2.5 and 3.6 μm in the emergent flux based on the band model method is due to the bands of HCN other than the ν_1 bands.

By these comparisons, we conclude that the molecular opacities of CO, CN, C_2 and HCN are reasonably approximated by the band model method in our model calculation.

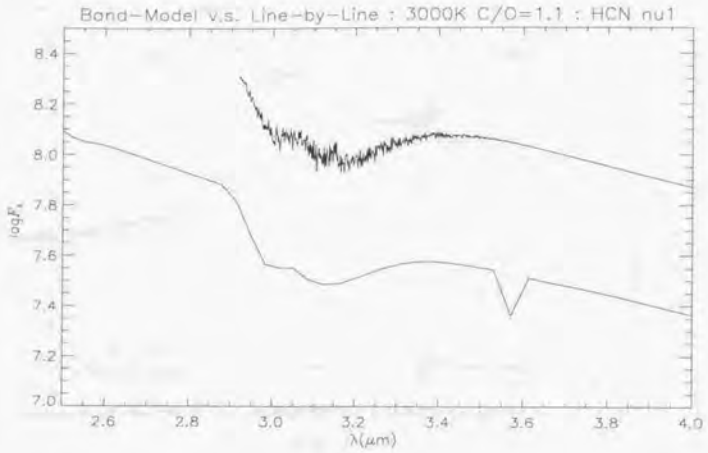

Figure 4.7: The upper spectrum is the synthetic spectrum of the HCN ν_1 bands for $T_{\rm eff}$=3000K and C/O=1.1. The lower one is the emergent flux based on the band model method. The absorption at 2.5 and 3.6 μm in the emergent flux is due to the bands of HCN other than the ν_1 bands

4.4 Model photospheres of carbon stars

We used the computational code of model photospheres which has been developed by Tsuji (e.g. 1999) to calculate the model photospheres of carbon stars. In the calculation, hydrostatic equilibrium, including radiation and turbulent pressures, the plane-parallel and homogeneous photospheres in radiative equilibrium are assumed. Local thermodynamic equilibrium (LTE) is assumed in the evaluation of molecular abundance and opacities. The sources of continuous absorption are bound-free and free-free of H^-, free-free of H_2^- and He^-, bound-free and free-free of H I, Si I, Mg I and Ca I, Rayleigh scattering by H I, H_2, and He, and electron scattering. Molecular line opacities are evaluated by the band model method discussed above for CO, CN, C_2, HCN and C_2H_2. We note that the opacities of ^{13}CO, ^{13}CN, ^{12}C^{13}C and $^{13}C_2$ are considered assuming $^{12}C/^{13}C$=50.

We fixed the surface gravity ($\log g = 0.0$) and the micro-turbulent velocity ($\xi_{\rm micro} = 3\,{\rm km\,s^{-1}}$), and calculated model photospheres for $T_{\rm eff}$ = 3200K, 3000K and 2800K, and for C/O = 1.10, 1.03 and 1.01. These values are typical in carbon stars discussed in Chapter 5.

The pressure-temperature structures of our model photospheres are shown in Figure 4.8 for C/O=1.10 and three effective temperatures. The photosphere with $T_{\rm eff}$=2800K is considerably cooler than those of other models. This is because the cooling by polyatomic molecules which have strong bands in the infrared region dominate in the surface layers of the photosphere for $T_{\rm eff}$=2800K.

We also show the model photospheres for $T_{\rm eff}$=3000K and three C/O ratios in Figure 4.9. We can see that the photosphere with a lower C/O ratio is cooler than that with a higher C/O ratio. This is due to the weaker backwarming effect in the optical region by the decrease of CN and C_2 molecules in stars with lower C/O ratios. Hence the temperature structure of photosphere is dependent not only on the effective temperature but also on the C/O ratio. We examine the effect of C/O ratio on molecular features in the infrared spectra in the next chapter.

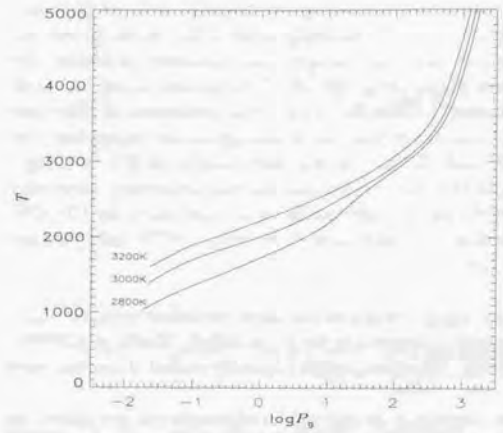

Figure 4.8: Model photospheres of carbon stars for C/O=1.10 and $T_{\rm eff}$ =3200K, 3000K and 2800K.

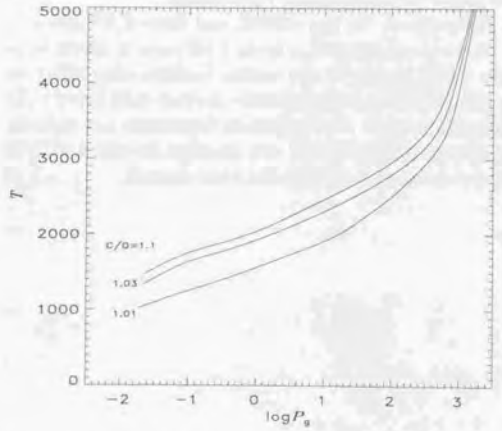

Figure 4.9: Model photospheres of carbon stars for $T_{\rm eff}$ =3000K and C/O=1.10, 1.03 and 1.01

References

Gustafsson B., Bell R. A., Eriksson K., Nortlund Å, 1975, A&A 42, 407

Höfner S., Dorfi E. A., 1997, A&A 319, 648

Peytremann E., 1974, A&A 33, 203

Tsuji T., 1971, PASJ 23, 553

Tsuji T., 1994, LNP 428, *Molecules in the Stellar Environment*, ed. U. G. Jørgensen, 79

Tsuji T., 1999, in proceedings of the IAU Symp. 177, *The carbon star phenomenon*, ed. R. F. Wing, in press

Chapter 5

Molecular features in carbon stars

abstract

We carried out observations of bright optical carbon stars with the ISO SWS, and detected the absorption features of CO, CS, CH, SiS and HCN in N-type and SC-type stars.

We found several characteristics of molecular absorption features corresponding to the spectral types. The CH fundamental bands in 3-4 μm in N-type stars are stronger than those in SC-type stars. On the other hand, the first overtone bands of SiS at 6.6 μm were detected in WZ Cas (SC-type), while none of them were detected in N-type stars. These results can be explained well by the lower C/O ratio in SC-type stars than in N-type stars. The absorption features of HCN (ν_1, $\nu_2 + \nu_3$ and $\nu_1 - \nu_2$) are stronger in SC-type stars than in N-type stars. This fact can be explained by the cooler atmospheres of our SC-type stars due to the lower C/O ratio as well as due to the lower effective temperature, compared with the N-type stars in our sample. The dependence of these infrared molecular features on the C/O ratio is well reproduced by the synthetic spectra based on our model photospheres.

However, the CS fundamental and first overtone bands and the band heads of the CO fundamental bands are weaker in the observed spectra than in those predicted by our model photospheres. In the even longer wavelength region, the distinct emission features of HCN ν_2 bands (14 μm) were detected in TX Psc. These results suggest a contribution to the infrared spectra by the emission of CO, CS and HCN in the outer atmosphere.

5.1 Introduction

As discussed in Chapter 1, one of the important characteristics in the AGB phase is the variation of the chemical composition in the stellar surface. Especially, the increase of carbon abundance may form carbon stars whose spectra are quite different from those of oxygen-rich stars. The structure of photopheres may also be influenced by the chemical composition.

The infrared spectra of oxygen-rich giants obtained with the ISO SWS have already been analyzed by Tsuji et al. (1997) in which the existence of warm molecule forming region in the outer atmospheres was revealed for M giants and Miras. In this chapter, we analyze the SWS spectra of carbon stars, and investigate the absorption and/or emission of molecules in the photospheres and in the outer atmospheres.

Carbon stars are clearly distinguished from cool oxygen-rich stars by their optical spectra; carbon stars show strong C_2 and CN absorption bands, while cool oxygen-rich stars show strong TiO absorption bands. This is because most oxygen is locked up in CO, which is the most tightly bounded molecule in carbon-rich stars while most carbon is locked up in CO in oxygen-rich stars. Most of cool carbon stars are called N-type, while cool oxygen-rich stars are called M-type. Besides the oxygen-rich stars and carbon stars, there are also the less common S-type stars which do not show strong TiO bands nor strong C_2 bands, but show ZrO bands. This means that the C/O ratios of S-type stars are close to unity, and most carbon and oxygen are locked up in CO. S-type stars are further classified by the existence of weak TiO bands or weak C_2 (and CN) bands. Stars showing weak C_2 and CN bands are called SC-type (or CS-type) stars which are in between S-type stars and carbon stars. Then there are two types of cool carbon-rich stars corresponding to the strength of C_2 absorption bands; N-type and SC-type. Since the strength of C_2 bands is strongly dependent on the abundance of carbon which is not locked up in CO, the difference of the spectra between N-type stars and SC-type stars can be attributed to the C/O ratios. The typical C/O ratio of N-type stars is about 1.1, while that of SC-type stars is about 1.01 (Lambert et al. 1986). Though the difference of the C/O ratio seems small, the abundance of carbon which is not locked up in CO (this can be represented by (C−O)/O) is significantly different between N-type stars and SC-type stars.

The pressure-temperature structure of the photosphere is also dependent on the C/O ratio. As shown in Section 4.4, the photosphere with the small C/O ratio (i.e. SC-type stars) is cooler than that with the large C/O ratio (N-type stars) even for the same effective temperature.

In this chapter, we investigate molecular features in the infrared spectra of N-type and SC-type stars obtained with the ISO SWS, and discuss the effect of the C/O ratio and the temperature structure of the photosphere. We observed three N-type stars and three SC-type stars whose spectra of the 3-8 μm region and of the

13-15 μm region are shown in Figures 5.1 and 5.2, respectively.

We note that there are some criteria for the carbon star classification other than the strength of C_2 bands. For example, ^{13}C-rich carbon stars ($^{12}C/^{13}C\sim3$) are called J-type, and carbon stars with relatively small depression in violet flux are called R-type. One carbon star can be classified to two types, e.g. one of the stars in our sample, WZ Cas, was classified to J-type as well as to SC-type. However, we do not discuss here these spectral classes other than N-type and SC-type, because we focus the effect of carbon abundance on the infrared spectra.

Since the infrared excess is not large in the stars in our sample, photospheric contribution dominates in the spectra of the wavelength region observed with the ISO SWS. In the 3-8 μm region, many vibration-rotation bands of diatomic and polyatomic molecules were identified and qualitatively interpreted by our model photospheres. We discuss the identification of molecular features and their characteristics in Section 5.3. On the other hand, some absorption or emission features of molecules originating in outer atmospheres are also expected in infrared spectra of mass losing stars. In the case of oxygen-rich stars, the strong absorption of H_2O and CO_2, which cannot be explained by the photospheric absorption alone, was found by Tsuji et al. (1997), and the CO_2 emission was also discovered by Justtanont et al. (1998). We discuss the contribution to the infrared spectra by molecular emission in the outer atmospheres of carbon stars in Section 5.4.

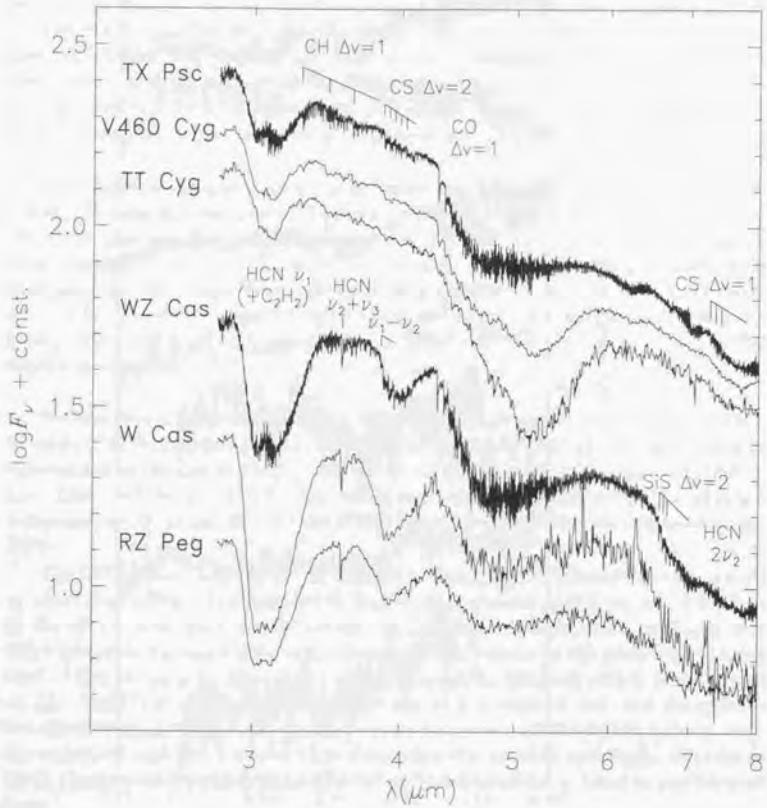

Figure 5.1: The observed spectra of six carbon stars. The upper three are the spectra of N-type stars and the lower three are those of SC-type stars

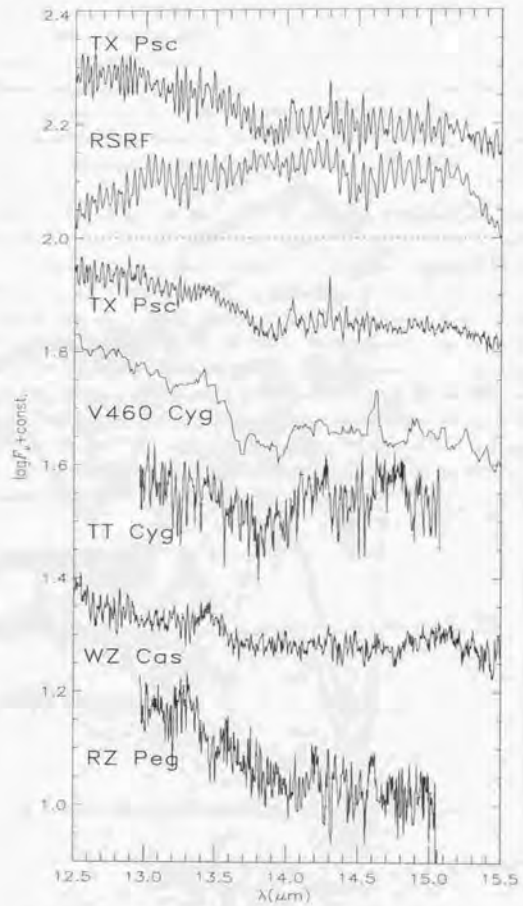

Figure 5.2: The top is the spectrum of TX Psc which is reduced by the normal procedure of the SWS 1A. The spectrum seems affected by fringes when we compare it with the RSRF (the second one). The third one is the spectrum of TX Psc processed by the defringing procedure as described in Chapter 2. The spectra of the other four stars are also shown

5.2 Stellar parameters

In this chapter, we compare several molecular features predicted based on our model photospheres with the observed ones. To specify the model photospheres to be applied in the analysis, the effective temperature ($T_{\rm eff}$), the chemical composition, the surface gravity and the microturbulent velocity should be determined for each object. We discuss the chemical composition, especially the C/O ratio, the effective temperature and the surface gravity of the stars in our sample in this section. The microturbulent velocity is assumed to be $3\,{\rm km\,s^{-1}}$ which is the typical value of red giants in the calculation of model photospheres and of synthetic spectra.

The chemical composition of carbon stars has been derived by Lambert et al. (1986), Ohnaka & Tsuji (1996), Ohnaka (1997), and others. In Table 5.1, we give the C/O ratio and the carbon isotope ratio (^{12}C/^{13}C ratio) derived in the above three papers. The C/O ratio of WZ Cas is very low (C/O=1.01) as expected for SC-type stars. Although there is disagreement between the authors, the C/O ratios derived for TX Psc and V460 Cyg (N-type) are higher than that for WZ Cas (SC-type). We adopt C/O=1.1 and 1.01 for TX Psc and WZ Cas, respectively, in the following discussion.

We also give the effective temperatures determined by Ohnaka & Tsuji (1996), Richichi et al. (1995) and Dyck et al. (1996) in Table 5.2. The effective temperatures determined by Ohnaka & Tsuji (1996) are based on the infrared flux method (IRFM, e.g. Blackwell et al. 1980). We re-examine the determination of the effective temperatures of carbon stars by the IRFM below, using the spectra obtained by the SWS.

The IRFM uses the ratio of the bolometric flux ($f_{\rm bol}$) to infrared flux ($f_{\rm IR}$) such as the L-band flux. The bolometric flux is proportional to $T_{\rm eff}^4$ by the definition of the effective temperature, while the infrared flux is proportional to $T_{\rm eff}$ in the Rayleigh-Jeans regime if there is no strong spectral feature in the photometric band used. Then the $f_{\rm bol}/f_{\rm IR}$ ratio is a good indicator of $T_{\rm eff}$, because that is proportional to $T_{\rm eff}^3$. Tsuji (1981) adopted the L-band flux as the infrared flux, and determined the effective temperature scale of N-type stars by the use of model photospheres with the empirical calibration of the 3 μm absorption due to HCN and C_2H_2. Ohnaka & Tsuji (1996) adopted the L'-band (3.5-4.1 μm) instead of the L-band as the infrared band.

The IRFM is applicable to the case that there is no strong feature in the infrared band adopted. A glance at Figure 5.1 reveals that the adoption of the L'-band by Ohnaka & Tsuji (1996) is justified for the N-type stars. However, as can be seen in the figure, there is a strong absorption feature at 3.9 μm in the spectra of SC-type stars and the actual L'-band flux is smaller than that predicted by the model photosphere which does not take it into account. Therefore the IRFM based on the L'-band flux without the correction for the absorption band at 3.9 μm overestimates

the effective temperatures of these SC-type stars. A quantitative measurement of the absorption is not easy, because of the uncertainty of the continuum level. However, we estimate the absorption of the 3.9μm feature to be about 15% of the L'-band flux in the three SC-type stars based on the SWS spectra. Then the effective temperatures of the SC-type stars would be lower by about 150-200K than those derived by Ohnaka & Tsuji (1996), as given in the third column of Table 5.2.

For some of the carbon stars in our sample, the effective temperatures were determined based on the stellar angular diameters measured by use of the lunar occultation events (Richichi et al. 1995) and/or by the interferometers (Dyck et al. 1996). Their results are also given in Table 5.2. Though there is a disagreement between the result based on the lunar occultation and the interferometric one, this may be due to the deviation from circular symmetry of the stellar disk as discussed by Richichi et al. (1995) in which the effect of this asymmetry was taken into consideration. We adopt $T_{\rm eff} = 3100\,{\rm K}$ and 3000 K for TX Psc and WZ Cas, respectively, in the following discussion.

The surface gravity can be derived by the relation

$$\log g = \log g_{\odot} - 2\log(R/R_{\odot}) + \log(M/M_{\odot}),$$

where g, R and M mean the surface gravity, the radius and the mass of the star, respectively. The radius of TX Psc is about $200R_{\odot}$ which is derived from the angular diameter about 9 mas (e.g. Richichi et al. 1995) and the distance of 230 pc (Hipparcos catalogue (ESA 1997)). Though the mass of TX Psc is unknown, the masses of the Galactic carbon stars are estimated to be $1M_{\odot} < M < 2M_{\odot}$ based on the kinematic properties (e.g. Dean 1976). Therefore we estimated the surface gravity of TX Psc to be $\log g \simeq 0.0$. Since the observed data for the other stars are more uncertain, we assume $\log g = 0.0$ for these stars in the following analysis.

Table 5.1: Carbon abundance and carbon isotope ratio of the carbon stars in our sample

star	C/O		^{12}C/^{13}C	
	O	L	O	L
TX Psc	1.16	1.027	22	43
V460 Cyg	-	1.062	21	61
TT Cyg	-	-	14	-
WZ Cas	-	1.010	4	4.5
W Cas	-	-	25	-
RZ Peg	-	-	18	-

Table 5.2: Effective temperatures of carbon stars of our sample

	IRFM[1]	corrected[3]	LO[4]	Interferometer[5]
TX Psc	3080	-	3000-3150	2921±60
V460 Cyg	3230	-	-	3200±157
TT Cyg	3050[2]	-	-	-
WZ Cas	3160	2980	-	3140±193
W Cas	3180[2]	3000	-	-
RZ Peg	2800[2]	2650	-	-

[1] The effective temperature based on the IRFM (Ohnaka & Tsuji 1996)
[2] The effective temperature determined by $(J - L')_0$ which was calibrated against the effective temperature scale determined by the IRFM
[3] The effective temperature corrected in this work (see Section 5.2)
[4] The effective temperature based on the angular diameter determined by using the lunar occultation (Richichi et al. 1995)
[5] The effective temperature based on the interferometric angular diameter (Dyck et al. 1996)

5.3 Molecular absorption features in 3-8μm

We have detected rich molecular features in the 3-8 μm region of the stars in our sample. The spectra of the six stars are shown in Figure 5.1 with the identification of several molecular bands. Since this wavelength region has become available for the first time with the ISO SWS, we describe the identification of the molecular absorption of CS, CH, SiS and HCN in some detail in this section. We also discuss the dependence of the molecular absorption on the spectral type.

5.3.1 CH fundamental bands (3-4 μm)

As shown in Figure 5.1, we identified the CH fundamental bands at 3.29 μm (1-0), 3.47 μm (2-1) and 3.64 μm (3-2), not only in the spectrum of TX Psc observed by the high resolution mode, but also in those of TT Cyg and V460 Cyg observed by the low resolution mode. The CH absorption features in the three SC-type stars are quite weak if any.

In Figure 5.3, we show the synthetic spectra based on our model photospheres together with the observed ones of TX Psc and WZ Cas. We found that the majority of the absorption features from 3.3 to 3.8 μm in the spectrum of TX Psc are due to the vibration-rotation transitions of CH. On the other hand, the absorption is quite weak in the synthetic spectrum with C/O=1.01, which is the value expected for SC-type stars. Though the strength of the CH absorption somewhat depends on the effective temperature, the effect of the C/O ratio is dominant. We attributed the stronger CH absorption in the N-type stars than in the SC-type stars to the higher C/O ratio in N-type stars. In other words, the weak CH features in SC-type stars are explained by the small abundance of free carbon atoms which are not locked up in CO (C−O abundance). This is the same characteristic as the weak C_2 and CN absorption in the optical spectra of SC-type stars, which is used as the classification criterion of carbon stars.

5.3.2 CS first overtone bands ($\sim$ 4 μm)

As shown in Figure 5.1, we clearly identified the band heads of the CS first overtone bands at 4 μm in the spectra of TX Psc and WZ Cas which are observed by the high resolution mode. The absorption features at 4 μm appear in the other spectra with the lower resolution as well.

The synthetic spectra of CS at 4 μm are shown in Figure 5.4 with the observed spectra of TX Psc and WZ Cas. The positions of the band heads of CS in the predicted spectra agree with those of the observed spectra. However, some features of the observed spectra cannot be explained well by the synthetic spectra of CS; there are other absorption features in this wavelength region. In Figure 5.4, we show the positions of several strong features of the CH fundamental bands. Most of the absorption features in this wavelength region of TX Psc are attributed to CS

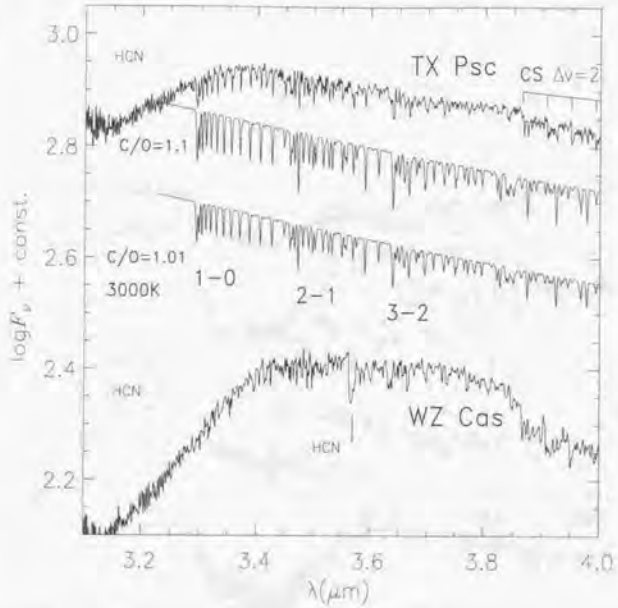

Figure 5.3: The observed spectra of TX Psc and WZ Cas, and the synthetic spectra of the CH fundamental bands based on model photospheres with $T_{\rm eff}$=3000K

and CH. In the observed spectrum of WZ Cas, there is a broad absorption feature between 3.8 and 4.1 μm. We discuss this absorption feature in the next subsection.

The CS absorption in the observed spectra is, as a whole, weaker than that in the predicted ones. We will discuss this problem in Section 5.4.

5.3.3 HCN vibration-rotation spectra (3-4 μm)

In Figure 5.5, we show the synthetic spectra of the HCN bands (ν_1, $\nu_2+\nu_3$ and $\nu_1-\nu_2$) together with the observed ones of TX Psc and WZ Cas. In the calculation of the 3 μm band, the vibration-rotation spectra of $H^{13}CN$ as well as of C_2H_2 are not included. $H^{13}CN$ is probably not so abundant in TX Psc, because the $^{12}C/^{13}C$ ratio is rather high; $^{12}C/^{13}C$=22 was derived by Ohnaka & Tsuji (1996) and a higher value was derived by Lambert et al. (1986). Ridgway et al. (1978) analyzed the high

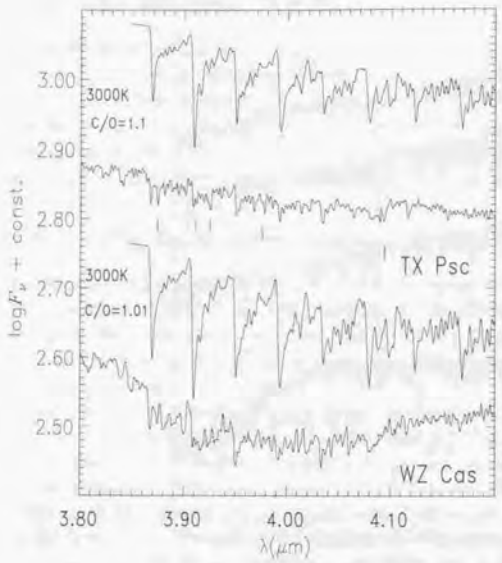

Figure 5.4: The observed spectra of TX Psc and WZ Cas, and the synthetic spectra of the CS first overtone bands based on the model photospheres with $T_{\rm eff}$=3000K. The positions of strong absorption features of the CH fundamental bands are also shown in the observed spectrum of TX Psc

resolution spectrum of the 3μm band of TX Psc, and reported that the absorption lines are almost entirely due to $H^{12}CN$. On the other hand, the absorption of $H^{13}CN$ may be important in WZ Cas, because lower $^{12}C/^{13}C$ ratios were reported (e.g. $^{12}C/^{13}C = 4$ by Ohnaka & Tsuji 1996). We estimated the C_2H_2 absorption by the band model opacity, and found that the C_2H_2 absorption for the parameter set of WZ Cas is stronger than that of TX Psc. This is because the photosphere of WZ Cas is cooler than that of TX Psc. However, we found that the effect of including C_2H_2, in addition to HCN, as opacity sources is at most 10% of the depth of the 3 μm band in the both cases. Hence we concluded that HCN absorption dominates the 3 μm feature in WZ Cas as well as in TX Psc.

We also detected the HCN $\nu_2 + \nu_3$ bands at 3.56 μm in the three SC-type stars. The identification of the $\nu_1 - \nu_2$ bands at 3.9 μm is difficult because of the blend with the CS bands, but these bands seem to be detected for WZ Cas in the wavelength

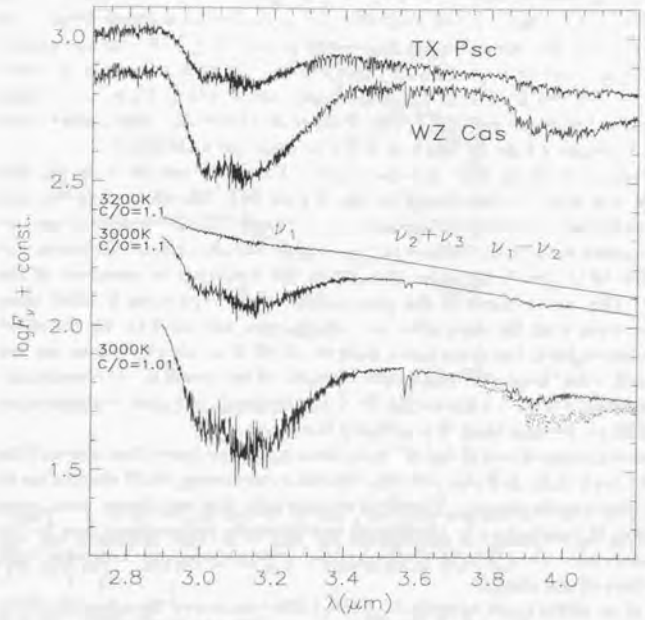

Figure 5.5: The observed spectra of TX Psc and WZ Cas, and the synthetic spectra of the vibration-rotation bands of HCN. The dotted line is the synthetic spectrum of the HCN $\nu_1 - \nu_2$ bands including $v_2 \leq 9$ calculated by the model photosphere with C/O=1.01 and $T_{\rm eff}$=3000K (see text)

region shorter than 3.86 μm at which there is the CS 1-0 band head. Further, we attributed the broad absorption feature at around 3.9 μm in the spectrum of WZ Cas which cannot be explained by the CS first overtone bands (Section 5.3.2.) to the HCN $\nu_1 - \nu_2$ bands. To examine this, we extended the line list of the $\nu_1 - \nu_2$ bands up to $v_2 = 9$ by regarding the l-type splitting as a degeneracy for $v_2 \geq 5$. The synthetic spectrum of these bands including $v_2 \leq 9$ is shown in Figure 5.5 for the case with $T_{\rm eff}$=3000K and C/O=1.01 by the dotted line. Although the line positions of the $\nu_1 - \nu_2$ bands in the synthetic spectrum are not accurate because of the simplification in the calculation of the energy levels for $v_2 \geq 5$, this absorption band can be qualitatively explained by the HCN $\nu_1 - \nu_2$ bands and the CS first overtone bands (Section 5.3.2.). In this wavelength region, the C_2H_2 $\nu_2 + \nu_5$ bands were identified in the spectrum of R Scl by Hron et al. (1998), but the contribution by the C_2H_2 absorption may be small in WZ Cas as in the 3 μm band.

One important result is that the absorption of HCN in our SC-type stars is stronger than that in the N-type stars (see also Figure 5.1). The absorption features of diatomic molecules including carbon (e.g. C_2, CN and CH) are generally weak in SC-type stars, except for CO, because of the small C−O abundance. However, the strength of the HCN bands strongly depends on the temperature structure of the photosphere. The temperature of the photosphere of SC-type stars is lower than that of N-type stars with the same effective temperature (Section 4.4). By the effect of the cool photosphere, the absorption features of HCN in SC-type stars are not weak compared with those of N-type stars, in spite of the small C−O abundance. This can be seen in Figure 5.5 where the HCN absorption in the synthetic spectrum with C/O=1.01 is stronger than that with C/O=1.1.

The effective temperatures of our SC-type stars are rather lower than those of the N-type stars (Table 5.2), and this also contributes to the strong HCN absorption in the SC-type stars in our sample. Therefore we conclude that the strong absorption of HCN in our SC-type stars is attributed to the cooler photosphere due to the lower C/O ratio as well as due to the lower effective temperature, compared with the N-type stars in our sample.

Noguchi et al. (1981) and Noguchi & Akiba (1986) measured the strength of the 3 μm band in carbon stars including 15 SC-type stars based on the near infrared photometry, and showed that the 3 μm bands in SC-type stars are as strong as in other carbon stars, most of which are N-type stars. Since the 3 μm band in SC-type stars would be attributed almost only to HCN, their result suggests that the HCN absorption features in SC-type stars are at least as strong as in N-type stars. This is consistent with our result, and can be explained by the cool photospheres of SC-type stars due to the small C/O ratios as described above.

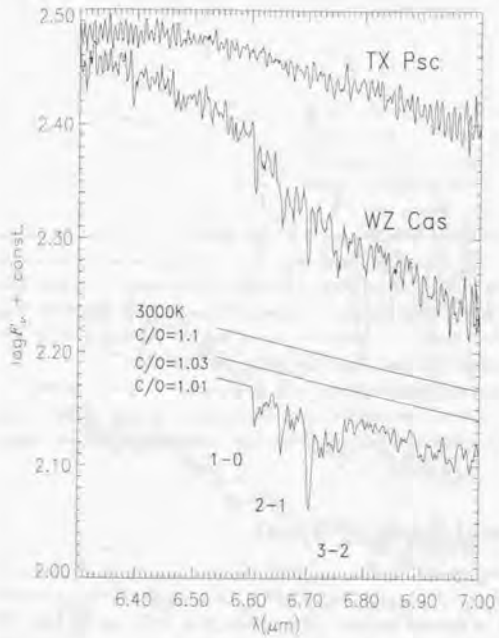

Figure 5.6: The 6-7 μm region of the observed spectra of TX Psc and WZ Cas, and the synthetic spectra of the SiS first overtone bands. The HCN $2\nu_2$ bands contaminate at around 7 μm in the spectrum of WZ Cas

5.3.4 SiS first overtone bands (6.6-7 μm)

In Figure 5.6, we show the 6.3-7 μm region of TX Psc and WZ Cas with the synthetic spectra of the SiS first overtone bands. The band heads of SiS are clearly identified in WZ Cas, while there is no feature of SiS in TX Psc. It should be noted that the HCN $2\nu_2$ bands contaminate at around 7 μm in the spectrum of WZ Cas. The SiS band heads appear in the synthetic spectrum with C/O=1.01 (i.e. the case of SC-type stars), while no or only very weak feature appears in the synthetic spectra with C/O=1.1 and 1.03 (i.e. the cases of N-type stars). Thus the SiS absorption is strongly dependent on the C/O ratio.

In Table 5.3 we give the C−O abundance for stars with C/O=1.1 and 1.03 (N-type) as well as for a star with C/O=1.01 (SC-type), where the oxygen abundance is assumed to be the solar value. We also give the solar abundances of sulfur and

Table 5.3:

	N-type		SC-type
C/O	1.1	1.03	1.01
(C−O)/H	8.3×10^{-5}	2.5×10^{-5}	0.83×10^{-5}
S/H	1.6×10^{-5}	1.6×10^{-5}	1.6×10^{-5}
Si/H	3.5×10^{-5}	3.5×10^{-5}	3.5×10^{-5}

silicon in Table 5.3. Since the C−O abundance is larger than the sulfur abundance in N-type stars, the most sulfur atoms are consumed by CS molecule which is quite stable in the photospheres of cool carbon stars. On the other hand, in the case of SC-type stars, there are free sulfur atoms to form SiS molecules, because the sulfur abundance is larger than the C−O abundance. The large abundance of SiS in SC-type stars can be qualitatively explained by the low C/O ratio.

As discussed in Section 4.4, the photosphere with the lower C/O ratio as in SC-type stars is cooler than that with the higher C/O ratio as in N-type stars. The lower temperature of the photosphere of SC-type stars also contributes to the larger abundance of SiS.

5.3.5 CS fundamental bands (7-8 μm)

The spectra in the 7-8 μm region of TX Psc and WZ Cas are shown in Figure 5.7 with the synthetic spectra of the CS fundamental bands. Although the band heads seem to be detected in the observed spectra, the absorption features of the CS fundamental bands are very weak. One of the reasons for the weakness of the CS features in the observed spectra is that the absorption of the HCN $2\nu_2$ bands masks the CS features in this wavelength region, especially in the spectrum of WZ Cas. However, the weakness of the CS features cannot be explained by this effect alone. We will discuss a possibility of the contribution by the molecular emission in the outer atmosphere in the next section.

5.3.6 C_3 bands (5 μm)

There is a deep absorption band at 5 μm in the spectra of TT Cyg and V460 Cyg. This band would be attributed to the vibration rotation transitions of C_3 (e.g. Jørgensen et al. 1989). This band was not detected in the spectra of SC-type stars as expected by their small C/O ratios. The absence of this band in the spectrum of TX Psc may indicate the smaller carbon abundance than those of TT Cyg and V460 Cyg.

C_3 is one of the candidates of opacity sources for the depression of UV flux in cool carbon stars. A systematic survey of C_3 bands observed with the SWS will give important information for the long standing problem of the violet opacity in carbon

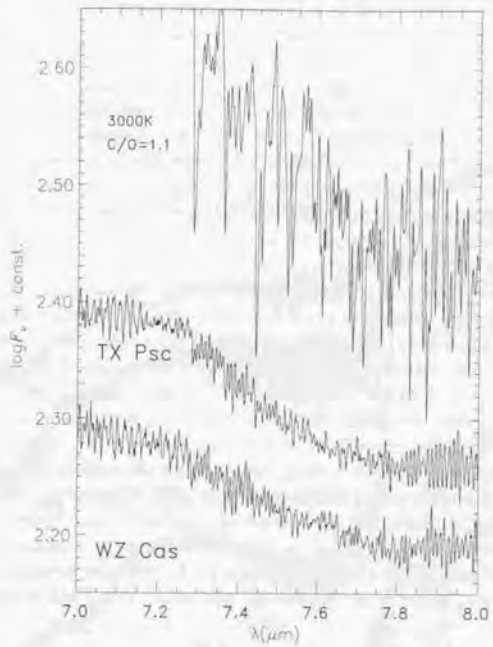

Figure 5.7: The 7-8 μm region of the observed spectra of TX Psc and WZ Cas, and the synthetic spectra of the CS fundamental bands

stars (see Section 6.3).

5.3.7 Spectra of TX Psc and WZ Cas

So far we have discussed each molecular band in Figure 5.3 (CH), Figure 5.4 (CS), Figure 5.5 (HCN), Figure 5.6 (SiS) and Figure 5.7 (CS). We calculated the synthetic spectra including all these molecules and CO (the fundamental and the first overtone bands), and show the results in Figure 5.8 together with the observed spectra of TX Psc and WZ Cas. The resolution of the synthetic spectra is 1500, while the resolution of the SWS06 is between 1000 and 2000 depending on the wavelength.

In addition to the HCN ν_1, $\nu_2+\nu_3$, and $\nu_1-\nu_2$ absorption bands, we found the $2\nu_2$ bands around 7 μm in WZ Cas and our synthetic spectrum can reproduce the feature to a certain extent. The absorption features around 5μm are reproduced by

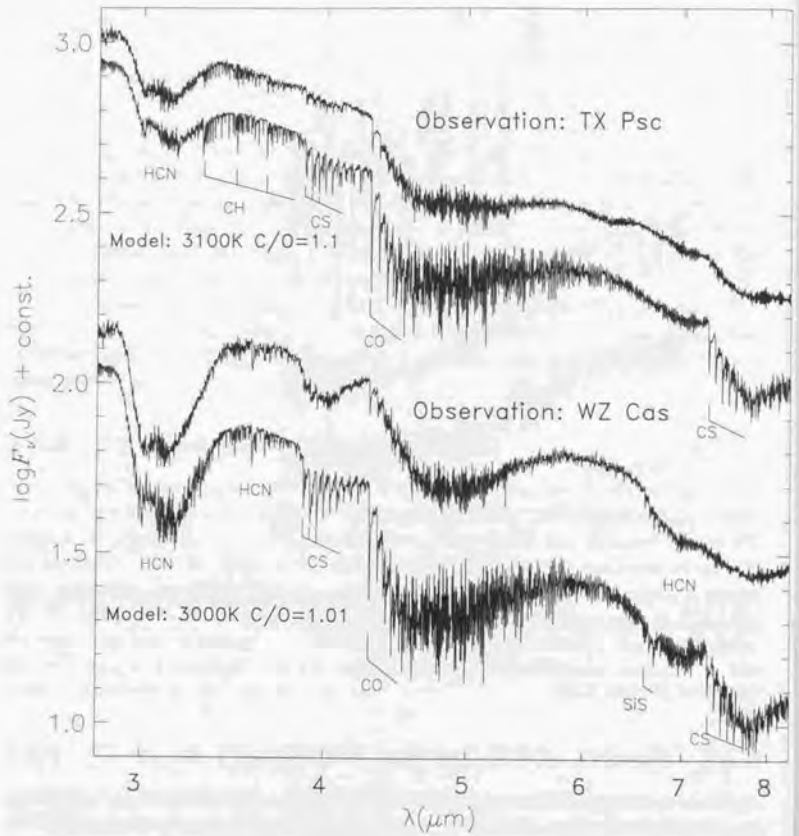

Figure 5.8: The observed spectra of TX Psc and WZ Cas, and the synthetic spectra including HCN, CO, CS, CH and SiS

our synthetic spectrum including the CO fundamental bands. However, the band heads of the CO fundamental bands at 4.3 μm are weaker in the observed spectra of both stars than in the predicted ones. The CS first overtone bands at 4 μm in the observed spectra are also weaker than those in the predicted ones, and the fundamental bands of CS almost disappear.

We conclude that the infrared absorption features of TX Psc and WZ Cas are almost due to the molecules identified in this section, and our model photospheres qualitatively reproduce these absorption features. However, it should be noted that there are many uncertainties in the model photospheres and the stellar parameters for cool carbon stars, and the good agreement between the observed spectra and calculated ones does not necessarily mean that we have well understood the spectra. For example, the uncertainties of the effective temperature and the surface gravity ($\log g$) are at least 100K and 0.5 dex, respectively, and the change of these parameters makes the agreement between the observed spectra and the calculated ones better or worse, because the HCN absorption is quite sensitive to the temperature structure of the photosphere. Jørgensen (1989) reported that his synthetic spectrum with $T_{\rm eff}$=3100K, $\log g = -0.5$ and C/O = 1.023 can reproduce the infrared spectrum of TX Psc. This means the fit between the synthetic spectrum and the observed one is not unique within the uncertainties of the stellar parameters. The sphericity of the photosphere may affect the spectra, but that is not taken into account in the present work. Further, the absorption features of CO and CS, which are stable and abundant in the photospheres of cool carbon stars, are not reproduced well by our synthetic spectra. This means we need more quantitative analysis to understand consistently the molecular features in the infrared spectra.

5.4 Molecular emission in the outer atmosphere

In the observed spectra, there are some features which cannot be reproduced by our model photospheres. In this section, we investigate the CO and CS absorption bands and 14 μm features, and discuss the molecular emission in the outer atmospheres.

5.4.1 CO and CS absorption features

As shown in the previous section, the absorption features of the CS first overtone bands and the band heads of the CO fundamental bands in the observed spectra are weaker than in the spectra predicted by our model photospheres. Furthermore, the absorption features of the CS fundamental bands in the longer wavelength region almost disappear. Since these molecules are quite stable in the photospheres of cool carbon stars, it is difficult to explain these facts by a small change of the temperature structure of the model photosphere or of the stellar parameter.

One important simplification in the calculation of our model photospheres and synthetic spectra is the assumption of plane-parallel geometry. For giant stars, however, we may need to consider the effect of sphericity on the band features.

The sphericity effects in extended photospheres were investigated by Watanabe & Kodaira (1978) for oxygen rich giants and supergiants. They pointed out the two effects of sphericity on absorption spectra. The one is that the surface area of the upper layers of the photosphere increases with the photospheric extension. As a result, strong absorption lines which originate in the uppermost layer are weakened. The other is that the absorption lines of molecules which are more abundant in lower temperature (e.g. H_2O) are strengthened, because the temperature drops due to flux dilution in extended photospheres. They demonstrated that the CO absorption features are not so affected by the sphericity for a star with $T_{\rm eff}$=3200K, $\log g = -0.5$ and $M = 1M_\odot$, which is corresponding to the stellar radius (R_*) of $295R_\odot$ and the photospheric extension of $0.23R_*$. This result was interpreted as the cancelation of the above two effects.

The effects of spherical extension on spectra of carbon stars were studied by Scholz & Tsuji (1984). They compared the effects between carbon stars and M giants, and revealed that the sphericity effects are smaller for carbon stars than for M giants with the same parameters ($T_{\rm eff}$, g or L, and M). This result was attributed to the difference of absorption sources in the surface photospheres between carbon stars and M giants. Jørgensen et al. (1992) also studied the effect of sphericity in carbon stars based on more complete opacities and detailed sampling method, and found even smaller sphericity effects than those reported by Scholz and Tsuji (1984). They showed that the CO absorption lines are insensitive to, or rather strengthened by, the sphericity effects for stars with $T_{\rm eff}$=2800K, $\log g = -0.5$. Ohnaka (1997) also investigated the sphericity effect on absorption lines of CO fundamental bands for carbon stars, and showed that the strong lines are strengthened by the sphericity effect, while weak lines are weakened for a star with $T_{\rm eff}$=2800K, $\log g$=0.0 and $M = 2M_\odot$. However, the effect is unlikely detectable in the SWS spectra due to their limited resolution.

Thus the effects of sphericity depend not only on the stellar parameters but also on the opacity sources in the surface of photospheres. However, the effects are generally smaller for carbon stars than for oxygen-rich giants, and the CO absorption lines are insensitive to the spherical extension. We conclude that the spherical extension of the photosphere is not the main reason of the weakness of CO absorption bands (and probably of CS absorption bands) found in the observed spectra of our carbon stars.

We discuss here a possibility of the contribution by the emission in the outer atmosphere. As mentioned in Chapter 1, AGB stars generally show the mass loss phenomena and have circumstellar envelopes. The matter projected on the stellar disk can absorb the incident photospheric radiation. This causes the excess absorption compared with the absorption features produced in the photosphere. From the matter to the sides of the stellar disk, we can receive photons either emitted thermally or scattered from stellar radiation.

Tsuji (1988) reported the excess absorption of the CO first overtone bands in several M giants, and attributed this to the absorption in the warm molecule-rich region close to the star. Similar excess absorption of the CO first overtone bands was also found by Ohnaka (1997) for TX Psc which is one of the stars in our sample. On the other hand, absorption features may be weakened in the longer wavelength region by the emission in the outer atmosphere, because the contribution by the photospheric radiation is smaller in the longer wavelength region. The result that the absorption of the CO fundamental bands are weaker and those of the first overtone bands are stronger compared to the spectra predicted by the model photosphere is consistent with this expectation. The characteristics of the fundamental and the first overtone bands of CS are also consistent with this prediction. However, it is not easy to explain these features quantitatively. For instance, our observations show that absorption is quite weak in the band heads of the CO fundamental bands. Since the excitation potential of the lines which form band head features is considerably high (e.g. higher than 10000 cm^{-1} for the 1-0 band of CO), quite warm CO gas is required in the envelope.

5.4.2 HCN ν_2 bands (14 μm)

In the even longer wavelength region, some distinct emission features are expected from the hypothesis of the contribution by the emission in the outer atmospheres. As described in Chapter 3, HCN and C_2H_2 have strong vibration-rotation bands in 13-15 μm. In Figure 5.9 we show the 14 μm region of the observed spectrum of TX Psc. In this figure, we also show the low resolution spectrum of TX Psc, the low and high resolution spectra of S Cep (N-type), which were observed in the solicited

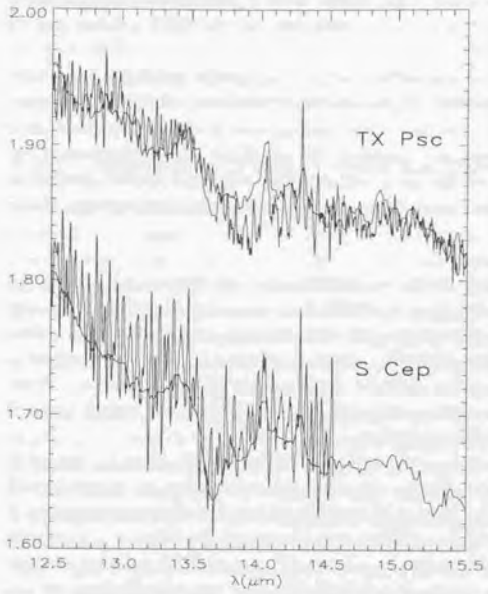

Figure 5.9: The observed spectra of TX Psc and S Cep, and the synthetic spectra of the HCN ν_2 bands and the C_2H_2 ν_5 bands. The low resolution spectra observed with the SWS01 are superimposed on the high resolution ones with the SWS06. The two spectra of S Cep were obtained on the same date, while those of TX Psc were not

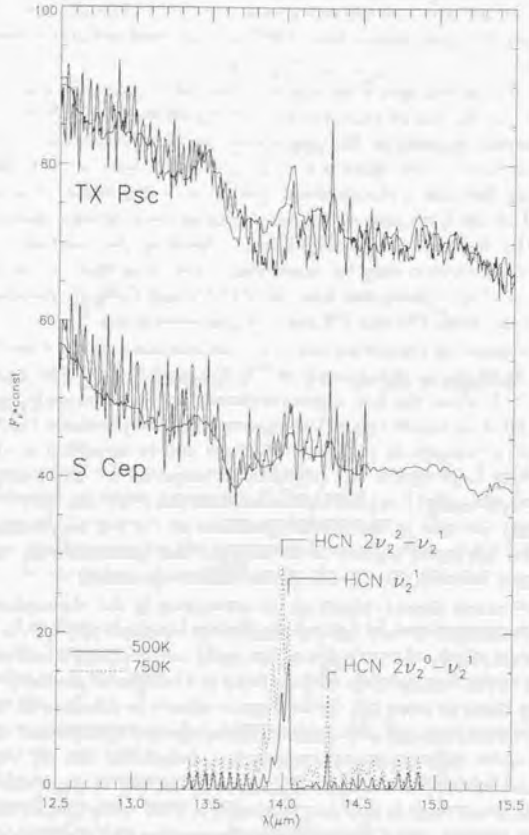

Figure 5.10: The observed spectra of TX Psc and S Cep, and the calculated emission spectra ($\tau B_\nu(T)$) of the HCN ν_2 bands for 500K and 750K

time program ZZAGB2PN (P.I. Dr. F. Kerschbaum) and archived. We note that our higher resolution spectrum of TX Psc was obtained on 6 Mar. 1997, while the lower resolution one was on 12 Dec. 1997. Though the spectral features between these two spectra are somewhat different, this may not be due to the instrumental problem but due to the variation of the intrinsic stellar spectrum. The two spectra of S Cep were obtained on the same date (7 Dec. 1997) and spectral features as well as flux levels agree well.

In Figure 5.9, we also show the synthetic spectra of the HCN ν_2 bands and the C_2H_2 ν_5 bands calculated by the model photosphere with $T_{\rm eff}$=3000K and C/O=1.1. The HCN absorption feature appears at 13.9 μm in the spectrum of TX Psc. The absorption feature at 13.7 μm in the spectrum of S Cep would be due to C_2H_2. However, these absorption features in the observed spectra are much weaker than in the predicted spectra. The line lists used in the calculation of the synthetic spectra are incomplete, especially for higher excitation lines. Therefore the weakness of absorption in the observed spectra may be more significant than that found in Figure 5.9. The weakness of the absorption features of HCN and C_2H_2 in observed spectra should relate to the weak CO and CS features discussed above.

In addition to the weakness of absorption features, emission features are directly detected at 14.04 and 14.30 μm in the spectra of TX Psc and S Cep. We show these spectra in Figure 5.10 where the flux density is shown on the linear scale, and emission spectra of the HCN ν_2 bands calculated assuming the temperatures (500K and 750K). These emission features at 14.04 and 14.30 μm can be identified as the Q branches of the HCN ν_2^1 band and of the $2\nu_2^0$-ν_2^1 band, respectively. The energy levels of HCN and the wavelengths of the transitions between the levels are shown in Figure 5.11. The emission features in the SWS06 spectrum of TX Psc are unlikely due to the fringes or the defringing process if we compare the spectrum with the RSRF (Figure 5.2). These features also appear in the SWS01 spectrum.

Since the molecular features should consist of the absorption in the photosphere (and partly in the outer atmosphere) and the emission in the outer atmosphere, it is not easy to discuss quantitatively the emission in the outer atmosphere. However, the emission features of the Q branch of the $2\nu_2^0$-ν_2^1 band at 14.30 μm is probably as strong as that of the ν_2^1 band at 14.04 μm. If the region where the emission of the $2\nu_2^0$-ν_2^1 band originates is dense enough to be regarded as in thermal equilibrium, the temperature should be quite high because the excitation potential of the $2\nu_2^0$ level is corresponding to about 2000K. However, the Q branch of the $2\nu_2^2$-ν_2^1 band which is expected at 14.00 μm is not seen in the spectrum of TX Psc. This means that the excitation to the $2\nu_2^0$ level is mainly due to radiative pumping by 7 μm photons, because the $2\nu_2^2$ transition is forbidden by the selection rule on the quantum number l while the $2\nu_2^0$ transition is allowed. Then the temperature of the region where the emission features originate is not necessarily so high.

The probability for collisional excitation is estimated by $C \sim N_{\rm H_2}\sigma v$. The cross section, σ, is of the order of 10^{-15}cm^2, and the velocities of the molecules, v, for the temperature considered are about 1 km s^{-1}. The Einstein coefficients of the vibrational transitions $2\nu_2^0$ and $2\nu_2^0$-ν_2^1 are 2.1 s^{-1} and 3.3 s^{-1}, respectively. Therefore the radiative processes dominate, if the density is lower than 10^{10}cm^{-3}. Since the densities of the outer atmosphere and the circumstellar envelope of TX Psc would not be so high except for the innermost layer (see Section 6.3), the above interpretation on the excitation of the HCN molecule is quite reasonable.

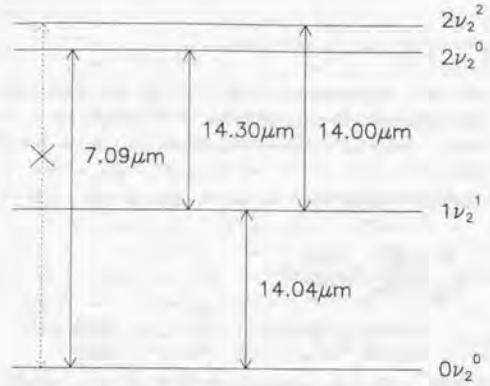

Figure 5.11: The energy levels of HCN and the wavelengths of transitions in the ν_2 bands

The flux of the Q branch of the $2\nu_2^0$-ν_2^1 band measured for TX Psc is about 2×10^{-12} erg s^{-1}cm^{-2}. The uncertainty would be as large as factor 2, because the emission of the $2\nu_2^0$-ν_2^1 band blends with photospheric absorption. We now estimate the flux of $2\nu_2^0$-ν_2^1 band expected from the circumstellar envelope (including the outer atmosphere in this discussion) of TX Psc, and compare it with the observed one. In the calculation, we assume the pure radiative processes, i.e. the HCN molecule in the ground state is pumped to the $2\nu_2^0$ level by 7 μm photon from the photosphere, and radiatively decays to the ν_2^1 and the ground levels. We also assume an optically thin circumstellar envelope with the constant mass loss rate ($\dot{M}$), the constant expansion velocity ($v_{\rm exp}$) and the constant abundance of HCN ($\epsilon_{\rm HCN}$). The fraction of the $2\nu_2^0$-ν_2^1 transition is $\alpha = A_{2\nu_2^0-\nu_2^1}/(A_{2\nu_2^0-\nu_2^1} + A_{2\nu_2^0}) \sim 0.6$.

The number of HCN molecule in the spherical shell with radius r and thickness dr is

$$n_{\rm HCN} = 4\pi r^2 dr \cdot n\epsilon_{\rm HCN},$$

where n is the density which is given by $n = \dot{M}/(4\pi r^2 v_{\rm exp}\mu m_{\rm H})$. The flux of $2\nu_2^0$-ν_2^1 band from this shell is

$$dF_{2\nu_2^0-\nu_2^1} = \alpha \frac{1}{4\pi D^2} n_{\rm HCN} \frac{D^2}{r^2} f_{\lambda_0} \sigma_{\lambda_0} \delta\lambda,$$

where D is the distance to the star, λ_0 is the wavelength of the $2\nu_2^0$ transition (7.09 μm), and f_{λ_0} is the 7 μm flux density observed (200Jy=1.2×10^{-4}erg s^{-1}cm^{-2}cm^{-1}). The cross section, σ_{λ_0}, is given by $(\pi e^2/m_e c^2)(\lambda_0^2 f_{2\nu_2^0}/\delta\lambda)$, where $f_{2\nu_2^0}$ is the band oscillator strength of the $2\nu_2^0$ transition (1.6×10^{-6}), and $\delta\lambda$ is the width of lines in the $2\nu_2^0$ band. The stimulated emission is ignored here. The integrated flux expected to be observed is

$$F_{2\nu_2^0-\nu_2^1} = \int_{r_{\rm in}}^{\infty} dF_{2\nu_2^0-\nu_2^1} = \alpha \frac{e^2\lambda_0^2 f_{2\nu_2^0}}{4m_e c^2 \mu m_{\rm H}} f_{\lambda_0} \frac{\dot{M}\epsilon_{\rm HCN}}{v_{\rm exp} r_{\rm in}}$$

$$\sim 6.6\times10^{-12}\,{\rm erg\,s^{-1}cm^{-2}} \left(\frac{\epsilon_{\rm HCN}}{6\times10^{-6}}\right)\left(\frac{r_{\rm in}}{R_*}\right)^{-1}\left(\frac{\dot{M}}{10^{-7}M_\odot{\rm yr}^{-1}}\right)\left(\frac{v_{\rm exp}}{10{\rm km\,s^{-1}}}\right)^{-1},$$

where R_* is the stellar radius ($200R_\odot$). The abundance of HCN in the circumstellar envelope has not yet been measured for TX Psc, though the upper limit, 2.2×10^{-5}, was determined by Olofsson et al. (1993b) using the emission line in the radio range. We here adopt $\epsilon_{\rm HCN} = 6\times10^{-6}$ which was derived from the calculation of photodissociation and molecular abundance in the circumstellar envelope of TX Psc by Wirsich (1997). The expansion velocity of the circumstellar envelope is 10.5 km s^{-1} which was determined by Olofsson et al. (1993a) using the CO emission in the radio range. However, the velocity in the inner envelope would be smaller than that in the extended envelope (Section 1.2, see also Section 6.3), and the density of HCN in the inner envelope would be higher than that estimated in the above simple calculation. Further, in the innermost layer, the effect of collisional transition should be considered because of the high density. Though there are such uncertainties in the above estimation of the flux of the HCN $2\nu_2^0$-ν_2^1 band, the order of the flux expected is 10^{-12} erg s^{-1}cm^{-2}, which is consistent with the observed one. This means that the emission of the HCN would be reasonably explained by the radiation processes in the circumstellar envelope, and the HCN features can be one of the constraints on the detailed modeling of the outer atmospheres and the circumstellar envelopes of carbon stars.

The detection of emission of the Q branch of the $2\nu_2^0$-ν_2^1 band at 14.30 μm was also reported by Cernicharo (1998) for IRC+10216 which is the well known infrared carbon star with heavy mass loss. The feature was attributed to the emission in cool envelope where HCN molecules in the ground state are pumped by 7 μm photons originating in the inner part of the envelope (Cernicharo 1998). The structures of the outer atmosphere and the circumstellar envelope (e.g. the thickness of the dust shells) are quite different between TX Psc and IRC+10216, but the excitation and emission mechanism would be common for the 14 μm bands of HCN in these stars.

5.4.3 Molecular emission in the outer atmosphere

Based on the above analysis of CO, CS and HCN features in carbon stars, we conclude that molecular emission in the outer atmospheres contributes to their infrared spectra. From the absorption features of CO, CS and HCN (14 μm) which are weaker than those predicted by model photospheres, the existence of the warm and dense region is suggested. In addition, the emission feature of the HCN ν_2 bands suggests a rather cool component in the outer atmosphere or in the circumstellar envelope.

Our observations of oxygen-rich giants with the ISO SWS revealed that the absorption features of CO and SiO in M giants are weaker, while the absorption features of H_2O and CO_2 are stronger, than those predicted by our model photospheres (Tsuji et al. 1997). To explain this fact, we proposed the warm molecular envelope around the photosphere. We note that the sphericity effect was considered in the calculation of the model photospheres and the synthetic spectra for M giants in that work. Further, the 15 μm CO_2 emission (ν_2 bands) in oxygen-rich giants was reported by Justtanont et al. (1998) and Ryde et al. (1999), and that was also detected in our M giants. Thus the characteristics of absorption and emission of molecules in carbon stars are similar to those in oxygen-rich giants, although the species detected are of course different.

The emission bands of CO_2 in the 13-16 μm region of oxygen-rich stars have not yet been consistently explained. The ν_2^1 band at 15.0 μm which is expected to be strongest is rather weaker than the ν_1^0-ν_2^1 band at 13.9 μm and the $2\nu_2^0$-ν_2^1 band at 16.2 μm. This nature may be similar to that of HCN 14 μm emission features discussed above. As a possible explanation of the CO_2 emission features, the two-layer model of the circumstellar envelope was proposed by Ryde et al. (1999). One is a warm and high density layer close to the star where the 13.9 and 16.2μm bands originate but the 15 μm band is weak due to its optically thickness. The other is a cool and optically thin layer expanding far out in the wind where the 15 μm band originates. Similar discussion may be possible for the HCN emission features in the 14 μm region of carbon stars. But the situation is more complicated because the photospheric contribution is large in the HCN features contrary to the CO_2 features.

Aringer et al. (1999) showed that the absorption of the SiO first overtone bands (4 μm) is quite weak in oxygen-rich cool stars, especially in Mira variables. They attributed this fact to the effect of atmospheric dynamics based on the analysis of the SiO bands using the dynamical models (e.g. Höfner and Dorfi 1997) in which the stellar pulsation is considered. The main reason why weaker absorption is predicted by dynamical models than by hydrostatic ones is their larger extension producing emission components. The concept of the warm molecule-rich region proposed by Tsuji et al. (1997) as well as suggested by this work may be similar to that of surface layers of dynamical model atmospheres, and pulsation is one of the explanations for the weakness of absorption features and/or emission features observed in cool giants.

However, the problem is that the most stars in our sample are not Mira variables but semi-regular or irregular variables in which the effect of pulsation would be much weaker than in Miras. For example, the visual variability is as small as 1 magnitude in TX Psc and WZ Cas, while most Miras show that of 3-10 magnitude. The variation of the radial velocities of absorption lines of molecules (mainly CN) as well as those of atomic lines (K I, Na I and Li I) is much smaller in TX Psc than in carbon-rich Miras (Barnbaum 1994). Furthermore, H_2O absorption features were detected even in the spectra of early M giants (β Peg and α Cet) for which no H_2O absorption is predicted by model photospheres (Tsuji et al. 1997, 1999). Though atmospheric dynamics by stellar pulsation may be one of the physical mechanisms causing the weakness of absorption features (and perhaps emission features) found in infrared spectra of cool giants, our results suggest the existence of some other components in the outer atmospheres in which molecular absorption and/or emission features originate.

5.5 Concluding remarks

We obtained the infrared spectra of carbon stars free from contaminations of the Earth's atmosphere for the first time thanks to the ISO SWS. We identified the absorption and emission features of several molecules in the infrared spectra of N-type and SC-type stars. The main conclusions are as follows;

(1) The CH fundamental bands in 3-4 μm are stronger in N-type stars than in SC-type stars. The first overtone bands of SiS at 6.6 μm were detected in the SC-type star WZ Cas, while no feature of SiS is seen in N-type stars. These results can be explained well by the lower C/O ratio in SC-type stars than in N-type stars.

(2) We identified the combination bands of HCN ($\nu_2 + \nu_3$ and $\nu_1 - \nu_2$) in SC-type stars and the strong absorption of the CH-stretching bands of HCN (ν_1) in both N-type and SC-type stars. The absorption features of HCN in the spectra of the SC-type stars in our sample are stronger than those in the N-type stars. This fact could be attributed to the cooler atmosphere of the SC-type stars due to the lower C/O ratio as well as due to the lower effective temperature, compared with the N-type stars in our sample.

(3) We re-determined the effective temperatures of SC-type stars by the infrared flux method based on the L'-band flux, considering the strong absorption feature at 3.9 μm found in the SWS spectra of SC-type stars. The effective temperatures of SC-type stars turned out to be lower by 150-200K than those derived by the previous work which did not take it into account.

(4) The CS fundamental and first overtone bands as well as the band heads of the CO fundamental bands are weaker in the observed spectra than in the predicted ones based on our model photospheres. In the spectrum of TX Psc, we detected not only the quite weak absorption features of HCN ν_2 bands but also the emission features of ν_2^1 and $2\nu_2^0$-ν_2^1 bands. These results suggest the contribution to the infrared spectra by the emission of CO, CS and HCN in the outer atmosphere.

By the present work, most of the absorption and/or emission features in the spectra of carbon stars in our sample are identified. The dependence of molecular features on the spectral type is explained well for N-type and SC-type stars. The importance of the C/O ratio in the structures of photospheres as well as in the molecular formation is shown by the analyses of the molecular features.

For detailed and quantitative discussion on the molecular spectra of carbon stars, we need more realistic model photospheres and more precise stellar parameters, and may need to take the time variation of the spectra into account. The accurate knowledge on molecules is also indispensable. In addition to the improvement of model photospheres, the detailed models of the outer photosphere are required to study the implications of the molecular features.

References

Aringer B., Höfner S., Wiedemann G., 1999, A&A, in press
Barnbaum C., 1994, ApJS, 90, 317
Blackwell D. E., Petford A. D.,Shallis M. J., 1980, A&A 82, 249
Cernicharo J., 1998, Ap&SS 255, 303
Dean C. A., 1976, AJ 81, 364
Dyck H. M., van Belle G. T., Benson J. A., 1996, AJ 112, 294
ESA, 1997, The Hipparcos and Tycho Catalogues, ESA SP-1200
Höfner S., Dorfi E. A., 1997, A&A 319, 648
Hron J., Loidl R., Höfner S. et al., 1998, A&A, 335, L69
Jørgensen U. G., 1989, ApJ 344, 901
Jørgensen U. G., Almlöf J., Siegbahn Per E. M., 1989, ApJ 343, 554
Jørgensen U. G., Johnson H. R., Nordlund Å, 1992, A&A 261, 263
Justtanont K., Feuchtgruber H., de Jong T. et al, 1998, A&A 330, L17
Lambert D. L., Gustafsson B., Eriksson K., Hinkle K. H., 1986, ApJS 62, 373
Noguchi K., Akiba M., 1986, PASJ 38, 811
Noguchi K., Kawara K., Kobayashi Y. et al., 1981, PASJ 33, 373
Ohnaka K., 1997, Ph. D. Thesis, The University of Tokyo
Ohnaka K., Tsuji T., 1996, A&A 310, 933
Olofsson H., Eriksson K., Gustafsson B., Carlström U., 1993a, ApJS 87, 267
Olofsson H., Eriksson K., Gustafsson B., Carlström U., 1993b, ApJS 87, 305
Richichi A., Chandrasekhar T., Lisi F., et al. 1995, A&A 301, 439
Ridgway S. T., Carbon D. F., Hall D. N. B., 1978, ApJ 225, 138
Ryde N., Eriksson K., Gustafsson B., 1999, A&A 341, 579
Scholz M., Tsuji T., 1984, A&A 130, 11
Tsuji T., 1981, JA&A 2, 95
Tsuji T., 1988, A&A 197, 185
Tsuji T., Aoki W., Ohnaka K., 1999, in proceedings of *The Universe as seen by ISO*, in press
Tsuji T., Ohnaka K., Aoki W., Yamamura I., 1997, A&A 320, L1
Watanabe T., Kodaira K., 1978, PASJ 30, 21
Wirsich J., 1997, Ap&SS 250, 271

Chapter 6

Fine-structure line emission of metals in AGB stars

abstract

We detected five forbidden lines of iron, silicon and sulfur in the SWS spectra of red giants. [Fe I] 24 μm emission was detected in three carbon stars, TX Psc, WZ Cas and W Ori, and [S I] 25.2 μm emission was also detected in TX Psc. On the other hand, [Fe II] 26 μm emission was detected in the spectrum of two oxygen-rich stars, 30g Her and α Her, and [Si II] 34.8 μm and [Fe II] 35.3 μm emission lines were detected in 30g Her.

We estimate that the temperature of the line forming region is several hundred Kelvin or higher and the mass of the region is several $\times 10^{-6} M_{\odot}$. This implies that there is a rather dense and warm region close to the star in addition to the well known cool expanding envelope in these stars.

One remarkable result is that the emission lines of neutral metals were detected in carbon stars while the lines of ions were in oxygen-rich giants. This result indicates that the ionization states of metals in the outer atmospheres of carbon stars are quite different from those of oxygen-rich giants. This suggests that the effect of chromospheric ultraviolet radiation is much weaker in carbon stars than in oxygen-rich giants in which emission lines were detected. By compiling the results derived by the analyses of fine-structure lines and of molecular features detected in our ISO SWS observations, the chromospheric activity, chemistry in the outer atmosphere and the relation of infrared spectral features to stellar evolution are discussed.

6.1 Introduction

As shown in Chapter 1, it is very important to clarify the structure and the chemical processes in the outer atmospheres of cool evolved stars for understanding of the origin of stellar mass loss and the formation of circumstellar envelopes. In the previous chapter, we described the molecular features detected in carbon stars and discussed the molecules in the outer atmospheres as well as in the photospheres. The molecules in the outer atmospheres of oxygen-rich giants in our sample were also discussed by Tsuji et al. (1997). However, most of these discussions are based on the absorption features of molecules, so that we cannot avoid the difficulty in distinguishing the component of the outer atmosphere from the photospheric one. On the other hand, the emission features in the infrared region can be more direct evidence of the existence of outer atmospheres. Especially, the forbidden lines of metals whose excitation potentials are about several hundred cm^{-1} are expected to be useful, because these lines can well trace the region with temperatures of about several hundred Kelvin or higher. In this chapter, we discuss our observations for the wavelength region longer than 20μm where some forbidden lines of metals exist.

The forbidden lines we discuss here are the fine-structure lines in the ground state of metals which have been observed in various objects (e.g. planetary nebulae, H II region). For late-type stars, however, the detection was limited to a few very bright supergiants. Haas & Glassgold (1993) detected the [O I] 63 μm and [Si II] 35 μm emission lines for α Ori for the first time using the Kuiper Airborne Observatory. Their result agrees well with the prediction based on the model of the thermal structure for α Ori's envelope by Rogers & Glassgold (1991), and they concluded that these lines originate in the dense and warm gas in the inner envelope of this star and discussed the effect of chromospheric radiation in the dust-poor envelope of α Ori. Though these lines were also detected in some other supergiants (Haas et al. 1995), the detection was limited to very bright objects.

The observation of these lines in various red giants became realistic thanks to the ISO SWS. We observed 10 red giants including M giants and carbon stars with the high resolution mode, and detected several fine-structure lines in five stars among them. In Section 6.2, we describe the observation and the measurement of the fluxes for the lines detected, and estimate the temperature and the mass of the line emitting region. In Section 6.3, we discuss the location of the line emitting region, the chromospheric activity and the chemistry in the outer atmosphere of cool evolved stars based on the results derived by the analyses of fine-structure lines as well as of molecular features described in Chapter 5 and in Tsuji et al. (1997).

6.2 Observations and results

6.2.1 Detection and measurement of fine-structure lines

We described the sample of our program in Chapter 2. We discuss here the 10 objects (five M giants and five carbon stars) among them which were observed using the SWS06 or SWS01-4 with a resolution about 1000-2000. The observation and data reduction were done as described in Chapter 2.

In Table 6.1, we give the fine-structure lines of FeI, FeII, SI and SiII which are expected in the wavelength region between 10 and 45 μm covered by the SWS. These elements should be quite abundant and have transitions with the excitation potential lower than 2500 cm^{-1} in this wavelength region.

The observed spectra at around 25 μm are shown in Figures 6.1. In this wavelength region, the [Fe I] line (24.0 μm) was detected in 3 stars (TX Psc, WZ Cas and W Ori), the [Fe II] line (26.0 μm) was detected in 3 stars (α Her, 30g Her and TX Psc), and the [S I] line (25.2μm) was detected in TX Psc. Further, in the 35 μm region of 30g Her, the [Fe II] and [Si II] lines were also detected. We confirmed that these emission lines were detected both by the up and down grating scans. Therefore these lines are very unlikely spurious features. On the other hand, no emission line was detected in the other four objects (T Lyr, V CrB, α Cet and ρ Per) in our sample. In the spectrum of SW Vir, some emission features are seen in the 25 μm region (Figure 6.1). However, it is quite difficult to identify the fine-structure line emission, because of the contamination by rich-H_2O emission lines in this wavelength region of SW Vir (Tsuji et al. 1999).

One remarkable result is that the fine-structure lines of neutral atoms, i.e. [Fe I] and [S I], were detected in the carbon stars, but no line of ions was detected except for the weak [Fe II] line in TX Psc. On the other hand, the lines of ions, i.e. [Fe II] and [Si II], were detected in the oxygen-rich stars, but no line of neutral metals was detected. Namely the emission lines of neutral metals were detected in the carbon stars while the lines of ions were detected in the oxygen-rich giants. We discuss the implication of this result in the next section.

Some examples of lines detected in our observation are shown in Figure 6.2, where the dot is the median of the signals of each grid defined by a resolution element, and the error bar indicates $\pm 1\sigma$ (the standard deviation). The solid line indicates the best least-square fit on the assumption of a flat continuum and a Gaussian line profile. In the fitting, the line width is fixed at the instrumental resolution ($R = 1200$), because of the low signal-to-noise ratios in some lines. Therefore the free parameters in the fitting are the continuum level, the line strength and the central wavelength of the line. The flux measured for each fine-structure line is given in Table 6.2.

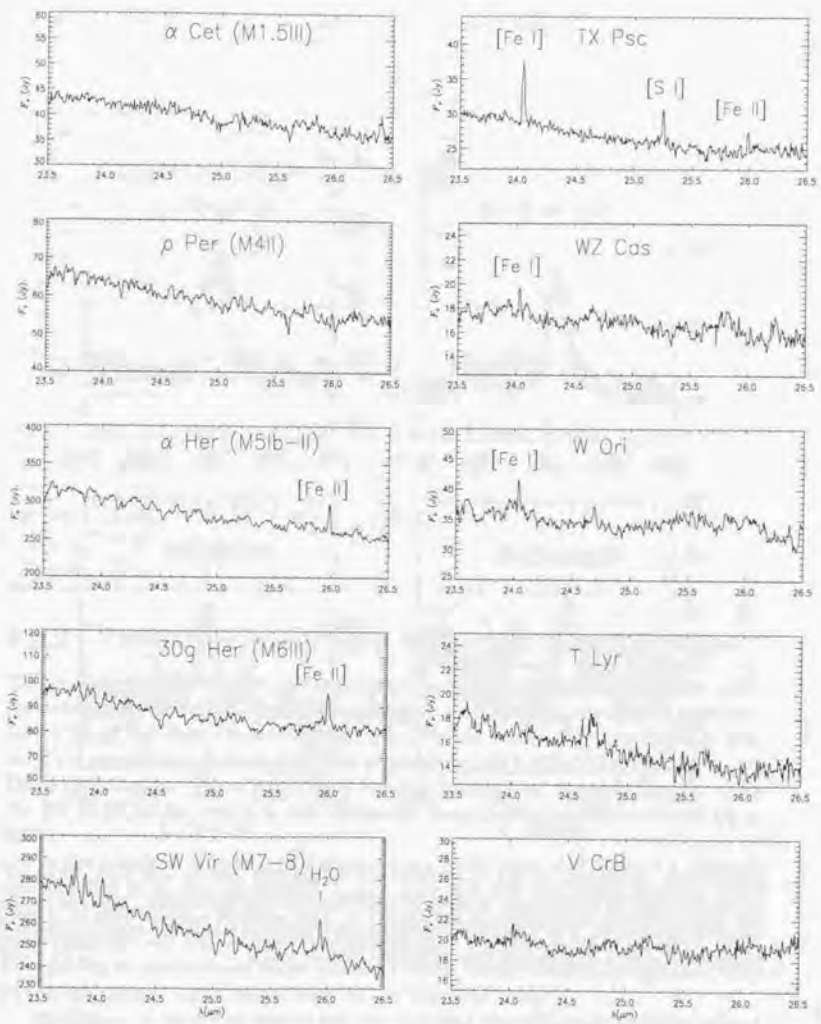

Figure 6.1: The 25 μm region of the observed spectra of M giants (left) and carbon stars (right)

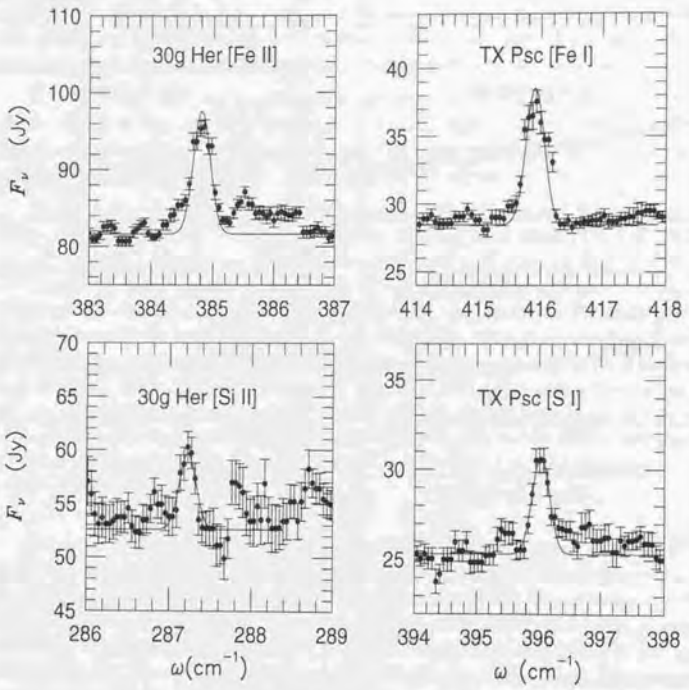

Figure 6.2: Examples of the lines detected in 30g Her and in TX Psc. The dot is the median of the signals in each grid defined by the resolution, and the error bar indicates $\pm 1\sigma$. The solid line indicates the best least-square fit assuming a flat continuum and a superposed Gaussian line profile

Table 6.1: The emission lines expected in the infrared range

λ (μm)	species	transition	E_u (cm^{-1})	A_{ju} (10^{-3}s^{-1})
24.042	[FeI]	$^5D_4$-$^5D_3$	415.93	2.50
34.713	[FeI]	$^5D_3$-$^5D_2$	704.00	1.60
25.988	[FeII]	$^6D_{9/2}$-$^6D_{7/2}$	384.77	2.13
35.349	[FeII]	$^6D_{7/2}$-$^6D_{5/2}$	667.64	1.57
17.938	[FeII]	$^4F_{9/2}$-$^4F_{7/2}$	2430.08	5.84
25.249	[SI]	$^3P_2$-$^3P_1$	396.8	2.13
34.814	[SiII]	$^2P_{1/2}$-$^2P_{3/2}$	287	0.217

Table 6.2: The emission lines detected in the observed spectra

λ (μm)	species	line flux (10^{-16}Wm^{-2})				
		30g Her	α Her	TX Psc	WZ Cas	W Ori
24.042	[FeI]	-	-	11.2	3.07	6.28
25.249	[SI]	-	-	5.70	-	-
25.988	[FeII]	16.3	39.1	3.22	-	-
34.814	[SiII]	5.41	-	-	-	-
35.349	[FeII]	5.41	-	-	-	-

6.2.2 Temperature and mass of the line emitting region

The temperature of the line emitting region can roughly be estimated by the upper excitation potential (E_u) of the line. As given in Table 6.1, the upper excitation potentials of the lines detected are between 287 and 667 cm^{-1}. Therefore the temperature is evaluated to be higher than several hundred Kelvin. On the other hand, the [Fe II] 17.9 μm (E_u = 2430 cm^{-1}) was not detected in any spectrum in which the [Fe II] 26 μm line was detected. Hence the temperature would not be so high as 3000K.

In the spectrum of 30g Her, we detected two [Fe II] lines as in Table 6.2. Though the line flux of the [Fe II] 35 μm is rather uncertain, the temperature about 1000-2000K is derived from the flux ratio of these two [Fe II] lines in 30g Her. For the other stars we can not estimate the temperature by flux ratios of emission lines, because the 35 μm region of α Her was not observed, and the spectra of carbon stars in the wavelength region longer than 27 μm are quite noisy.

Summarizing the above discussion, the temperatures of the line emitting regions are estimated from several hundred to 2000 Kelvin.

We estimate the mass of the line emitting region for 30g Her and TX Pcs in

which the fine-structure lines were clearly detected.

If the line is optically thin, the line flux ($F_{\rm ul}$) is

$$F_{\rm ul} = \frac{N_{\rm u} A_{\rm ul} E_{\rm ul}}{4\pi D^2},$$

where $N_{\rm u}$ is the total number of atoms in the upper level, D is the distance to the star, and the other quantities are expressed in standard notation.

We adopt 110 pc and 230 pc as the distances of 30g Her and TX Psc based on the trigonometric parallaxes in Hipparcos catalogue (ESA 1997). $N_{\rm u}$ is derived from the line flux measured for 30g Her and TX Psc (Table 6.2). The derived $N_{\rm u}$ is given in Table 6.3. The number of nuclei of the element ($N_{\rm elem}$) is estimated from $N_{\rm u}$ on the assumptions that the level populations are in thermal equilibrium, and all the atoms are in the ionization state of the detected line. The assumption of thermal equilibrium can be applied to the gas with higher density than critical density (e.g. $n_{\rm cr}^{\rm H} \sim 10^5$-$10^6$ cm^{-3} when collision with H I atoms is considered; see Hollenbach & Mckee 1989). The density of the warm region of the envelope would be higher than this criterion as we will discuss in the next section. The level population derived is shown in Figure 6.3 for Fe I ground state (a^5D) as a function of temperature as an example. We find that the population on the J=3 level is almost constant ($\sim$0.25) for the temperature higher than about 500K, from which the population rapidly decreases with decreasing of the temperature. Therefore the $N_{\rm elem}$ can be estimated from $N_{\rm u}$ if we adopt the population at around 1000K. Then the number of hydrogen atoms ($N_{\rm H}$) corresponding to $N_{\rm elem}$ is derived assuming the solar abundance. The $N_{\rm elem}$ and $N_{\rm H}$ are also given in Table 6.3. The $N_{\rm H}$'s derived from two or three lines agree well and correspond to about $2\times10^{-6}M_\odot$ and $6\times10^{-6}M_\odot$ in 30g Her and in TX Psc, respectively. These values are probably the lower limits of the masses of the line forming regions, because we assumed that the lines are optically thin and neglected the depletion of these metals by grains and/or molecules in the above discussion.

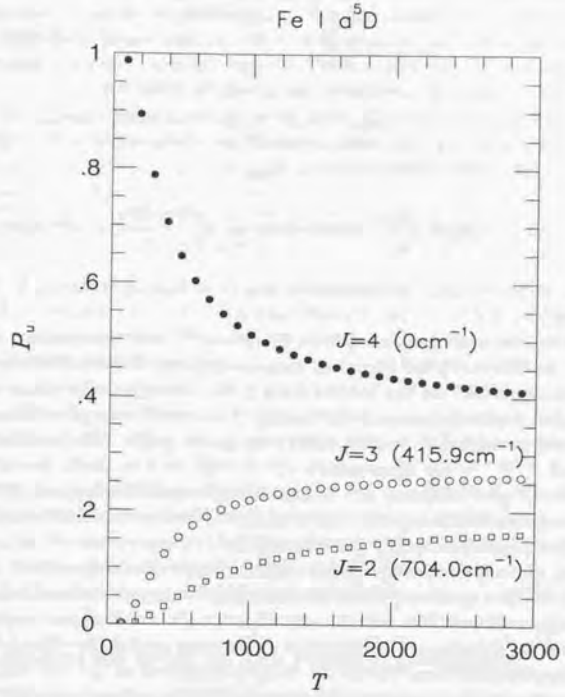

Figure 6.3: The level populations in the a^5D state of Fe I on the assumption of thermal equilibrium. Each level population is normalized as the total for J=0-4 to be unity. We can find that the population in J=3 level is about 0.2-0.25 for T >600K, and rapidly decreases with the decrease of temperature from 600K

6.3 Discussion

6.3.1 Location of the line forming region

In this subsection, we discuss where these emission lines arise based on the temperature and the mass in the line emitting region derived in the previous section.

As well known, mass-losing giants have expanding envelopes which are usually observed by the molecular emission (e.g. CO) in radio region, and mass loss rate and expansion velocity are determined. We give the mass loss rate and expansion velocity of the envelope of the stars in our sample in Table 6.4.

Here we assume the spherically symmetric and expanding envelope with a constant mass loss rate ($\dot{M}$). On these assumptions, the number of hydrogen atoms ($N_{\rm H}$) from $r = R_*$ (stellar surface) to $r = R_{\rm max}$ is

$$N_{\rm H} = \int_{R_*}^{R_{\rm max}} n_{\rm H} 4\pi r^2 dr = \frac{1}{m_{\rm H}} \int_{R_*}^{R_{\rm max}} \frac{\dot{M}}{v_e} dr,$$

where $n_{\rm H} = \dot{M}/(4\pi r^2 v_e m_{\rm H})$ is the number density of hydrogen, and v_e is the expansion velocity.

If the constant mass loss rate ($\dot{M} = 10^{-7} M_\odot {\rm yr}^{-1}$) and the constant expansion velocity ($v_e = 10\,{\rm km\,s^{-1}}$) are assumed, $R_{\rm max}$ must be as large as 10^{15}cm ($\sim 70 R_*$) for 30g Her and 2×10^{15}cm ($\sim 150 R_*$) for TX Psc to explain the mass of the line forming region derived above. If we assume $T = 1000$K at $r = 10^{14}$cm (several $\times R_*$) from the central star, around where dust grains might form, and temperature declines with $r^{-0.5\sim-1}$, the temperature at $r = 70R_*$ or $r = 150R_*$ would be about $100 \sim 300$K or lower. This may not be high enough to excite the spices to the upper levels of the lines detected in our observations. The line fluxes observed in these stars would not be explained by this picture.

However, the outer atmosphere of real red giants would be denser than that expected by the extrapolation of the circumstellar envelope with constant expansion velocity, because the outflow velocity should be smaller in the inner region than in the circumstellar envelope. Unfortunately, we cannot derive the velocity structure from the fine-structure lines due to the limited resolution of the SWS06. However, the temperature of the line emitting region which is at least as high as several hundred Kelvin suggests that these emission lines arise from the layer close to the photosphere. If we assume that the emission lines detected by our observations form within several $\times R_*$ ($\sim 10^{14}$cm) from the central star, the density of the line forming region must be as high as $10^9{\rm cm}^{-3}$ to explain the mass of the region derived above. This is corresponding to the expansion velocity of about 1 ${\rm kms}^{-1}$ if constant mass loss rate is assumed.

We suggest that the emission lines detected in our observation arise in the dense and warm region close to the star with small expansion velocity. A dense and quasi-static molecular forming zone in the outer atmosphere has been found from the excess absorption of low excitation lines of the CO first overtone bands in M giants and carbon stars including 30g Her (Tsuji 1988) and TX Psc (Ohnaka 1997). According to their analyses, the molecule forming zone is characterized by the temperature of about 1000K, the high column density ($N_{\rm c}({\rm CO}) \sim 10^{20}{\rm cm}^{-2}$), and the proximity to the star. Further, the existence of a rather warm molecule forming region around red giants is revealed by the ISO observations of the absorption features of H_2O and CO_2 (Tsuji et al. 1997) and of the CO_2 emission (Justtanont et al. 1998).

The high resolution UV observation of TX Psc using *HST* by Carpenter et al. (1997) revealed that the fluorescent lines of Fe I (2807 and 2823 Å) show no sign of outflow within the measurement uncertainty of 1-1.5 ${\rm kms}^{-1}$. Though they suggested that these lines originate in the chromosphere itself, this quasi-static neutral iron gas may relate to that found by our infrared observation.

Table 6.3: Estimation of mass in line forming region

	$N_{\rm u}$ (10^{46})	$N_{\rm elem}$ (10^{46})	$N_{\rm H}$ (10^{51})	M ($10^{-6} M_\odot$)
30g Her				
[Fe II] 26μm	1.5	6.6	2.1	1.7
[Fe II] 35.3μm	0.89	8.0	2.5	2.1
[Si II] 34.8μm	6.3	12	3.4	2.8
TX Psc				
[Fe II] 26μm	1.3	5.7	6.7[1]	5.6[1]
[Fe I] 24μm	3.4	15		
[S I] 25μm	3.3	13.2	8.4	7.0

[1] The sum of the $N_{\rm H}$'s (the masses) derived from the [Fe II] 26 μm and the [Fe I] 24 μm.

6.3.2 Ionization state in the outer atmosphere

Since the fine-structure lines detected in two M giants and three carbon stars are probably originating in the warm region close to the star, these lines can be good probes to investigate the structure and the chemistry in the outer atmospheres of cool evolved stars. In this subsection, we discuss the ionization of metals in the outer atmospheres based on the fine-structure lines detected.

The contrast of the emission lines detected in the carbon stars and in the M giants is remarkable; the emission lines of neutral metals (Fe I and/or S I) were detected in the carbon stars (TX Psc, W Ori and WZ Cas) while emission lines of ionized metals (Fe II and/or Si II) were detected in the M giants (30g Her and α Her). Though our sample is not large, this result suggests that the ionization states in the outer atmosphere are quite different between carbon stars and oxygen-rich

stars.

The comparison with UV observation is very useful in this discussion. The neutral metals (Mn and Fe) in the circumstellar envelopes of TX Psc and 30g Her were observed as the overlying absorption on the Mg II h and k emission lines around 2800Å (e.g., Eriksson et al. 1986, Luttermoser et al. 1994). The column densities of Mn I and Fe I estimated are larger in TX Psc than in 30g Her, though the values are quite uncertain due to the saturation of the overlying absorption. Further, the recent UV observation of Fe II emission lines by Carpenter et al. (1997) showed that the ionization fraction of iron (Fe II/Fe I) is significantly lower in the outer atmosphere of TX Psc than in that of M giants. Our result that the lines of neutral metals were detected in TX Psc but not in 30g Her is consistent with the results of these UV observations.

The ionization for collision dominated gas can be calculated using Saha's equation. For iron and silicon, whose ionization potentials are 7.86 and 8.15 eV, respectively, ions dominate if the temperature is higher than 2000K. However, the temperature of the whole outer atmospheres of 30g Her and α Her is unlikely as high as 2000K, and some other processes would be required to explain the ionization of iron and/or silicon in 30g Her and α Her.

In the outer part of the envelope, the interstellar UV radiation ionizes metals. However, the line emitting region would not be the outer part of the circumstellar envelope, which should not be as high as several hundred Kelvin. On the other hand, ionization of metals by chromospheric UV radiation is expected in the inner part of the circumstellar envelope and the outer atmosphere. Unfortunately, the far UV radiation of the stars in our sample is not available. However, our infrared observations imply that the activity of the chromosphere where the UV photons with high energy (e.g. $\lambda < 1575$ Å corresponding to the ionization potential of iron) are emitted is not so strong in the carbon stars as in the M giants, or there is some attenuation of the UV radiation in the carbon stars.

The reason for the difference of ionization states between carbon stars and oxygen-rich stars is not clear. We discuss here possible reasons by considering the differences between M giants and carbon stars which may be summarized as follows.
(i) The chemical composition, especially the C/O ratio.
(ii) The temperature structure of photospheres. This is due to the difference of molecular opacities influenced by the chemical composition.
(iii) The effective temperatures. Carbon stars may have rather lower effective temperatures than M giants. For instance, the effective temperatures of α Her and 30g Her are about 3200K or higher, while the effective temperatures of TX Psc, WZ Cas and W Ori are 3000-3100K.

The difference of the chromospheric activity itself between carbon stars and oxygen-rich stars is unknown. Since the Mg II h and k emission lines at 2800Å seems quite weak in low resolution UV spectra of carbon stars, the activities of the

chromosphere were considered to be much weaker than those in M giants. However, by the high resolution UV spectroscopy of TX Psc, it was clarified that the Mg II emission profiles in carbon stars are strongly affected by the overlying absorption of Mg II, Mn I and Fe II in the cool circumstellar envelope (Eriksson et al. 1986). Therefore the chromospheric activity, which is probably represented by the Mg II emission, may be as strong in carbon stars as in late M giants. Since the origin of chromosphere is unclear as described in Chapter 1, the effect of the difference of the chemical composition and the temperature on the chromospheric activity cannot be evaluated.

On the other hand, the attenuation of the UV flux from the chromosphere may be quite different between M giants and carbon stars, because possible opacity sources of UV radiation strongly depend on the chemical composition and the temperature. In fact, the flux decreases faster toward shorter wavelength in carbon stars, especially in N-type stars, than in M giants, and this has led to the idea that the flux is depressed by unknown opacity sources (so-called 'problem of violet opacity'). Johnson et al. (1988) examined several opacity sources including neutral metals and molecules, and suggested that the large opacity in N-type stars is due to the cooler outer photospheres of carbon stars than those of M giants. To clarify the reason of the weak UV and violet radiation should be quite important for understanding of the chemistry in the outer atmosphere.

6.3.3 Chemistry in the outer atmosphere

The ionization states of atoms in outer atmospheres, which may represent the strength of the chromospheric radiation, give constraints in modeling of the chemical processes in the outer atmspheres and the circumstellar envelopes, because the chromospheric radiation affects the molecule and dust formations and then the structure of the envelope (e.g. Beck et al. 1992). Our result suggests that the effect of chromospheric radiation is significant on the chemical processes in M giants, while that is not so large on those in carbon stars.

In addition to the fine-structure lines of metals, we detected many molecular features which would originate in the outer atmospheres in the infrared spectra of our stars. The molecular features of carbon stars were discussed in the previous chapter, and those of M giants were reported by Tsuji et al. (1997). Further, there are some evidences of molecular absorption in the outer atmospheres of our program stars found by the high resolution infrared spectroscopy (e.g. Tsuji 1988). We here summarize these results and discuss the chemistry in the outer atmospheres for three stars; 30g Her, SW Vir and TX Psc.

30g Her (M6III)

The results of our observation with the ISO SWS are as follows;
(i) [Fe II] and [Si II] were detected, while no line of neutral metals was detected.
(ii) The strong absorption of H_2O, which cannot be explained by the photospheric

component alone, was found in the 3 μm region (Tsuji et al. 1997). CO_2 emission was also detected in the 15 μm region.
(iii) The silicate emission at 9.7 μm is quite weak. The 13 μm emission feature which may be attributed to Al_2O_3 (Onaka et al. 1989) was detected.

Further, excess absorption of CO lines of the first overtone bands was reported by Tsuji (1988).

The chemistry in the outer atmospheres of M giants was theoretically investigated by Beck et al. (1992) including chromospheric radiation. Their model was calculated on the assumption of constant mass loss rate ($\dot{M} = 2 \times 10^{-6} M_\odot \mathrm{yr}^{-1}$) and constant expanding velocity ($v_{\exp} = 1.0\,\mathrm{kms}^{-1}$), and showed the effect of chromospheric UV radiation to the molecular concentration and to the dust formation. The UV radiation was given by scaling that of α Ori (i.e. $F_* = \beta F_{\alpha-\mathrm{Ori}}$ where β is the scaling factor). In their Fig. 8 which gives the molecular concentration as a function of β at $r = 5R_*$, we find that Fe^+ and Si^+ are abundant but Fe^0 is not in the model with rather strong UV radiation, e.g. the model with β larger than 1/30. However, in these models with strong UV radiation, the abundance of H_2O should be very small. We note that the effect of UV radiation on CO and CO_2 cannot be discussed here, because CO is quite abundant even in models with strong UV radiation ($\beta \sim 1$), and CO_2 was not considered in their calculation. The difficulty is how we explain the existence of H_2O and Fe^+ without Fe^0. This may indicate an inhomogeneous chromosphere suggested by Luttermoser et al. (1994) for this star. The inhomogeneity in the K I 769.9nm scattering was also reported by Plez & Lambert (1994).

SW Vir (M7-8)

The results of our observation with the ISO SWS are as follows;
(i) No fine-structure line was identified.
(ii) The excess absorption of H_2O at 3 μm and of CO_2 at 4.2μm was detected (Tsuji et al. 1997). H_2O absorption at 6 μm is weak and may be affected by the emission in the outer atmosphere. Many H_2O emission lines were detected in the wavelength region longer than 20 μm (Tsuji et al. 1999). CO_2 emission in the 15 μm region is stronger than that in 30g Her.
(iii) The silicate emission features at 9.7 μm and 18 μm are strong. The 13 μm emission was also detected (Tsuji et al. 1999).

Further, excess absorption in vibration-rotation lines of the CO first overtone bands and of the SiO first overtone bands was reported by Tsuji (1988) and Tsuji et al. (1994), respectively. Since the spectrum of SW Vir between 25 and 35 μm may be covered by the strong H_2O emission as mentioned in Section 6.2, the identification of fine-structure lines is quite difficult and we cannot conclude whether gaseous metals exist in the outer atmosphere or most metals have already condensed. However, the outer atmosphere of this star is obviously molecule-rich, and the chemistry of the outer atmosphere of this star may be explained by the model with weak chromospheric radiation in Beck et al. (1992).

Table 6.4: Fundamental propaties of our sample

	sp. type	$\dot{M}$ [1] ($10^{-7} M_\odot$)	$v_{\exp}$ [1] (km/s)	R [3] ($R_\odot$)	P [4] (day)	T_{eff} [5] (K)
o Cet	M1.5III	-	-	-	-	3900
ρ Per	M4III	0.1[2]	7.0[2]	160	50	3500
α Her	M5Ib-II	0.8[2]	8.0[2]	430	-	3200
30g Her	M6III	1.1	8.0	180	70	3200
SW Vir	M7-8	4.0	7.0	260	150	3000
TX Psc	N, C7,2	0.9	10.5	210	-	3080
W Ori	N, C5,4	0.74	11.1	220	212	2980
WZ Cas	SC, C9,2JLi	0.26	5.1	-	186	2980
T Lyr	J, C6,5	0.71	12.4	-	-	2400
V CrB	CH?, C6,2e	2.4	7.1	-	357	2200:

[1] The mass loss rate and the expansion velocity derived based on CO emission by Kahane and Jura (1994) for M giants and by Olofsson et al. (1993) for carbon stars
[2] The mass loss rate and the expansion velocity derived based on optical resonance lines by Sanner (1976)
[3] The stellar radius determined by the distance (Hipparcos catalogue) and anglar diamiter (Dyck et al. 1996, Richichi et al. 1995)
[4] The pulsation period
[5] The effective temperature determined by the IRFM (see Chapter 5 for carbon stars and Tsuji (1986) for M giants)

TX Psc (N-type)

The results of our observation with the ISO SWS are as follows;
(i) The fine-structure lines of Fe^0 and S^0 are strong, while that of Fe^+ is weak.
(ii) CO and CS emission in 4-8 μm region was suggested. HCN emission features at 14 μm were detected.
(iii) The emission feature of SiC dust expected at 11 μm was not detected.

No theoretical model of chemistry in the outer atmospheres including chromospheric radiation is known for carbon-rich stars. However, there is no evidence of the strong effect of the UV radiation in this star.

6.3.4 Relation with stellar evolution

Finally, we discuss the relation of spectral features with the evolution of red giants.

We observed oxygen-rich giants whose spectral types are from M1.5 through M7-8. We assume here that the sequence of spectral type roughly represents the evolution of red giants. In Table 6.3 where the basic stellar parameters are given, we can find that the radius and the period of pulsation continuously increase with the spectral types becoming later, except for α Her. This indicates that our assumption is reasonable, though the masses of these stars are unknown. We note that α Her

is excluded from our consideration, because this star shows some characteristics as a supergiant; e.g. the luminosity class is Ib-II and the radius is very large ($R \sim 400 R_\odot$).

Our results are that no fine-structure line was detected until the M4 star (ρ Per), emission lines of ions were detected in the M6 star (30g Her), and no strong line is seen in the M7-8 star (SW Vir). This may indicate the following picture of evolution.

(i) The outer atmospheres have not grown in the stars earlier than M5.

Since strong ultraviolet emission lines (e.g. Mg II λ2800) were observed (Judge et al. 1993), the chromosphere of ρ Per is active and the metals in the outer atmosphere would be highly ionized (e.g. Guilain & Mauron 1996). However, the mass loss rate of ρ Per is still low ($\sim 10^{-8} M_\odot$), so that the infrared fine-structure lines are too weak to be detected in our observation.

(ii) The outer atmosphere become dense enough to show the fine-structure lines and molecular features in stars with the spectral type about M6. The Chromosphere is still active.

Since the mass loss rate of 30g Her is probably much higher than that of ρ Per (see Table 6.3) and the chromosphere is still active (Luttermoser et al. 1994), Fe^+ and Si^+ are abundant in the outer atmosphere enough to be detected in our observation (Beck et al. 1992). On the other hand, many molecular features which would originate in the outer atmosphere are also found for this star as described above. Therefore the transition of the outer atmosphere from ion-rich to molecule-rich occurs at M6 star. This was also suggested by the observation of radio continuum which showed that ion fraction rapidly decreases at M6 stars (Drake et al. 1991).

(iii) The chromosphere becomes weak and fine-structure lines of ions disappear in the stars later than M6. Molecules and dust become abundant.

We cannot conclude whether most metals are ionized or in neutral or in solid state in SW Vir as discussed above. However, the outer atmosphere of this star is obviously molecule- and dust-rich. As a result, the stellar outflow significantly grows and stars show heavier mass loss from this phase.

On the other hand, it is difficult to discuss the relation between the infrared spectra and evolution for carbon stars, because the evolutionary sequence is unclear in carbon stars. We only comment on the non-detection of fine-structure lines in T Lyr and in V CrB. One possible reason for this result is that these stars may be metal-poor; the oxygen abundance of T Lyr was derived by Lambert et al. (1986) as [O/H]$= -0.5$ which is corresponding to [Fe/H]~ -0.8 in the usual chemical enrichment of the Galactic disk (Edvardsson et al. 1993). V CrB has large radial velocity (about 120 kms^{-1} by Barnbaum 1992) which may indicate halo population. Another possibility is that the effective temperatures of these stars would be much lower than those of the other stars in which fine-structure lines were detected. However, the effect of the lower temperature on the fine structure lines is unclear.

6.4 Concluding remarks

We carried out observations of the infrared fine-structure line emission using the ISO SWS, and detected them for the first time for five red giants including M giants and carbon stars. We showed that these lines are good probes to investigate the outer atmospheres of cool giants, where various molecules and dust grains probably form. In the chemical processes in this region, chromospheric radiation should play an important role in some stars. The difference of ionization states between carbon stars and oxygen-rich giants is quite remarkable, and this result gives an important constraint for modeling of the chemistry in the outer atmospheres of mass losing giants. Further, we suggest that the fine-structure lines of ions appear in a stage of stellar evolution of oxygen-rich stars when the outer atmosphere grows but the chromosphere is still active. This may be corresponding to M6 giants, and after which the mass loss rate may rapidly increase.

In addition to the detailed modeling of the structure and the chemical processes in the outer atmospheres, further observations of fine-structure lines would be quite useful. The high resolution spectroscopy ($R > 10^4$) of these lines is desired to investigate the velocity field of the outer atmospheres where stellar outflows would be accelerated. The time variation of the emission should also be considered. In fact, the time dependence of the flux of the [O I] (63 μm) line in α Ori was suggested by Haas et al. (1995). Periodic monitoring of the fine-structure lines will give important information for the study of the complicated structures of the outer atmospheres.

References

Barnbaum C., 1992, AJ 104, 1585
Beck H. K. B., Gail H. -P., Henkel R., Sedlmayr E., 1992, A&A 265, 626
Carpenter K. G., Robinson R. D., Johnson H. R. et al., 1997, ApJ 486, 457
Drake S. A., Linsky J. L., Judge P. M., Elitzur M., 1991, AJ 101, 230
Dyck H. M., van Belle G. T., Benson J. A., 1996, AJ 112, 294
Edvardsson B., Andersen J., Gustafsson B. et al., 1993, A&A 275, 101
Eriksson K., Gustafsson B., Johnson H. R. et al., 1986, A&A 161, 305
ESA, 1997, The Hipparcos and Tycho Catalogues, ESA SP-1200
Guilain Ch., Mauron N., 1996, A&A 314, 585
Haas M. R., Glassgold A. E., 1993, ApJ 410, L111
Haas M. R., Glassgold A. E., Tielens A. G. G. M., 1995, ASP Conf. Ser. 73, *Airborne Astronomy Symposium on the Galactic Ecosystem*, eds M.R. Haas, J. A. Davidson, E. F. Erickson, 397
Hollenbach D., Mckee C. F., 1989, ApJ 342, 306
Johnson H. R., Luttermoser D. G., Faulkner D. R., 1988, ApJ 332, 421
Judge P. G., Luttermoser D. G., Neff D. H., Cuntz M., Stencel R. E., 1993, AJ 105, 1973
Justtanont K., Feuchtgruber H., de Jong T. et al., 1998, A&A 330, L17
Kahane C., Jura M., 1994 A&A 290, 183
Luttermoser D. G., Johnson H. R., Eaton J. A., 1994, ApJ 422, 351
Ohnaka K., 1997, Ph. D. Thesis, The University of Tokyo
Olofsson H., Eriksson K., Gustafsson B., Carlström U., 1993, ApJS 87, 267
Onaka T., de Jong T., Willems F. J., 1989, A&A 218, 169
Plez B., Lambert D. L., 1994, ApJ 425, L101
Richichi A., Chandrasekhar T., Lisi F., et al. 1995, A&A 301, 439
Rodgers B., Glassgold A. E., 1991, ApJ 382, 606
Sanner F., 1976, ApJS, 32, 115
Tsuji T., 1986, A&A 156, 8
Tsuji T., 1988, A&A 197, 185
Tsuji T., Aoki W., Ohnaka K., 1999, in proceedings of *The Universe as seen by ISO*, in press
Tsuji T., Ohnaka K., Hinkle K. H., Ridgway S. T., 1994, A&A 289, 469
Tsuji T., Ohnaka K., Aoki W., Yamamura I., 1997, A&A 320, L1

Chapter 7

Summary and concluding remarks

We carried out the observations of cool evolved stars with the ISO SWS and detected various atomic and molecular features in the infrared spectra. Our results showed the importance of the entire infrared spectra of these objects free from contaminations of the Earth's atmosphere with reasonably high resolution. By the good quality spectra, especially the higher resolution ones with the SWS06, various molecular bands and fine-structure lines of metals were definitively identified for the first time in these red giants.

We analyzed molecular spectra of N-type and SC-type carbon stars. By the present work, most of the absorption features in the wavelength range from 3 to 15 μm were identified for our sample. We showed the dependence of the molecular features on the C/O ratio which should be close to unity in SC-type stars. The CH bands are much weaker in SC-type stars than in N-type stars. The SiS bands were detected in the SC-type star WZ Cas, while no feature of SiS is seen in N-type stars. These results can be explained well by the difference of C/O ratios between N-type stars and SC-type stars. On the other hand, The absorption features of HCN in the spectra of the SC-type stars in our sample are stronger than those in N-type stars. This fact is basically explained by the cooler photosphere of the SC-type stars due to the lower C/O ratio. Thus the C/O ratio not only directly affects the abundance of molecules formed in the photosphere but also indirectly affects it through the influence on the temperature structure of the photosphere.

The observed spectra of TX Psc and WZ Cas in the 3-8 μm region are, at least qualitatively, reproduced by our synthetic spectra for the reasonable stellar parameters. However, the absorption features of CO and CS in the observed spectra are quite weaker than predicted ones. In addition, some distinct emission bands of HCN were detected at 14 μm in the spectrum of TX Psc. Though there are uncertainties in model photospheres and stellar parameters, we conclude that some molecular emission in outer atmospheres contributes to the infrared spectra.

In addition to rich molecular features, the fine-structure line emission of iron, silicon and sulfur was also detected in the spectra of the oxygen-rich and carbon-rich AGB stars in our sample. Based on the line fluxes measured and the excitation potential of the lines, we conclude that these emission features originate in the rather warm and dense region close to the star, and these lines could be good probes to investigate the outer atmospheres of cool giants, where many molecules and dust grains probably form. One unexpected but remarkable result is that the emission lines of ions were detected in oxygen-rich stars while the emission lines of neutral metals were found in carbon stars. This means that ionization states in the outer atmospheres between carbon stars and oxygen-rich giants are quite different. This result would give an important constraint on the modeling of the chemistry including chromospheric radiation in the outer atmospheres of mass losing giants. Further, based on a systematic survey of the line emission for M giants, we suggest that the fine-structure lines of ions appear in a stage of stellar evolution when the outer atmosphere grows but the chromosphere is still active. This is corresponding to M5-6 giants, and after which the mass loss rate would rapidly increase.

Our study of the SWS spectra suggests the existence of the outer atmospheres with quite complicated structures even in the semi-regular and irregular variables. While stellar pulsation should play an important role in Mira variables, some other mechanisms would be required for the formation of the outer atmospheres and the mass loss outflow in the stars studied in the present work. The chromosphere would influence the chemical processes and then the structures of the outer atmospheres, especially in oxygen-rich stars. Our results will put important constraints on modeling of the outer atmospheres dealing with hydrodynamics and photo-chemistry. The detection of various atomic and molecular features in our SWS spectra of red giants also suggests the direction of future observations – the high spatial resolution mapping and the high spectral resolution spectroscopy of the molecular bands and the fine-structure lines for the objects as discussed in this thesis. These observations will reveal more clear spatial and velocity structures of the outer atmospheres in cool evolved stars.

Acknowledgments

I wish to express my thanks to Prof. T. Tsuji for leading my researches with valuable advices and encouragements throughout the work. To him and to Dr. K. Ohnaka, I am very much indebted for their cooperation in the observation with the ISO. I am grateful to Prof. H. Okuda for taking initiative in our ISO project. I would like to thank Dr. I. Yamamura for helpful support in the data reduction, and also thank the SWS Instrument Dedicated Team for making the SWS Interactive Analysis software available. I also thank the members of our ISO group, especially Drs. K. Kawara, T. Tanabé and Y. Sato for helpful advice and support. Thanks are also due to Prof. Ando for useful comments.